Mechanistic, enzymatic and structural insights into *M. tuberculosis* Alkyl-hydroperoxide reductase subunit C, a key enzyme of the mycobacterial antioxidant defense system as well as its interaction with its reducing partner, Thioredoxin C

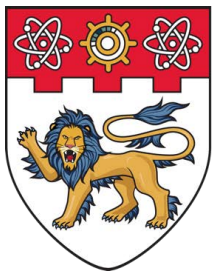

NANYANG TECHNOLOGICAL UNIVERSITY
SINGAPORE

WONG CHUI FANN

SCHOOL OF BIOLOGICAL SCIENCES

A thesis submitted to the Nanyang Technological University in partial fulfilment of the requirement for the degree of Master of Science

2017

ACKNOWLEDGEMENTS

I would like to express my utmost gratitude to my advisor, Professor Gerhard Grüber for his insightful comments, encouragements, patience and immerse knowledge. Your guidance and support throughout my master's program has led to the completion of my master's dissertation. A special thank you, also for supporting me financially throughout my master's education. Your confidence in me has helped me achieve things I never thought I could achieve. I could not have imagined having a better advisor and mentor for my research.

I am also indebted to Dr. Kamariah Neelagandan, Dr. Toh Yew Kwang and Ms. Sek Mun Foong for their guidance and discussions during my enzymatic kinetics assay experiments.

Also, I would like to thank Dr. Shin Joon for his guidance through NMR as well as data analysis. His expertise in this field has allowed progress for my dissertation, leading to the results I have obtained. Not to forget, Dr. Malathy Sony Subramanian Manimekalai has guided me in many ways with regards to HADDOCK modelling and crystallography. For without her expertise, I would not have been able to complete this dissertation nor published a paper.

I am also immensely grateful to Dr. Saw Wuan Geok, for being my constant throughout my initial stages of learning as well as through this master's program. I am grateful for all the discussions we have had, that has incented me to widen my research from various perspectives. Thank you, for all the emotional, physical and mental support you have provided me thus far. Without them, I would not imagine completing my master's program.

I would also like to express my sincere gratitude to Ms. Sherilyn Chong, for all the discussions we've had as well as for taking initiatives to help me out wherever necessary. Thank you for your jokes during my toughest days and, for your support through experiments. You have made my life in this lab much more pleasant.

I would also like to thank the other lab members who have helped me in one way or the other: Dr. Ardina Grüber, Dr. Hendrick Sielaff, Dr. Wilson Nartey, Dr. Priya Ragunathan, Mr. Arvind Kumar Khandelia, Mr. Singh Dhirendra, Mr. Bogdanovic Nebojsa, Ms. Pan Ankita and Ms. Bharti Singal.

I am thankful to Dr. Manikkoth Balakrishna Asha for her help in collecting X-ray data at the National Synchrotron Radiation Research Centre (NSRRC, Hsinchu,

Taiwan). Also, I would like to thank the staffs of beamline 13B1 at NSRRC for their technical assistance. In addition, I would like to acknowledge all the academic and technical staffs and facilities at the School of Biological Sciences, who have helped me in one way or the other with my research work.

Lastly, I would like to extend my gratitude to my parents, my older brother and my best friends, for their emotional support throughout my studies.

LIST OF FIGURES

Introduction

Materials and Methods

Results

Discussion

LIST OF TABLES

Materials and Methods

Results

Å	Angström
AhpC	Alkyl-hydroperoxidase reductase subunit C
AhpF	Alkyl-hydroperoxidase reductase subunit F
AIDS	Acquired Immune deficiency syndrome
C_P	Peroxidatic cysteine
C_R	Resolving cysteine
DTT	Dithiothreitol
E. coli	*Escherichia coli*
EDTA	Ethylenediaminetetraacetic acid
EM	Electron microscopy
FF	Fully folded
FQ	Fluoroquinolones
H. pylori	*Helicobacter pylori*
H_2O_2	Hydrogen peroxide
HIV	Human Immunodeficiency Virus
INH	Isoniazid
IPTG	Isopropyl-β-D-thiogalactoside
LTBI	Latent tuberculosis infection
LU	Locally unfolded
M. bovis	*Mycobacterium bovis*
M. tuberculosis	*Mycobacterium tuberculosis*
MDR-TB	Multi-drug resistant tuberculosis
NaCl	Sodium chloride
NADH	Nicotinamide adenine dinucleotide
NADPH	Nicotinamide adenine dinucleotide phosphate
Ni-NTA	Nickel-nitrilotriacetic acid
NMR	Nuclear magnetic resonance
NMR	Nuclear magnetic resonance
PCR	Polymerase chain reaction
PDB	Protein Data Bank
RMP	Rifampicin
S. typhimurium	*Salmonella typhimurium*
SEC	Size exclusion chromatography
TB	Tuberculosis

TNF	Tumor necrosis factor
Trx	Thioredoxin
TrxR	Thioredoxin reductase
WHO	World Health Organization

Abstract

Abstract

ABSTRACT

In 2015, the World Health Organization estimated that Tuberculosis (TB) infection affects a third of the world's population and is the leading cause of mortality caused by a single infectious agent. Through the years, effective drugs were designed to target its causative agent, *Mycobacterium tuberculosis* (*M. tuberculosis*). Despite this, the evolvement of resistant strains is still a cause of concern. To persist in the harsh conditions of a host's macrophage, *M. tuberculosis* has evolved various mutations, which includes the overexpression of an alkyl-hydroperoxide reductase subunit C (*Mt*AhpC) protein. However, few studies have been performed on the protein, *Mt*AhpC in relation to TB infection.

In the current study, recombinant *Mycobacterium bovis* (*M. bovis*) (BCG Strain) AhpC (*Mb*AhpC), which shares an identical protein sequence as *Mt*AhpC, was generated to elucidate the structure of *Mb*AhpC in solution. 2D projections were then performed, thereby confirming existing postulations on the dodecameric ring of AhpC in solution. With that, further characterization of *Mb*AhpC through kinetics assay provide insights into the enzymatic kinetics of *Mb*AhpC. For the first time, the accurate kinetic parameters of *Mb*AhpC, such as the catalytic efficiency (k_{cat}/ K_m) and Michaelis constant (K_m) were computed from the experimental data obtained. In addition, NMR titration assays revealed the reducing partner of AhpC as well as its interacting residues.

Point mutations were performed on the unique N-terminus of *Mb*AhpC. Downstream experiments like size exclusion chromatography and dynamic light scattering further highlighted the uniqueness of the conserved residues lying in the N-terminus in maintaining the redox-oligomerization. With molecular docking and structural studies, the importance of the N-terminus of *M. tuberculosis* was further elaborated from a structural point of view.

All in all, the results presented in the current studies revealed biochemical, biophysical and structural insights into *Mt*AhpC.

1. Introduction

Introduction

1 INTRODUCTION

Tuberculosis and its causative agent, *Mycobacterium tuberculosis* (*M. tuberculosis*) has infected many people and resulted in a high mortality rate since primeval times. Aerobic respiration by *M. tuberculosis* generates reactive oxygen and nitrogen radicals. In order to subsist in the harsh environment of the human body, the bacteria evolved a variety of measures to evade the human immune response and thrive in the host. One such measure developed by *M. tuberculosis* is its expression of peroxiredoxins, which aids in reducing the elevated levels of organic peroxides by decomposing them. As a result, *M. tuberculosis* is able to thrive in a host cell, and its persistence within its host eventually results in its host mortality.

1.1 Impact of tuberculosis in the world

Ranked above Acquired Immunodeficiency Syndrome (AIDS) in causing mortality because of an infectious disease [1], Tuberculosis (TB) has claimed the lives of many individuals ever since ancient times. In the recently published World Health Organization's (WHO) Global Tuberculosis Report 2016, an additional 10.4 million new cases with a mortality of approximately 1.8 million individuals were reported [2]. Most of the TB cases reported occurred in Asia and WHO-classified African regions with approximately 61% and 26%, respectively. 87% of these incidents were reported to occur from the 30 high TB burden countries with the majority of these cases being from South Africa, Pakistan, Nigeria, China, Indonesia and India. Statistically, approximately 11% were amongst those patients coinfected with HIV as well. A large proportion of TB coinfection with HIV were found in WHO-classified African Region (Figure 1.1) [2].

The WHO has derived various methods to estimate TB mortality which comprises of two main categories; (i) TB mortality among HIV-negative people and (ii) TB mortality among HIV-positive people [2]. Reports have shown that approximately 84% of TB mortality occur in the category of patients who are HIV-negative in WHO-classified African Region and South-East Asia countries [2]. On the other hand, India and Nigeria account for the majority of TB mortality among the HIV-positive category [2]. In particular, the 30 high TB burden countries vary significantly in terms of the number of TB cases, with some countries experiencing substantial reductions (Myanmar, Ethopia, China, Pakistan, the Philippines and the Russian Federation) to an increase in the number of TB cases in the Democratic People's Republic of Korea and in Congo

[2]. Despite the number of TB cases reducing slowly (from 1.4% to 1.5% in 2000-2015), the need to accelerate the decline in TB cases is necessary to facilitate in the reduction of TB mortality [2].

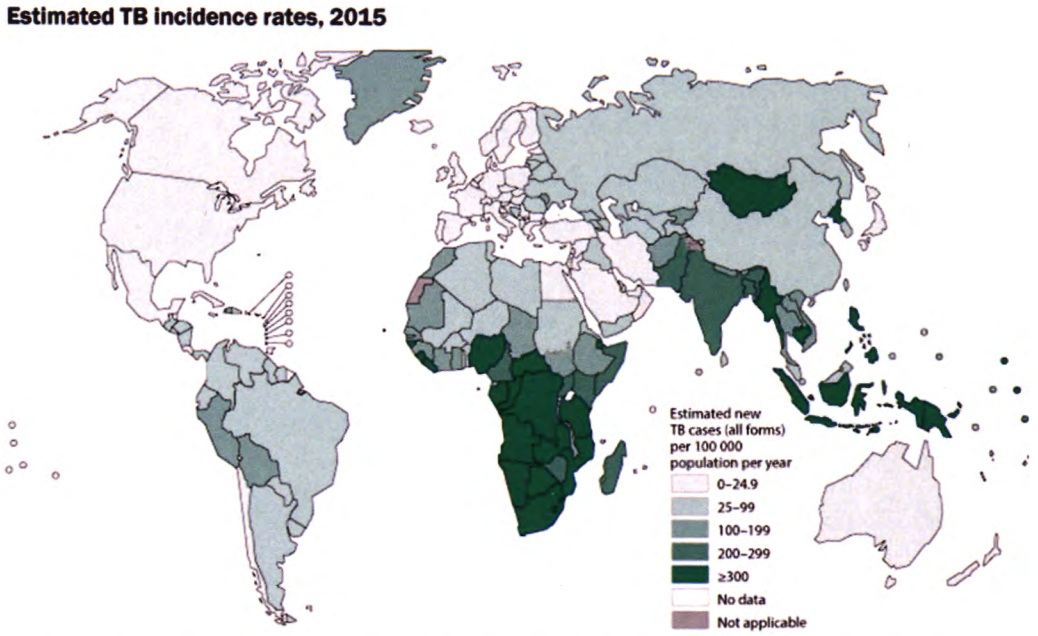

***Figure 1.1**: Visual representation of the estimated number of cases of TB in 2015.* Majority of TB cases are regionalized in Asia and WHO-classified African region, with more than 300 per 100,000 population. The 30 high TB burden countries are Angola, Bangladesh, Brazil, Cambodia, China, Congo, Central African Republic, DR Congo, DR Korea, Ethiopia, India, Indonesia, Kenya, Lesotho, Liberia, Mozambique, Myanmar, Namibia, Nigeria, Pakistan, Papua New Guinea, Philippines, Russian Federation, Sierra Leone, South Africa, Thailand, the United Republic of Tanzania, Viet Nam, Zambia and Zimbabwe. This figure was reused from World Health Organization Global Tuberculosis Report 2016 [2].

1.2 Tuberculosis infection in a host

TB infections can be clinically classified as latent (LTBI) or active TB infection [3]. The former encompasses an asymptomatic and a non-transmissible state of TB whilst the latter encompasses a transmissible TB disease presenting physical symptoms such as fever, persistent cough with haemoptysis, fatigue, loss of appetite and loss in body weight [4]. According to the Centers for Disease Control and Prevention (CDC), the evaluation of a patient suspected of carrying active TB will undergo various tests to confirm the presence of active TB [5]. Generally, the Mantoux tuberculin skin test (TST) is performed, followed by a posterior-anterior chest radiograph and subsequently, by a sputum smear as well as a radiometric liquid culture (BACTEC) [5]. However, there are also cases of patients, who are tested as culture-positive for active TB disease but are physically asymptomatic [3, 6]. Studies have suggested that these patients experience clinical symptoms at a much earlier phase prior to presenting physical symptoms. In

such cases, the host is said to experience a delayed disease presentation due to an earlier reactivation of the disease [7, 8]. Usually, these patients are classified as having subclinical TB or LTBI [3]. Nonetheless, these studies exemplifies that the presence of LTBI reactivation and ongoing TB infection are largely responsible for the global TB infections [9].

Exogenous factors such as the source (defined as a patient being diagnosed as carrying infectious TB [10, 11]) and proximity to the source govern the possibility and progression of TB infection. From the 20th century epidemiological surveys, the outcomes suggest the relationship between the proximity to an infectious TB patient and contracting TB [12, 13]. In addition, factors such as overcrowding in a region with the population infected with TB disease, also predisposes one to TB infection [14]. Other risk factors were also suggested, including excessive alcohol intake, smoking, prior type II diabetes mellitus, malnutrition [15] and indoor air pollution [14].

Patients who are HIV-positive, are also at risk of TB infections [3, 6, 16]. Statistics have shown that in sub-Saharan Africa, approximately 30% of patients who are coinfected with TB and HIV results in mortality in less than a year of TB diagnosis [17]. The increased in mortality was shown to result from the delay in the treatment from the onset of physical symptoms of TB infection to the eventual confirmation through a smear-positive TB detection [18]. Therefore, this highly suggests that HIV/TB mortality could be reduced should there be an early diagnosis and treatment. Furthermore, some HIV-positive patients had been found as smear-negative in the initial phase [19]. As a result of multifactorial reasons such as inadequate radiographic facilities or inadequate knowledge on TB disease, these HIV-positive patients with smear-negative results would have an increased delay in diagnosis and treatment of TB [20]. With the coinfection of HIV and TB, the patient would have a higher chance of LTBI reactivation and subsequently, leading to TB progression [3, 17, 21]. Current HIV treatment with highly active antiretroviral therapy (HAART) has shown that HAART significantly reduces a HIV-positive patient's risk of being infected with TB [6, 22, 23]. With such implementations, this could plausibly play a key role in reducing HIV/TB mortality.

Nonetheless, exposure to *M. tuberculosis* may result in either the complete elimination or persistence of the pathogen [3, 8]. The elimination of *M. tuberculosis* were largely observed in health care workers who were exposed to infectious TB patients [8], but tested negative for TST. Here, it was found that the body's innate

mechanisms such as recruitment of macrophages [24] and neutrophils [25] may be responsible for eliminating the pathogen. In opposition to the elimination of TB infection, persistence of the pathogen is defined as the ability of *M. tuberculosis* to adapt in harsh environments which allows it to transit between non-replicating phase and replicating phase [8]. The persistence of *M. tuberculosis* suggests that the patient may be either infected with LTBI or active TB [26]. Although no evidence has been found to confirm the presence of a transcriptional response regulator (*dos*R) being responsible for dormancy in LTBI human infections [27], *in vitro* studies have shown that *dos*R regulon is responsible for the persistence of *M. tuberculosis* [8, 28, 29].

1.3 Pathogenesis of *M. tuberculosis* in causing pulmonary TB

M. tuberculosis is not known to persist in any environmental reservoirs apart from humans [30, 31]. Little has been understood about the early phase of infection by *M. tuberculosis* in humans. Models of the early events that occur during primary infection of TB were proposed in guinea pigs, mice and rabbits [32]. However, studies have also proved that guinea pigs were highly susceptible to even a few viable tubercle bacilli [33]. Studies performed with mice provided more insights into vaccinations rather than the pathogenesis of TB [34, 35]. Lastly, rabbits were shown to be more resistant to *M. tuberculosis* as compared to guinea pigs and mice. Experiments performed on rabbits infected with *M. tuberculosis* showed that despite the development of pulmonary TB and cavities, none of the infections progressed to active TB [36, 37]. These studies have not provided the minute details about the pathogenesis of *M. tuberculosis*, but instead, have enlightened scientists with an overview of the pathogenesis of TB. Moving forward from animal models, scientists observed that the pathogenesis of *M. tuberculosis* was better understood through non-human primates (NHP), zebrafish embryo or modern imaging technologies. In fact, the radiological and clinical manifestations observed in TB infection in NHPs were found to be comparative to that of humans [38-40]. The study of zebrafish embryos infected with *M. marinum* provided a clarity towards the preliminary stages of TB infection [41-43]. The preliminary stages of TB infection are described briefly hereafter with reference to Figure 1.2 and 1.3.

The preliminary stages of TB start from the inhalation of the tubercle bacilli, *M. tuberculosis* which infects the human respiratory tract (Figure 1.2, part 1) and is subsequently translocated to the lower respiratory tract (Figure 1.2, part 2). The

translocation results in *M. tuberculosis* encounter with alveolar macrophages [3], whereby it internalizes the alveolar macrophages and actively blocks phagosome-lysosome fusion [44, 45] (Figure 1.2, part 3). Following the inhibition of the maturation of the phagosome [46, 47], *M. tuberculosis* was proposed to be involved in rupturing the phagosome [48] before translocation into the cytosol [49]. The ESX-1 secretory pathway and the secreted ESAT-6 was shown to facilitate this translocation [49] which subsequently leads to the release of bacterial products and/or even genomic DNA fragments in the cytosol [50-52]. It is uncertain as to whether *M. tuberculosis* possesses the advantages of releasing bacteria products in the cytosol [53, 54]. However, studies performed suggested that the translocation of *M. tuberculosis* to the cytosol of macrophages induces an innate immune response against *M. tuberculosis* [55]. This is performed through the ESX-1 secretory system whereby through this pathway, *M. tuberculosis* can elicit a type I interferon response in infected macrophages [56]. One study had shown that the elicitation of type I interferon response in mouse decreases the mouse immunity against *M. tuberculosis* infection [57, 58]. This highly suggest that type I interferon response promotes the growth of *M. tuberculosis* rather than eliminate the infection. Although this model has not been confirmed in humans, it has indeed provided a clearer understanding to the pathway of *M. tuberculosis* infection.

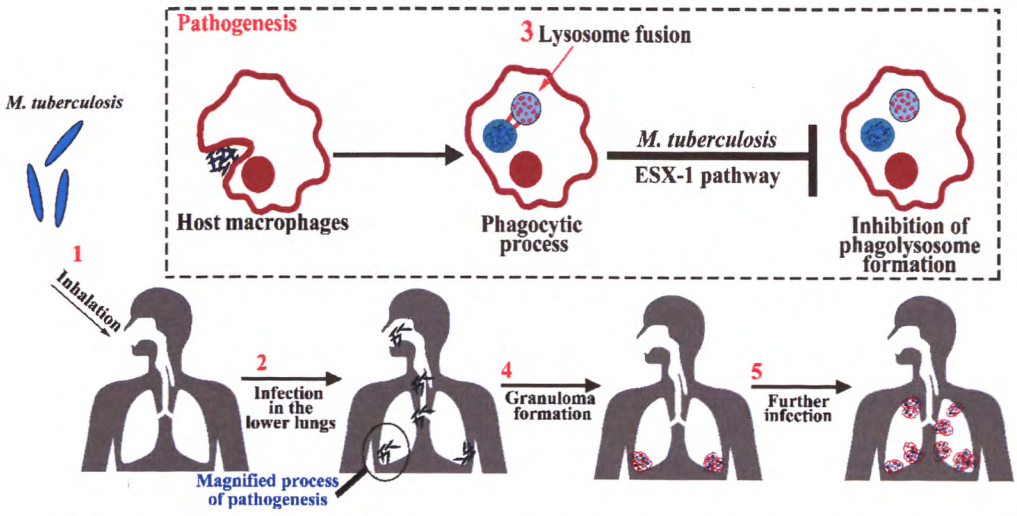

***Figure 1.2**: The initial stages of the infection process of M. tuberculosis.* 1. Inhalation of the bacteria causes an infection in the lower respiratory tract. 2. To combat the infection, the host immune system will induce the recruitment. 3. However, *M. tuberculosis* is able to prevent the maturation of the phagosome into a phagolysosome *(boxed region)*. 4. If the host is immune-compromised or exposed to infectious TB, the elimination of *M. tuberculosis* will be decreased. This leads to the formation of granulomas in the host. 5. Subsequent infections or LTBI reactivation may lead to TB progression to active TB, where it infects the rest of the lungs and plausibly, organs.

The infection then proceeded with the recruitment of cells at the site of infection and subsequently, the formation of a granuloma by the host [32] (Figure 1.2, part 4). Thereafter, T-cells are activated, and this leads to the onset of a cell-mediated immune response. To carry on the process of infection, infected dendritic cells or inflammatory monocytes would then transport *M. tuberculosis* to the lymph nodes of the host for T-cell priming. It was reported that *M. tuberculosis* is capable in delaying the initial T-cell priming and T-cell trafficking [59].

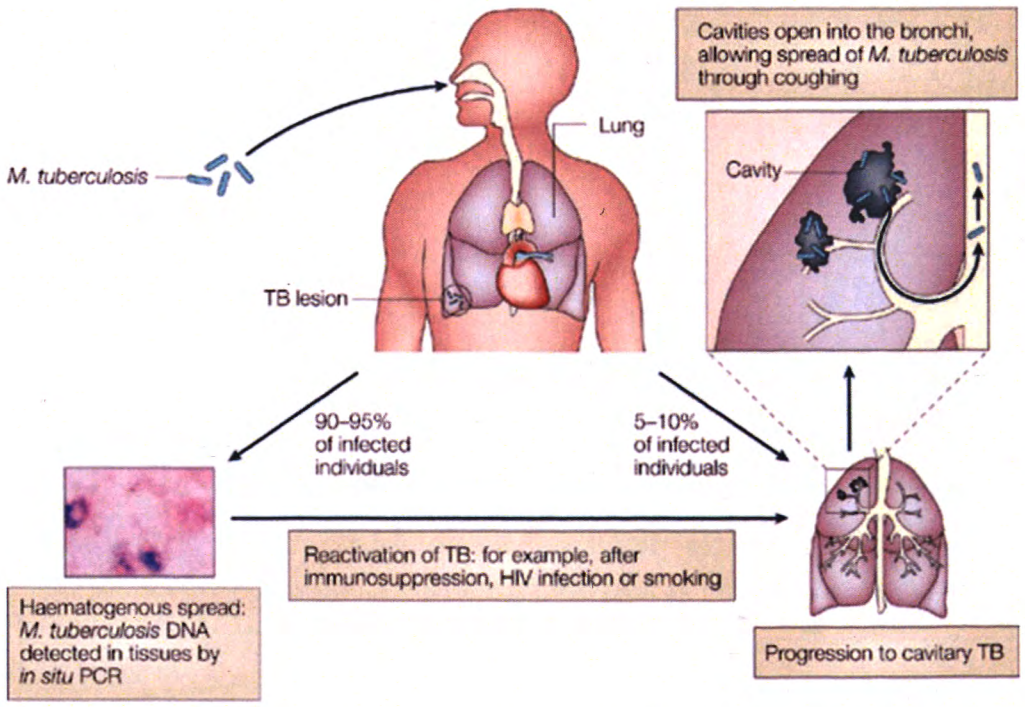

Figure 1.3: *Information graphic on the infection of M. tuberculosis.* Transmission of TB infections is generally through inhalation. As TB infects the lower respiratory tract, it leads to the formation of TB lesions in the lungs. Most TB infections can be cured with proper antibiotics treatment. However, the reactivation of TB and a minority of TB cases may progress to cavitary TB. This figure is reused from Rook *et. al* (2005) [60].

T-cell mediated immune response drives the formation of a calcified tuberculous caseating granuloma, clinically termed as the Ghon complex, which has the capability to confine and restrain the growth of *M. tuberculosis* thereby leading to healing [32]. This Ghon complex is made up of a collection of epithelioid cells, lymphocytes and capillaries. It was also proposed that these calcified tuberculous caseating granulomas may have a certain burden of bacteria, within which, *M. tuberculosis* will be unable to continue in proliferation [3]. The burden of bacteria refers to the ability of the host

granulomas in containing *M. tuberculosis* [61]. However, it is also important to note that the notion of a burden of bacteria was only experimented on NHPs [61]. Also, it is uncertain if humans would manifest such observations. Nonetheless, in cases where there is no substantial tissue injury caused by an infectious granuloma (observed in chest radiography scans), patients presenting an infectious granuloma can still be treated [3]. These patients are categorized as LTBI patients with controlled asymptomatic infection [3], in which they were also tested to be TST and IGRA positive [28]. However, the progression of the formation of an infectious granuloma were only confirmed in mice in which they presented large infectious granulomas and more studies are needed to understand if this occurrence is similar to that of humans [62]. Preventive treatments are then provided to LTBI patients such that the disease progression to active TB is reduced [26]. To date, some countries have accepted the TB preventive therapy, also known as the Isoniazid Preventive Therapy (IPT) [63]. In this study, the patients subjected to this therapy were those who had been tested positive in TST as well as with presence of radiographic lesions (of probable TB origin). It was concluded that with a strict regimen on isoniazid, the progression of LTBI to active TB was significantly reduced [63].

Out of these, there are also a few exceptional cases where the infection can progress to active TB disease [3, 64] (Figure 1.2, part 5). The term exceptional refers to situations where an LTBI patient is immuno-compromised [65]. The presence of conserved T-cell antigens in *M. tuberculosis* [66], HIV infection, treatment with tumor necrotic factor alpha (TNFα) neutralizing antibodies as well as inborn genetic errors [67] have been proposed to result in the progression from LTBI to active TB disease [3] (Figure 1.3). Detailed information of each factors are explained in the next section.

1.3.1 Pathogenesis of *M. tuberculosis* in causing pulmonary TB – Presence of T-cell antigens

Little is known about the presence of conserved T-cell antigens in *M. tuberculosis* and its relation to disease progression. Theoretically, viruses with reduced antigenic variation and immune evasion may result in their reduced ability in rendering an infection [68]. Instead, one study proposed that the T-cell antigens present in *M. tuberculosis* which are responsible for interaction with human T-cells are highly conserved [66]. The same study also suggested that the presence of highly conserved T-cell antigens is necessary for human T lymphocytes recognition to elicit a type I

interferon immune response by the host, which in turn triggers *M. tuberculosis* disease progression from LTBI to active TB [66].

1.3.2 Pathogenesis of *M. tuberculosis* in causing pulmonary TB – Coinfection with HIV

HIV infection usually results in sparse numbers of $CD4^+$ T-cells. As such, patients with HIV infection are more prone to TB infection and disease progression which may eventually lead to increased chances of mortality.

1.3.3 Pathogenesis of *M. tuberculosis* in causing pulmonary TB – TNFα

TNFα is one of a few cytokines produced by monocyte-derived macrophages when a host is exposed to *M. tuberculosis* infection [69]. Studies performed in murine *M. tuberculosis* have shown that the absence of TNFα results in the formation of granulomas [70]. Furthermore, *in vitro* studies have shown that the production of TNFα was able to eliminate mycobacteria and at the same time, prevent the spreading of the pathogen [71]. In yet another mutational study, murine models tested with TNF knockouts were found to be unable to form granulomas, suggesting the lack of an innate immune response [72]. These studies have shown the necessity of TNFα in the containment of *M. tuberculosis* infection through *M. tuberculosis* specific antigen T-cell response [73]. However, the above studies were limited to *M. tuberculosis* infection in the liver. Unlike TB infection in the liver, studies in relation to pulmonary TB revealed that the decline in TNFα production resulted in increased pulmonary inflammation, pulmonary cell damage and/or mortality [74]. Furthermore, the amount of TNFα plays a role as to whether TNFα functions as a protective mechanism or causes an increase in immunopathology [75]. It was found that the excess of TNFα production induces systemic inflammation rather than protecting the host, thereby leading to the manifestation of clinical cachexia [76]. Here, it highly suggests that an adequate amount, but not excessive, of TNFα production is crucial to control TB progression.

In patients suffering from moderate to severe rheumatoid arthritis and do not respond to anti-rheumatic drugs or methotrexate therapy, were instead, given anti-TNFα therapy [77]. However, the utilization of anti-TNFα treatment was found to facilitate in the progression of TB infections in patients being treated for rheumatoid arthritis wherein the antibodies bind to TNFα, leading to reduced TNFα function [78]. In particular, the data presented revealed that these patients on anti-TNFα therapy may

progress to develop active TB when exposed to infectious TB or has LTBI [79, 80]. These studies highly suggest that anti-TNFα therapies inhibits the protective mechanism of TNFα against *M. tuberculosis* infection. Thereby, this leads to an increased chance of TB disease infection or progression when exposed to infectious TB [81].

1.3.4 Pathogenesis of *M. tuberculosis* in causing pulmonary TB – Inborn genetic mutations

Inborn genetic mutations, which carries mutations that affects either the accessory chain of IFN-γR or the IFN-γ receptor, may render a patient to be more susceptible to TB progression [82, 83]. Some genes encoding proteins such as gp130 have been shown to participate in the defense mechanism against *M. tuberculosis* infection, especially those along the IL-12-IFNγ axis, whilst deletion or mutation in this protein were linked to the progression of LTBI to active TB [84-87]. Nonetheless, all the above are postulations and more studies should be performed to further understand the mechanism of infection leading to the progression of active TB.

LTBI reactivation, on the other hand, is generally associated with the liquefaction of previously formed granulomas and the eventual rupture into the bronchoalveolar and vascular system [32, 88, 89]. This suggests the plausibility of *M. tuberculosis* dissemination in the host organs which leads to a second infection.

1.4 Treatments for TB infection and the emergence of *M. tuberculosis* resistance

Vaccination for TB have seen the light since 1921 and anti-tubular drugs were first discovered in 1950 [90]. The current and only approved TB vaccine is the *Mycobacterium bovis* (*M. bovis*) Bacillus Calmette-Guérin (BCG) [91].

Despite being the most widely used vaccine, BCG still has its limitations. Studies performed have confirmed the effectiveness of BCG vaccination in infants [92, 93] and it was shown that the efficacy of BCG vaccination in adolescents and adults varies from 0-80% [94]. Despite presenting such high efficacy, meta-analysis performed showed that the protective efficacy of BCG vaccination wanes with time [95, 96]. Furthermore, it was found that there were insufficient evidence of the effectiveness of BCG vaccination after 10 years from being vaccinated [97]. Of significance is the efficacy of BCG vaccination in adults, in which it was proven to be less effective in developing world in which they carry the highest incidence of infectious TB cases [98, 99]. Overall,

the above studies provided evidence that there are limitations on this widely used vaccination, BCG.

To overcome the limitations of BCG vaccinations, research scientists around the world are focusing on designing alternatives and/or improvements on BCG vaccination. One such vaccination (recombinant BCG30; rBCG30) currently undergoing clinical trials utilizes the over-expression of antigen 85B (Ag85B) [100, 101]. Scientists have tested rBCG30 on HIV-positive individuals and have also found an improved efficacy and is generally safer for HIV-positive individuals [102]. However, the vaccination is still on hold at clinical trials phase despite being tested to show immunogenicity (against TB) in humans and improved protection (against TB) in guinea pigs [103]. Attempts were made to improve rBCG30 in which the focus was the addition of immunodominant genes such as Ag85A and TB10.4 as well as the expression of perfringolysin O [104]. This improved vaccination (Aeras-422) revealed improved efficacy as compared to BCG when tested with mice and guinea pigs. However, Aeras-422 was stopped in clinical trials phase I due to the adverse side effects observed in patients [105]. With the same strategy of utilizing recombinant BCG, other recombination attempts were made. One such is the VPM 1002, which is currently undergoing clinical trials phase IIa. VPM 1002 employs the improvement of cytolytic T-cell responses through the secretion of listeriolysin [106, 107] as well as the deletion of Urease C [108].

Apart from using rBCG vaccination techniques, current development for TB vaccines also targets booster vaccinations such as the utilization of fusion protein (fusion of proteins such as Ag85B, ESAT-6, Rv2660C, Rv1196, Rv0125 and TB10.4) or viral-vector (viral factors such as replication deficient adenovirus 5, replication deficient adenovirus 35 or Ankara) for pre-exposure to booster vaccinations [92]. The detailed explanation and references are shown in the table below.

Type	**Vaccination candidate**	**Description**		**References**
Fusion proteins delivered in adjuvant		***Adjuvant***	***Fusion protiens***	
	HyVac4:IC31	IC31	Ag85B and TB10.4	[109, 110]
	Hybrid 1 + IC31	IC31	Ag85B and ESAT-6	[111]
	Hybrid 56 + IC31	IC31	Ag85B, ESAT-6 and Rv2660c	[112]

	M72 + AS01	AS01	Rv1196 and Rv0125	[113, 114]
	M72 +AS02	AS02		
Utilization of viral factors		***Virus***	***Expressed proteins***	
	AdAg85A	Replication-deficient adenovirus 5	Ag85A	[115]
	Aeras-402	Replication-deficient adenovirus 35	Ag85A, Ag85B and TB10.4	[116, 117]
	Aeras 485	Modified Ankara vaccinia	Ag85A	[118]

Despite various booster vaccinations development, most of these booster vaccinations are currently either undergoing clinical trials phase or have no current updates as to whether the clinical trials are completed or on hold. Apart from findings on booster vaccinations, scientists have also opted for the usage of whole bacterial which are either detoxified or inactivated [92]. Two such advanced vaccinations are RUTI and *M. vaccae* [119]. RUTI utilizes fragmented and detoxified *M. tuberculosis* cells and are targeted for LTBI patients [119, 120]. In LTBI patients, *M. tuberculosis* are in the latent form and when patients are treated with RUTI, an immunological response will be triggered against the antigens found on the latent *M. tuberculosis* [121]. Clinical trials have proceeded to ascertain the effectiveness of RUTI and is currently undergoing phase IIa clinical trials [122]. *M. vaccae* is utilized as a vaccination, wherein the whole-cell was inactivated and used alongside immunotherapy [120, 123]. It was found that the inactivated *M. vaccae* vaccination triggers a cellular immune response in which the T-helper 1 (Th1) response between the tubercle bacilli and host tissues are upregulated, whereas the T-helper 2 (Th2) mechanisms specific to the bacilli antigens are down-regulated [123].

As shown from the above, despite having multiple vaccinations developed to prevent the dissemination of TB, only one (BCG) has been approved for usage so far. Moving forward, apart from preventing TB infection through vaccinations, what are the current available drugs to treat TB infections?

The four first-line of antimicrobials treatment for TB are isoniazid (INH), rifampicin (RMP), pyrazinamide and ethambutol [124]. Through the years, researchers are continuously searching for alternative drugs to target TB infection. In recent years, bedaquiline [125, 126] and delamanid [127-129] have been approved to target multi-drug resistant tuberculosis [130, 131]. Yet, the rising number of cases reported for resistant *M. tuberculosis* strains is still a huge cause of concern [132].

The emergence of resistant *M. tuberculosis* was first observed in patients diagnosed with pulmonary TB, where streptomycin was utilized for treatment [133]. Unfortunately, this has upregulated to even resistance to first-line antimicrobials and/or second-line antimicrobials [134]. Wild *M. tuberculosis* was observed to have lower spontaneous mutation rates [135] and there have been no data available about the DNA acquisition by *M. tuberculosis* [3]. Nonetheless, a study performed have revealed the presence of mutations on single genes that could lead to drug resistance [136]. However, this study does not highlight the relationship between the mutations and drug resistance, it only suggests the possibility of allelic exchange. In recent years, a review performed on eight crucial genes refuted this proposal [137]. Therefore, the next question is, what would then result in the emergence of drug resistant *M. tuberculosis*? The selection for *M. tuberculosis* resistance was largely due to non-compliance of chemotherapy in patients [138]. Apart from patient non-compliance, poor infection control could possibly lead to the emergence of resistant *M. tuberculosis* [139-142]. The access to self-medication where patients do not require prescription to purchase anti-TB drugs also plays a part in the emergence of resistance [143, 144]. In addition, the negligent usage of antibiotics in which either the patient does not complete the course of antibiotics or the misuse of antibiotics (by health professionals, unskilled practitioners or private practitioners) would further allow pathogens to develop resistance towards antibiotics [145-147].

In view of the increasing incidence of resistance towards antimicrobials in *M. tuberculosis*, WHO has established the "STOP TB Strategy". There are six main strategies employed: i) Moving towards the enhancement and expansion of Directly Observed Treatment (DOTS), ii) Engaging the public as well as health care workers in the promotion of standards of care for TB patients, iii) Engaging the community to empower their knowledge in the prevention of TB cases as well as TB treatment in patients, iv) Promoting and enabling research to develop new vaccines/drugs/diagnostic tools, v) Targeting MDR-TB, TB/HIV as well as TB endemic populations and lastly, vi)

Improving primary health care through contributions made to health sectors [148]. In line with the STOP TB strategy, a patient-centered approach was suggested particularly for coinfection of HIV with drug resistant TB [149]. This approach utilizes strategies of DOTS, however, with the implementation of education and patients counselling, especially where HIV is a social stigma [149]. In addition, three other organizations have also implemented research as a fundamental to improve diagnosis, treatment as well as development of healthcare interventions [150-152].

1.5 Emergence of MDR and XDR *M. tuberculosis*

The emergence of multi-drug resistance TB (MDR-TB) became particularly evident in 1985, in USA, where there were increased cases of TB mortality and patients who are unresponsive to TB drugs [153]. Apart from USA, WHO has also observed the emergence of MDR-TB worldwide [154]. MDR-TB is defined as patients conferring resistance to two first-line treatments: INH and RMP [155]. MDR-TB patients requires the treatment with second-line drugs which were found to be more costly and also the requirement of long-term therapy as compared to first-line drugs [156]. Second-line treatments usually includes the combination of fluoroquinolones (gatifloxacin, levofloxacin or monofloxacin), injectable agents (kanamycin, capreomycin or amikacin) as well as anti-TB drugs (clofazimine, linezolid, terizidone, ethionamide, cycloserine or prothioamide) [3].

However, due to the cost and requirement of long-term therapy required for MDR-TB, approximately 46% of patients are found to not have completed the full therapy [157]. As a result, resistance has broadened to extensively drug resistant TB (XDR-TB), which was observed in 2006 [134]. XDR-TB is defined as the inclusion of MDR-TB, resistance to FQs as well as resistance to one or more injectable second-line TB drugs (capreomycin, kanamycin and/or amikacin) [153].

Despite the emergence of MDR-TB and XDR-TB, not all countries in the world are at epidemic levels of MDR/XDR-TB [158]. Nonetheless, the global burden of drug resistant TB is still high. In one report published in 2008 by WHO and the International Union Against Tuberculosis and Lung Disease Global Project [159], it was reported that out of all the reported TB cases, MDR-TB holds up to 4.8%. Of which, India and China accounts for approximately 50% of the cases whilst the Russian Federation, another 7%. Statistically, 86% of the world's MDR-TB burden is shared amongst 27 countries. This was significantly higher by almost half a million cases in 2006 as compared to the 2004

estimates. In 2004, India, China and the Russian Federation held approximately 62% of the global burden. In a more recent report by WHO in 2016, it was found that the global burden of MDR-TB is approximately 3.3%, in which central Asia and Eastern Europe are facing MDR-TB epidemic [132].

All the above-mentioned statistics prove that MDR-TB remains a threat to many provinces in China and the former Soviet Union. In addition, there are also lesser data available on drug resistance available in South Africa. This further reinforces the need to find a better treatment for MDR-TB [2].

1.5.1 Resistance of *M. tuberculosis* with INH-treatments in patients

The most common cause of MDR-TB is the resistance to INH; the front-line TB drug. INH is a pro-drug that requires *in vivo* activation by *katG* [160]. INH activation results from the removal of a hydrazine group on INH, which is mediated by *katG* [161]. The utilization of active INH generates electrophilic and reactive species (peroxide, superoxide, hydroxyl radical, nitric oxide, isonicotinic-acyl anion or radicals) [162-164]. The susceptibility of *M. tuberculosis* is due to the presence of these highly reactive electrophilic and/or reactive species generated upon *katG*-mediated INH activation [135]. *In vivo* and *in vitro* mutational studies have suggested that the target of INH in *M. tuberculosis* is the presence of enoyl-acyl carrier protein reductase (InhA) as well as the β-ketoacyl-acyl carrier protein synthase (KasA) [165-167]. Both of which were shown to be crucial in mycolic acid biosynthesis, which is essential for the formation of the mycobacterial-envelope architecture [165]. The activation of INH subsequently leads to the inhibition of mycolic acid biosynthesis in *M. tuberculosis* [168]. Without proper formation of the mycobacterial-envelope architecture, it exposes *M. tuberculosis* to the formation of defective layers of the mycobacterial-envelope [168] which compromises the pathogen against the environmental stresses as well as oxygen radicals of the host [169].

Apart from being the only protein capable of mediating the activation of INH, *katG* is an essential enzyme for *M. tuberculosis* whereby it functions as a catalase and peroxidase [170]. Studies have shown the close association of mutations in *katG* and clinically isolated INH-resistant TB strains [171, 172]. In particular, two amino acid substitutions were found to implicate the activity of *katG*: amino acid 315 (Serine to Threonine) and 463 (Arginine to Leucine) [172, 173]. An alternative mechanism was proposed by another study revealing that, instead of amino acid substitution, missense

mutations were found in *katG*, particularly at the site of amino acid 463 [174]. Nonetheless, both postulations found that apart from mutations found in *katG*, there were also mutations found on InhA, which lies upstream of *katG*, that may also lead to resistance to INH [173]. Furthermore, the deletion or point mutations of *katG* and/or InhA were shown to reduce the peroxidatic function of *katG* [175, 176]. Therefore, for *M. tuberculosis* to survive in the highly oxidative environment of the macrophages, it highly suggests that *M. tuberculosis* must compensate for the reduced peroxidatic function of *katG*.

Moving forward, studies have suggested the intense pressure of selection of the function of *katG* by the host macrophages [177]. Herein, it was found that in INH-resistant patients, deletion or point mutations in *katG* may still retain the function of *katG* alongside reducing the toxicity of INH [178]. Although the exact molecular mechanism of INH resistance has not been fully confirmed to date, studies performed thus far, have highlighted the correlation between mutated or deleted *katG* and INH resistance. The next question that arises would be, what is the alternative mechanism utilized by *M. tuberculosis* to compensate for the reduced peroxidatic function of *katG* when patients are treated with INH?

It was found in one study that *katG* knockout mutants and INH-resistant mutants expressed a protein: the alkyl-hydroperoxidase reductase subunit C (AhpC) [179]. Previous studies performed have not found evidence leading to the overexpression of AhpC *in vitro* (unpublished data), yet another study revealed that it was due to the lack of passage through liquid culture or animals [179]. Evidence has shown, that the overexpression of AhpC was largely found in the 5' promoter region of AhpC [179]. In particular, in *katG* knockout strains, the 5' promoter sequence had approximately 9-20 folds of increased activity as compared to the wild-type strains [179]. This highlights that the increased expression of AhpC is necessary to compensate for the loss of function in *katG* deficient or mutant strains [180].

1.6 Introduction to AhpCs; a class of peroxiredoxins

AhpCs are classified as a class of peroxiredoxins. Peroxiredoxins are cysteine-based peroxidases, also known as ubiquitous enzymes that do not require cofactors in their catalysis [181]. In recent years, the emergence of a better understanding of the alkyl-hydroperoxide-reductase has provided insights into the mechanistic action of peroxiredoxins. Commonly found in most eubacteria and archaea [182], peroxiredoxins are usually expressed in prominent level despite having lesser catalytic efficiency as compared to glutathione peroxidases. Despite so, the detoxification of endogenously generated hydrogen peroxide (H_2O_2) was found to have been performed largely by peroxiredoxins [183].

Peroxiredoxins vary in oligomeric states and interfaces depending on the location of the resolving cysteine. The high expression of peroxiredoxins led to the classifications of peroxiredoxins into three main classes; the typical 2-Cys peroxiredoxins, atypical 2-Cys peroxiredoxins and 1-Cys peroxiredoxins [183]. Classifications of these peroxiredoxins are based on the number and location of the cysteine residues involved in catalysis. These cysteines are the peroxidatic cysteine (C_P) and the resolving cysteine (C_R). The main difference between peroxiredoxins and glutathione peroxidase is the presence of conformational changes between a locally-unfolded (LU) and fully-folded (FF) conformation (Figure 1.4A) [183]. This conformational change exposes the cysteine residues such that an inter-subunit disulfide bond can form within the C_P and C_R. A typical peroxidase catalysis involves peroxidation, resolution and recycling [184]. The first step of peroxidation occurs when the peroxidase is in the FF conformation holding four conserved residues; C_P, arginine, threonine and proline [183]. C_P is located within a universally-conserved PxxxTxxC motif that would bind to hydroperoxide substrates. Here, the thiolate anion would then be oxidized to cysteine-sulfenic acid (C_P-SOH). The presence of a LU conformational state allows the C_P to be exposed to the C_R, which subsequently allows the C_R to attack C_P-SOH. This is when the resolution reaction occurs to release water and a condensation reaction whereby an inter-subunit disulfide bond is formed. Consequently, the cycle is completed after the regeneration of free thiol forms of C_P and C_R, wherein the disulfide bond between the C_P and C_R is reduced by another reductant (Figure 1.4B). Studies have proposed that the stabilization of the FF conformation effectively promotes the oxidation of the C_P by the peroxide in the active site [185].

The majority of soluble peroxiredoxins are in a redox-modulated equilibrium of dimers and decamers, and referred to as the typical 2-Cys peroxiredoxins [183, 186]. In the typical 2-Cys peroxiredoxins, the resolving C_R is located at the C-terminus of the second chain of the dimeric subunit. This cysteine residue is crucial in the formation of an inter-subunit disulfide bond with the C_P during catalysis. Unlike the typical 2-Cys peroxiredoxins, the atypical class of peroxiredoxins forms an intramolecular subunit disulfide bond, whilst the 1-Cys peroxiredoxins usually involves only the C_P for catalysis. Here, the C_P is involved in a transient reaction, necessary for condensation reaction to happen [184].

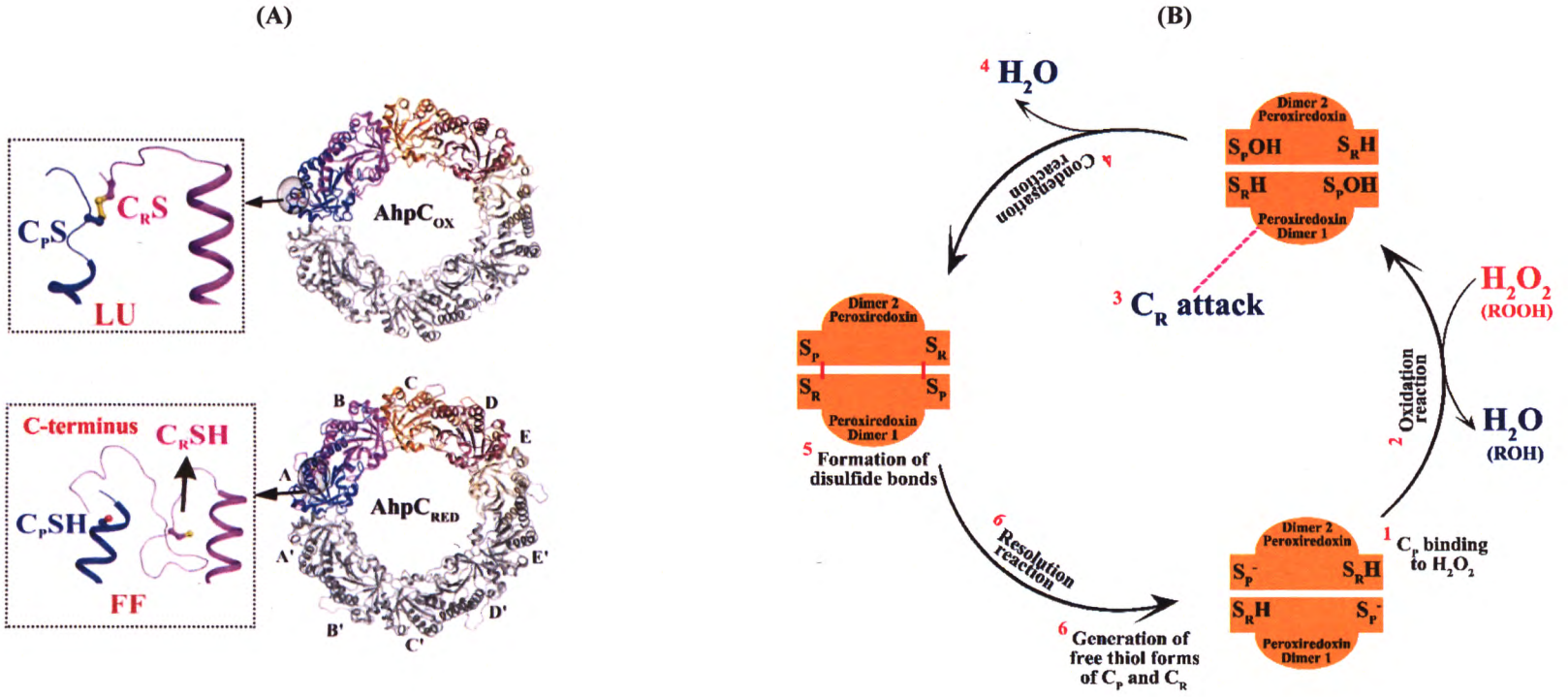

***Figure 1.4*: (*A*)** A representative figure using the crystallographic structures of *Ec*AhpC revealing the LU and FF conformations of the peroxiredoxin. In *Ec*AhpC$_{OX}$, C_R is in its -SOH intermediate state, ready to interact with C_P and form an inter-subunit disulfide bond. This conformation is reported to be the LU state. In this state, the peroxiredoxin is unable to react with the substrate, H_2O_2. On the other hand, before C_R interacts with C_P, *Ec*AhpC is reduced. *Ec*AhpC$_{RED}$ has its C_P and C_R facing away from each other. This conformation is reported to be the FF state. *Ec*AhpC$_{RED}$ is then able to reduce H_2O_2 to H_2O and thereby form a -SOH intermediate. This figure is adapted and modified from Nartey *et al.* (2015) [187] **(*B*)** A representative figure showing the process of H_2O_2 reduction by peroxiredoxins. There are three main reactions occurring in the typical 2-Cys peroxidase catalysis; oxidation, condensation and resolution. Firstly, the peroxiredoxin (in its FF conformation) will bind to H_2O_2 (*labelled 1*) and this leads to the oxidation reaction (*labelled 2*) in which it forms an C_P-SOH intermediate. Hereafter, it forms a LU conformation. Next, the exposure of the C_P to C_R allows the C_R to attack the C_P (*labelled 3*), and subsequently, undergo a condensation reaction where H_2O is released (*labelled 4*). After the condensation reaction, an inter-subunit disulfide bond is formed (*labelled 5*). Thereupon, the peroxiredoxin then undergoes a resolution reaction. This cycle is completed after the recycling of free thiol forms of C_P and C_R (*labelled 6*) and the disulfide bond between C_P and C_R is reduced by another reductant, wherein this releases the reduced form of the peroxiredoxin.

1.6.1 Alkyl-hydroperoxidase reductase subunit C (AhpC)

AhpCs are mechanistically complex in which the switch in quaternary structure allows the peroxidase to be stabilized in the catalytic states [181]. One example of such shift in quaternary structure is the oligomerization from a dimeric to decameric AhpC in *Salmonella typhimurium* (*S. typhimurium*; *St*AhpC) and *Escherichia coli* (*E. coli*; *Ec*AhpC) [186, 188]. During disulfide bond formation, *St*AhpC would lose its decameric interface. This redox modulation occurs wherein the reduced form of AhpC would oligomerize into a decamer and the oxidized form would remain as a dimer [184]. This redox-oligomerization has also been observed for many peroxiredoxins in mammalian and plant-derived 2-Cys peroxiredoxins [181]. Despite this, few studies have fully understood the physiological role of such transitions. Nonetheless, studies performed suggest that the presence of the decamer stabilizes the peroxidases.

Apart from understanding the redox-sensitive oligomerization in the typical 2-Cys peroxiredoxins, it is also crucial to understand the molecular function of the protein. Few studies have fully understood the function of AhpC in prokaryotes. Being one of the most abundant antioxidant protein in *Helicobacter pylori* (*H. pylori*), studies have proposed the switch from a peroxide reductase to a molecular chaperone function [189]. It was observed that when *H. pylori* is exposed to low amount of reactive oxygen radicals, AhpC would decompose these peroxides. However, when faced with a long-term stress, some of the AhpC proteins present in the bacteria would then be converted to molecular chaperones. This helps to prevent the bacteria from expressing misfolded or unfolded proteins. In addition, excessive amount of oxygen radical stresses may force all the AhpC proteins present to be converted to molecular chaperones. This switch from a peroxide reductase to molecular chaperone function helps to salvage some of the damaged proteins in *H. pylori*. In addition, this shift to a molecular chaperone is also observed in human peroxiredoxin 2 [190]. The presence of a specific cleavage in peroxiredoxin 2 has been proposed to cause the functional switch.

To fully understand AhpC, it is necessary to understand the peroxide reductase activity of AhpC. In *St*AhpC and *Ec*AhpC, it is understood that AhpC functions together with a flavoprotein, AhpF [187, 191]. The peroxide reductase activity of AhpC in these two bacteria is known to be flavin-dependent. In the well-studied *Ec*AhpC system, it is understood that the alkyl-hydroperoxide-reductase (AhpR) system involves both AhpC and AhpF to fully detoxify reactive oxygen radicals. The antioxidant system of *E. coli* is shown in Figure 1.5.

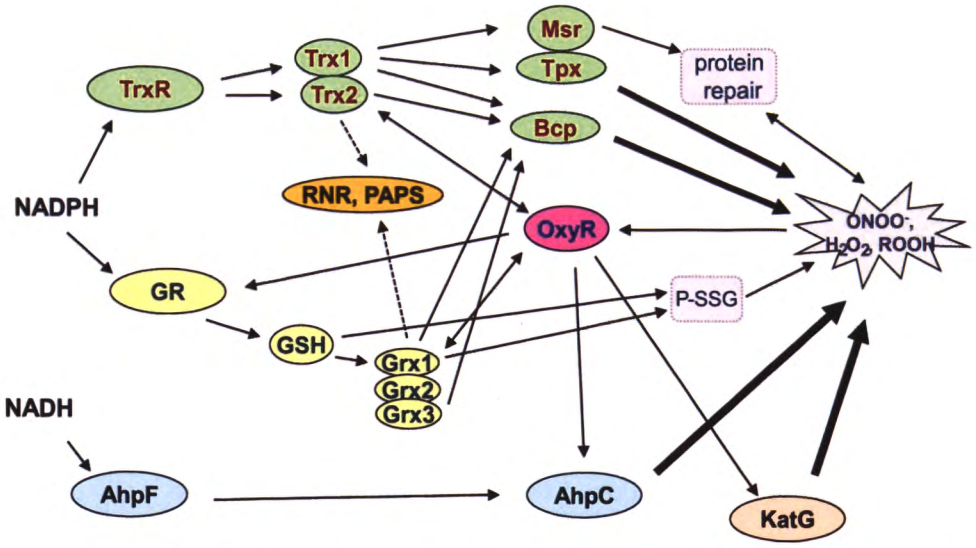

Figure 1.5: *Schematic drawing of the antioxidant systems in E. coli.* H_2O_2 can be effectively reduced with the thioredoxin reductase (TrxR) system, GSH antioxidant system as well as AhpF system. The TrxR system utilizes Trx1, Trx2 as well as three major thiol peroxidases (Msr, TPx and Bcp). The GSH antioxidant system encompasses three glutaredoxins (Grx1, Grx2 and Grx3). AhpF works alongside AhpC to reduce H_2O_2. *E. coli* OxyR is the main transcription factor that regulates the expression of Trx2, Grx1, GR and AhpC. This figure is reused from Lu, J. & Holmgren, A., 2014 [192].

1.6.2 *M. tuberculosis* Alkyl-hydroperoxidase reductase subunit C *(Mt*AhpC*)*

Unlike studies performed on *St*AhpC, *Hp*AhpC and *Ec*AhpC, little has been understood about the mechanism of *Mt*AhpC [180]. However, it was proposed that unlike the typical 2-Cys peroxiredoxins, *Mt*AhpC is unique, particularly in its structure [193].

Firstly, *Mt*AhpC has three cysteine residues unlike most 2-Cys peroxiredoxins, wherein they present only two cysteine residues. The conserved C_P is C61 while the conserved C_R is C174. However, *Mt*AhpC presents an additional cysteine, C176 (Figure 1.6A). Little is understood about the function of C176. However, an alternative proposal was brought up, which suggests the likelihood of the third cysteine to be involved in the formation of an intramolecular disulfide bond [180]. In a study performed by Koshkin *et al.* (2003) [194], it was proposed that C133 of AhpD is involved in the attack of C61-C174. This attack would result in the formation of a AhpD-C133-AhpC-C61 adduct. As such, studies have correlated the formation of this adduct with the plausibility of C176 to be involved in the disulfide bond formation. Here, it was proposed that C176 is involved in the sulfhydryl group attack of C61-C174, thereby forming an intramolecular disulfide bond between C174-C176 [180].

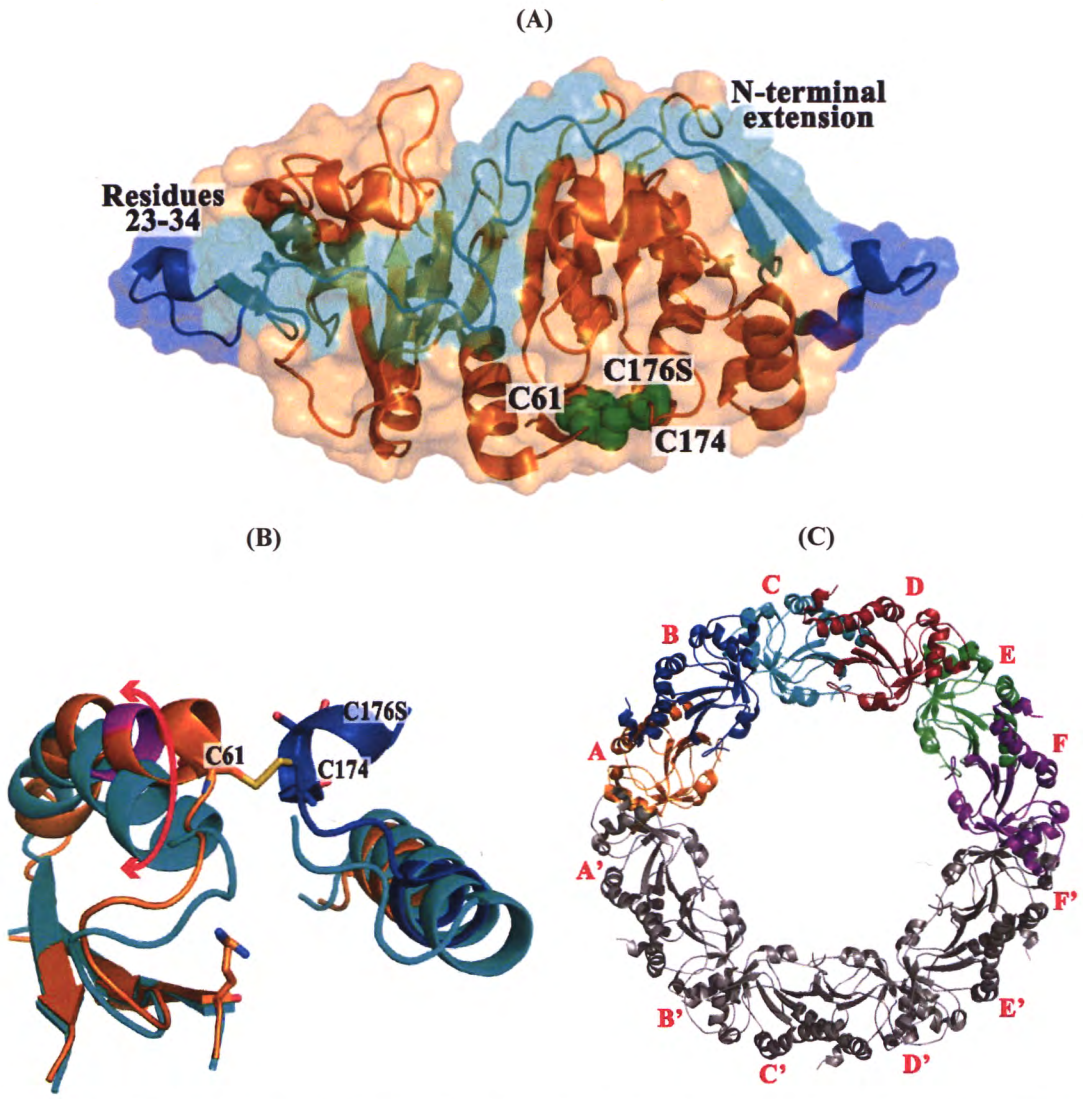

***Figure 1.6**: Cartoon and surface representations of the crystallographic structure of MtAhpC$_{C176S}$ (PDB ID: 2BMX) [180] in alignment with EcAhpC (PDB ID: 4O5R) [188].* **(*A*)** Dimeric subunit of *Mt*AhpC$_{C176S}$ consists of two cysteine residues, C61 and C174, alongside with a point mutation at C176 to serine (*represented with green spheres*). In the current study, the focus is on the additional N-terminal extension from residues 1-40 (*labelled N-terminus extension, represented in cyan*), is highly conserved only in mycobacteria. The second focus is on the loop region (*labelled residues 23-34, represented in dark blue*). **(*B*)** The up-close structure of the catalytic site of *Mt*AhpC$_{C176S}$. When compared with *Ec*AhpC (*represented in cyan*), *Mt*AhpC$_{C176S}$ (*represented in orange and dark blue for each subunit*) undergoes a rigid body movement in helix α1 (*represented in magenta, with red arrows*). This movement facilitates the formation of disulfide bonds between the two subunits (*represented in yellow*). **(*C*)** Unlike other typical 2-Cys peroxiredoxins, the proposed crystallographic structure of *Mt*AhpC$_{C176S}$ is a dodecamer (*each subunit is labelled as per written*). A, B, C, D, E, F (*represented in assorted colors of orange-yellow, dark blue, cyan, brown, red, green and purple, respectively*) are labelled on each subunit and its symmetric mates are labelled as A', B', C', D', E', F' (*represented in grey*).

Secondly, unlike *St*AhpC, the catalysis of *Mt*AhpC was proposed to be involved in a rigid body movement instead of local unwinding [193]. Studies have proposed that the local unwinding in *St*AhpC renders the C_P to be accessible for the formation of a disulfide bond. However, in *Mt*AhpC, the formation of a disulfide bond between C61

and C174 is achieved through the rigid body movement of helix α1 (Figure 1.6B). This rigid body movement exposes a small cavity in which it allows C61 to be in contact with C174 for a catalytic cycle to be achieved. In the same study, it was also proposed that the intramolecular disulfide bond formation between C174-C176 releases the helix α1 to a more favorable position [193]. This exposes AhpC to be involved in a reduction reaction by an external thiol. Since the studies performed by far only proposed the importance of the rigid body movement, it is necessary to understand the importance of maintaining the cavity for the formation of disulfide bonds.

Thirdly, *Mt*AhpC has been proposed to form a dodecamer instead of a decamer (Figure 1.6C). In the reported crystallographic structure of the *Mt*AhpC$_{C176S}$ mutant (PDB ID: 2BMX) [193], crystal forces were proposed to play a part in the formation of a dodecamer. However, no studies of *Mt*AhpC in solution have been performed thus far [193]. In addition, it is not fully understood if the presence of this decamer/dodecamer is crucial in the enzymatic function of *Mt*AhpC. Therefore, the question here is, that if *Mt*AhpC forms a dodecamer in solution, is this dodecameric ring crucial in maintaining the activity of the protein and/or the interaction with AhpD or TrxC? The interaction of *Mt*AhpC with AhpD or TrxC are described in more details below. Moreover, in the reported crystallographic structure, there are approximately 25 amino acid residues not resolved in the C-terminus. If so, resolving the full crystallographic structure of *Mt*AhpC may provide insights into whether the C-terminal plays a role in oligomerization and/or its interaction with AhpD or TrxC.

Fourthly, *Mt*AhpC presents additional residues in its N-terminus in comparison to AhpCs from other bacteria (such as *Ec*AhpC, *St*AhpC and *Hp*AhpC). Depending on the different sequence alignment algorithms applied, *Mt*AhpC has shown to have additional residues on the N-terminus. In addition to the previous study performed [195, 196], it was observed that the unique N-terminus also carries an additional loop at residues 23-34 (Figure 1.6A). The results revealed that the deletion of residues in this loop have resulted in the loss of redox-oligomerization in *Mb*AhpC. Furthermore, the mutant did not have any enzymatic activity [195, 196]. With such results, it is important to identify the critical amino acids in the N-terminus and/or loop to further understand the unique structure of *Mt*AhpC.

Next, the well-studied *St*AhpC and *Ec*AhpC are reduced by their reduction partner, AhpF [187, 191]. AhpF, which functions as a thiol-dependent antioxidant enzyme is crucial for the antioxidant process [192]. It is understood that the reduction

of the disulfide bond in AhpC by AhpF would then complete the catalytic cycle. However, in *Mt*AhpC, no homologue of AhpF flavoprotein was observed. Instead, on the genome locus where AhpF resides in *S. typhimurium*, AhpD was found in *M. tuberculosis* [180]. AhpD is a thioredoxin-like protein that is found in few organisms. In *Ec*AhpC, the AhpR system proposes the necessity of the AhpC-AhpF interactions for a successful catalytic activity [187]. However, in *Mt*AhpC, the absence of AhpF brings a debate to the reducing partners of AhpC. It was proposed that *Mt*AhpC functions as the foremost element chain, following AhpD, dihydrolipoamide dehydrogenase (Lpd) and dihydrolipoamide succinyltransferase (SucB) (Figure 1.7) [193]. Unlike the studies performed on *Ec*AhpC, few studies have been performed to characterize the interaction between AhpC and AhpD [180]. It is therefore crucial to know what is the reducing partner of *Mt*AhpC, in order to fully characterize the catalytic cycle.

Lastly, the presence of reduction equivalents of the thioredoxin system in *Mt*AhpC is still a debate. Apart from having AhpF as a disulfide bond reductant for AhpC, it was observed that thioredoxin and thioredoxin reductase facilitate the disulfide bond reduction in yeasts alkyl-hydroperoxides [180]. It has been proposed that in *M. tuberculosis*, the thioredoxin system that reduces peroxiredoxins in eukaryotes is inactive [180, 197]. During the experiment performed, it demonstrated that without AhpD or thioredoxins, the addition of hydroperoxide to AhpC did not yield any nicotinamide adenine dinucleotide (NADH) consumption. Although so, yet another study performed by Jaeger *et al.* (2004) showed the plausibility of the reduction of *Mt*AhpC by thioredoxin C (TrxC) (Figure 1.7) [198]. The reported data showed that the catalytic efficiency of *Mt*AhpC reduction of *tert*-butyl hydroperoxide (*t*-BOOH) with TrxC was approximately 5.6 μM [198]. The presence of such contradictory results highlights the importance of the need to study the reduction equivalents with AhpC.

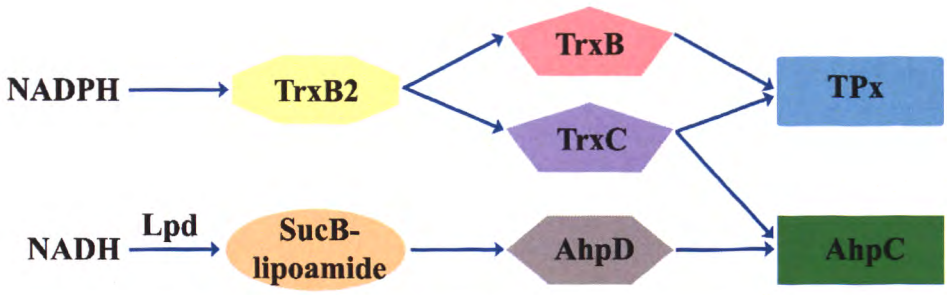

***Figure 1.7**: Schematic drawing of the antioxidant processes in MtAhpC.* AhpC is the main antioxidant system apart from TPx in *M. tuberculosis*. AhpC can be reduced effectively with AhpD [180]. However, the published data thus far, debates as to whether TrxC is the reducing partner of AhpC [180, 198]. In the thioredoxin system, NADPH is the electron donor. The system encompasses TrxB2, TrxB, TrxC and TPx. Instead, the AhpD system utilizes NADH as the electron donor. The antioxidant system functions alongside LpD, SucB lipoamide, AhpD and AhpC.

1.7 Thioredoxin reductase system

The general thioredoxin reductase system comprises of thioredoxin (Trx), thioredoxin reductase (TrxR) and nicotinamide adenine dinucleotide phosphate (NADPH) [192]. Through the disulfide reductase activity of Trx, peroxiredoxins like AhpC are regulated through a dithiol and/or disulfide balance. This in turn helps to protect the bacteria against reactive oxygen radicals [192].

Generally, Trx works coherently with TrxR through a fast-catalytic process. It has been shown that the utilization of the Trx antioxidant functions to protect the cell with various mechanisms [192]. These mechanisms include reducing reductases and regulating the activity of transcription factors that are redox-sensitive. Trxs are 12 kDa reductases and conserved from archaea, bacteria to human. Like the thiol-dependent peroxiredoxins, Trxs also present an active disulfide site, formed at the N-terminal portion of helix α2. Interestingly, this structure fold is common across peroxiredoxins, glutaredoxin and glutathione peroxidase [192]. TrxR on the other hand, is a homodimeric flavoprotein from the pyridine nucleotide-disulfide oxidoreductase family. Typically, there are two main classes of TrxRs; high molecular weight and low molecular weight. Eukaryotes present the higher molecular weight TrxRs, while archaea, bacteria, fungi and plants usually express low molecular weight TrxRs. The molecular weight of each subunit of the former is a 55 kDa protein while the latter is a 35 kDa protein. Structurally, high molecular weight TrxRs consist of a conserved N-terminal CVNVGC-active site and a C-terminal active site. Low molecular weight TrxRs, instead, contain only one active-site that consist of a CXXC-motif (Figure 1.8A).

Through the regulation of the oxidized disulfide and reduced dithiol forms of Trx, AhpC can then be reduced. The oxidized Trx would reduce AhpC whilst the reduced Trx reduces disulfides. NADPH is an important cofactor that is regularly consumed through this ensemble of proteins [199]. The mechanism of reduction varies amongst bacteria. In *E. coli*, TrxA and TrxC works together with glutaredoxin 1 to maintain cellular DNA synthesis. This is achieved through the donation of electrons to ribonucleotide reductase, an essential enzyme [199]. However, *M. tuberculosis* genome does not encode for the glutathione antioxidant system [200]. The absence of glutaredoxin 1 suggests the involvement of Trx and TrxR against oxidative stress. There are three Trx encoded in the genome of *M. tuberculosis* - TrxA, TrxB and TrxC, whilst the TrxR in *M. tuberculosis* is the TrxB2. [201]. Previous studies have shown the reduction of peroxides and dinitrobenzenes as well as the detoxification of hydroperoxides with the Trx antioxidant system in *M. tuberculosis* [197, 198].

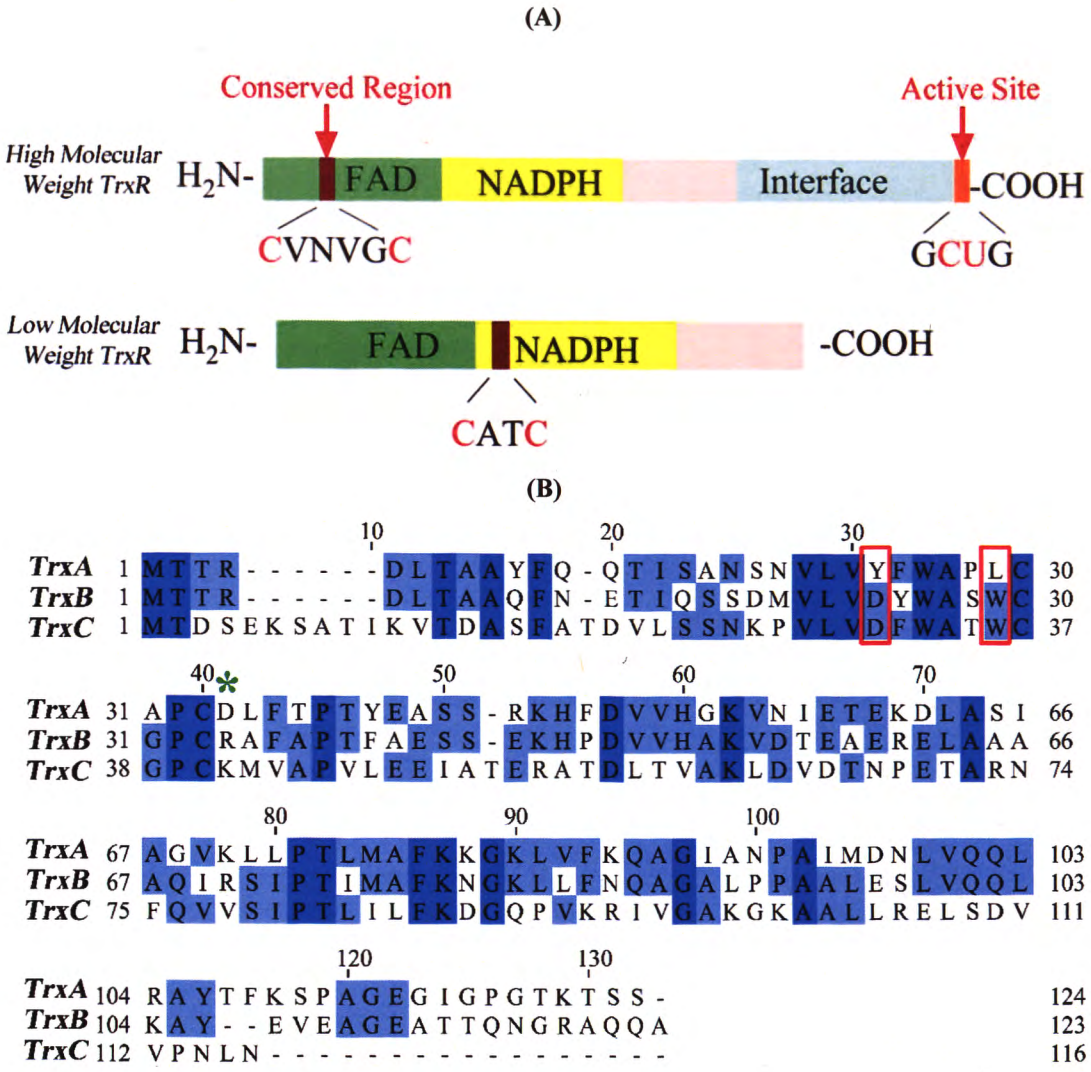

Figure 1.8: *TrxA, TrxB and TrxC conserved regions and sequence alignment.* **(*A*)** Illustration of the differences between high molecular weight TrxRs and low molecular weight TrxRs. Eukaryotic TrxR carries a conserved region, with amino acid CXXXXC. However, bacterial TrxR carries the conserved CATC amino acid region. In addition, eukaryotic TrxR carries a conserved active site that is absent in bacterial TrxR. This figure is adapted and modified from Koshkin *et al.* (2003) [192]. **(*B*)** Multiple sequence alignment of TrxA (Uniprot database: P9WG67), TrxB (Uniprot database: P9WHH1) and TrxC (Uniprot database: A0A045GR31) from the Uniprot database. The sequence alignment is colored based on the sequence similarities amongst the sequences; with the *darkest blue* representing a high sequence similarity and a gradient down to *light blue* representing lower sequence similarity. In comparison to TrxB and TrxC, which carries high similarity sequences when compared with other bacteria, TrxA in mycobacteria is slightly different. The conserved amino acids D27 and W32 in TrxB and TrxC are replaced with tyrosine and leucine, respectively, in TrxA (*highlighted with red box*). It is also important to note that the conserved residues in TrxB and TrxC are also conserved in most bacteria. In addition, on the C-terminal C_R, the conserved residues in TrxB and TrxC are replaced with aspartate (*labelled with green asterisk*).

Interestingly, TrxA has lower activity and is ineffective as an interacting partner for TrxB2. However, the activity of TrxB and TrxC have shown the probability of resistance of *M. tuberculosis* to oxidative stresses. Previous studies have shown variances in sequence alignment of TrxA from *M. tuberculosis* (*Mt*TrxA) in comparison

with TrxB and TrxC (Figure 1.8B) [199]. In addition, the conserved residues of TrxB and TrxC are also observed to be consistent in *E. coli* TrxA (*Ec*TrxA). The W32 and D27 residues in *Ec*TrxA are replaced with L29 and Y24, respectively, in *Mt*TrxA (Figure 1.8B, red box). In addition, the conserved basic residues TrxB (arginine) and TrxC (lysine) are replaced with an aspartate residue on the C_R at the C-terminus (Figure 1.8B, green asterisk). These amino acid differences in the putative redox-active site might explain the lower activity observed in TrxA-TrxB2. Further studies into the active-site electrostatics and pK_a values of the cysteine residues present in TrxA have also proposed the plausibility of a lower reductase activity. In the NADPH-insulin reduction assay, TrxA was also shown not to interact with TrxB2 [199]. This suggests that TrxA may not be the natural interacting partner of TrxB2.

On the other hand, TrxB and TrxC were reduced efficiently by TrxB2. In yet another study performed to characterize Trx, a Michealis-Menten kinetics assay was performed. Results have shown that there were insignificant differences in the Michaelis constant (K_m) or turnover number (k_{cat}) measured between TrxB and TrxC [199]. This highlights the mechanism of the thioredoxin antioxidant system in *M. tuberculosis* in which TrxB or TrxC could be the functional thioredoxins. With such complex mechanism, it is important to identify if TrxB or TrxC could then interact with *Mt*AhpC to reduce H_2O_2.

According to a paper published by Jaeger *et al.* (2004), it was shown that the effective reduction of *Mt*AhpC was achieved by TrxC instead of TrxB [198]. Herein, the kinetics analysis revealed that the reduction of *Mt*AhpC by TrxC was comparable to AhpD, the natural reductant for AhpC. TrxC was also shown to be efficient in reducing another peroxiredoxin; thiol peroxidase (TPx) (Figure 1.7). However, TrxB showed lower affinity and reactivity in the reduction of TPx. Therefore, the significance of TrxC interaction with *Mt*AhpC as well as its interacting residues, is crucial for a good cocktail drug target design.

1.8 Aims of the thesis

The detoxification of H_2O_2 with an alternative pathway through *Mt*AhpC is crucial for the virulence of INH-resistant *M. tuberculosis*. It was shown that the inactivation of *Mt*AhpC increased the susceptibility of *M. tuberculosis* to organic hydroperoxide and peroxynitrite-mediated toxicity [193]. In eubacteria, this system of eliminating excessive organic hydroperoxide is via AhpC and its reductase, AhpF.

However, AhpF is not expressed in *M. tuberculosis*. Instead, two reducing systems have been proposed for *Mt*AhpC; (i) AhpD and (ii) TrxC. This may in part reflect that *Mt*AhpC$_{RED}$ was proposed to form a dodecamer [193] instead of a decamer (like other peroxiredoxins). The sequential steps of AhpD or TrxC binding and electron transfer to *Mt*AhpC are proposed to alter the structural rearrangements of *Mt*AhpC, in order to facilitate electron transfer [180]. Although studies performed thus far have only proposed the plausible interacting partners of wild-type (wt) *Mt*AhpC, no study has highlighted the interacting epitopes between *Mt*AhpC and its interacting partners [180, 198]. Therefore, one of the aims of this study is to visualize the structure of *Mt*AhpC$_{RED}$ through 2D projections with micrographs obtained from electron microscopy, and to develop a crystallization protocol for future atomic structure determination. Structural insights will be extended by nuclear magnetic resonance (NMR) titration assays to identify the epitopes and residues involved in the interaction between AhpC-TrxC, in order to gain insights into the structural rearrangements of *Mt*AhpC and its reducing partners that facilitate electron transfer.

Apart from the difference in the regenerating enzymes of mycobacterial AhpC, the enzyme also differs from other eubacteria, in its broad spectrum of substrate specificity, including H_2O_2, organic hydroperoxides and peroxynitrite. Therefore, it is essential to understand the enzymatic kinetics of the interaction of *Mt*AhpC with different substrates. Thus, the second aim of this study is to perform steady-state and time-resolved peroxidase activity assays with H_2O_2 and *t*-BOOH, in order to highlight its substrate specificity.

Furthermore, in comparison to other AhpCs, *Mt*AhpC differs in length and composition at its N-terminus, in particular by its unique stretch of 15 amino acids as well as by the unique residues 23 to 34. The secondary structure of its N-terminal 40 residues was proposed to bridge the two oligomeric interfaces, in which the catalytic cysteines are located. In order to demonstrate the importance of these residues, amino acid substitutions of charged residues, that have been predicted to form the interaction between AhpC-AhpD or AhpC-TrxC, will be made in the N-terminus of *Mt*AhpC, to investigate the effects of critical N-terminal amino acids in terms of catalysis and its redox-oligomerization. The studies will be performed using biochemical, biophysical and enzymatic approaches.

2. Materials and Methods

Materials and Methods

2.1 MATERIALS

2.1.1 Chemicals

All the chemicals used for this study were of at least analytical grade. Chemicals were purchased from the following companies:

Buffers and salts	Sigma (St. Louis, MO, USA) USB (Sampscott, MA) Fluka (Sigma, Buchs Germany) Roth (Karlsruhe, Germany) Serva (Heidelberg, Germany)
DTT	Sigma (St. Louis, MO, USA)
Pefabloc^{SC}	BIOMOL (Hamburg, Germany)
Agarose, SDS, glycine, APS etc.	Bio-Rad (Hercules, CA, USA)
Antibiotics	Calbiochem, Sigma, Gibco
IPTG	Gold Bio (St. Louis, MO, USA)

2.1.2 Molecular biology materials

Primers	Integrated DNA Technologies (Singapore)
KAPA HIFI DNA polymerase	Kapa Biosystem (Massachusetts, MA, USA)
T4 DNA ligase	Promega (Wisconsin, USA)
QIAprep® Spin Miniprep Kit	QIAGEN (Hilden, Germany)
QIAquick® PCR Purification Kit	QIAGEN (Hilden, Germany)
E. coli plasmid propagation strain	DH5α
E. coli protein production strain	BL21(DE3)
pET-9d plasmid	Professor Gerhard Grüber's laboratory [202]

2.1.3 Chromatography

2.1.3.1 Affinity chromatography

Ni^{2+}-NTA beads	QIAGEN (Hilden, Germany)

2.1.3.2 Size exclusion chromatography

Superdex 75 10/300 GL	GE Healthcare (Uppsala, Sweden)
HiLoad 16/600 Superdex 75 pg	GE Healthcare (Uppsala, Sweden)
Superdex 200 10/300 GL	GE Healthcare (Uppsala, Sweden)
Superdex 200 Increase 10/300 GL	GE Healthcare (Uppsala, Sweden)
XK 16/100 Superdex 200 pg	GE Healthcare (Uppsala, Sweden)

2.1.3.3 Instruments and accessories

ÄKTA FPLC	GE Healthcare (Uppsala, Sweden)
ÄKTA Pure	GE Healthcare (Uppsala, Sweden)
Minisart® Filters (0.45 μm)	Sartorius Stedim Biotech (Goettingen, Germany)
Syringe, needles and accessories	BD Biosciences
Eppendorf table-top centrifuge	Eppendorf (Germany)

2.1.3.4 Protein concentration estimation

Amicon Ultra (3, 10 kDa)	Milipore (Co-cork, Ireland)
Vivacon 500 (3, 10 kDa)	Sartorius Stedim Biotech (Göettingen, Germany)
BioSpec-nano micro-volume spectrophotometer	Shimadzu Corporation (Kyoto, Japan)

2.1.4 Other instruments

Biometra T gradient PCR thermocycler	Biometra (Goettingen, Germany)
Sonoplus HD2200 ultrasonicator	Bandelin (Berlin, Germany)
Micropulser electroporator	Bio-Rad (Hercules, CA, USA)
Ultraspec 2100Pro Spectrophotometer	GE Healthcare (Uppsala, Sweden)
Stop flow Spectrometer SX20	Applied Biophysics (UK)

2.1.5 Computer software

PSI-Blast	EMBL-EBI (Cambridgeshire, U.K.)
Jalview	Elixir (U.K.)
Serial Cloner v2.6.1	© Franck Perez (SerialBasics)
PyMOL v1.5	Schrödinger, LLC (Portland, Oregon, USA)

OriginPro 9	OriginLab (Northampton, MA, USA)
NMRPipe and NMRDraw	NIST & NIH (USA)
SPARKY	© Thomas Goddard (San Francisco, USA)

2.2 METHODS

2.2.1 Sequence alignment

Multiple sequence alignments were performed using the interactive sequence alignment software, Jalview [203], which provides the ability to view, edit and analyze protein sequences. Protein sequences were sourced from the Uniprot database [204] and submitted to a web-server where distantly related sequences were then aligned based on the ClustalW [205] and Clustal-Omega [206] algorithms. Subsequently, the multiple sequence alignment results were analyzed in Jalview 2.9 [203]. The similarities within each sequence were then colored according to the percentage of residues in each column that agrees with the consensus sequence.

2.2.2 Cloning of *Mb*AhpC and its mutants

The construct designs of pET9d-*Mb*AhpC, *Mb*AhpC$_{16-195}$ and *Mb*AhpC$_{41-195}$ and all molecular cloning were performed by Mr. Arvind Kumar from Professor G. Grüber's laboratory (SBS, NTU) [196]. The isolated plasmids were then utilized in this study.

To identify the critical residues involved in the redox-oligomerization and activity of *Mb*AhpC, in-fusion-based mutagenesis was performed to generate different mutants. The mutant *Mb*AhpC$_{\Delta 23-34}$ was generated during my previous study and six new mutants were generated for this study. The *Mb*AhpC mutants with amino acid substitutions were created by substituting the single, double and triple conserved residues from *Mb*AhpC. Primers were designed following the schematic drawing, such that both primers have at least 15 base pairs overlap, excluding the mutations and/or deletions introduced (Figure 2.1A).

(A)

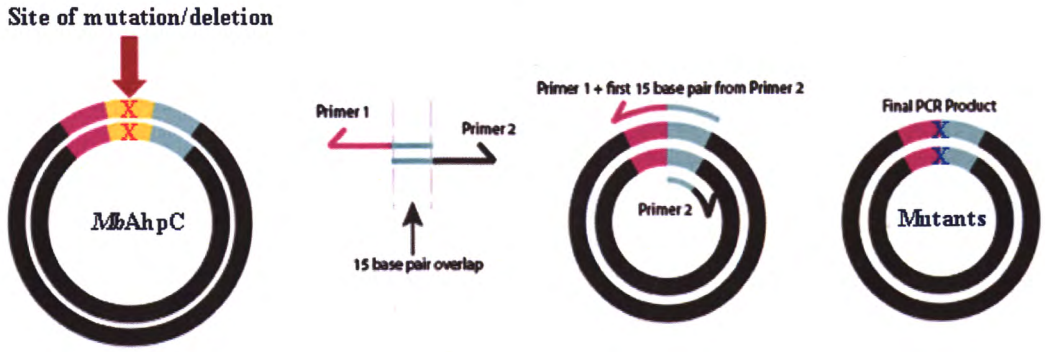

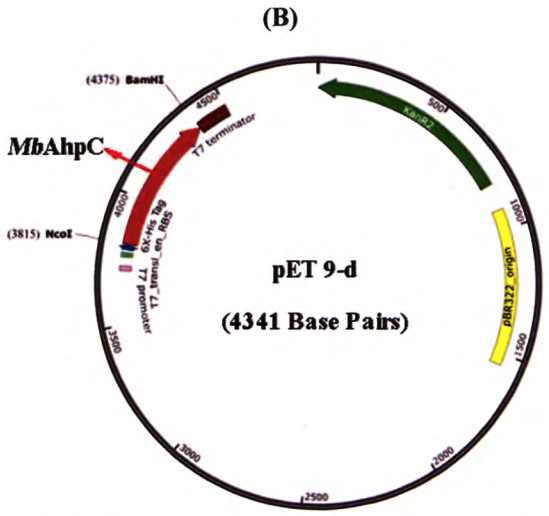

Figure 2.1: *Primers design and plasmid construct of MbAhpC.* **(*A*)** Schematics drawing of primers design. Both forward and reverse primers designed with 15 base pairs overlap, to ensure that the primers would anneal. In addition, the annealing temperatures of both primers were kept below 70 °C. The regions marked in orange are sites of deletion and/or mutations. **(*B*)** Plasmid pET-9d [202] with the two restriction sites labelled; *NcoI* and BamHI. *Mb*AhpC genome was engineered into this plasmid to ensure the production of the recombinant protein; AhpC. For a tight control of gene expression, kanamycin resistance gene was added to the plasmid.

All primers utilized for the amplification of plasmids were ordered from IDT (Integrated DNA Technologies, USA) and the full-length *Mb*AhpC-pET9d plasmid was used as a template in PCR Reactions. The primers encoding the mutations (underlined) are listed as following:

Construct		**Oligonucleotide Sequence (5'-3')**
*Mb*AhpC$_{T5A}$	Primer 1 (Forward)	TGC TAG CTA TTG GCG ATC AAT TCC CCG
	Primer 2 (Reverse)	CCA ATA GCT AGC AGT GGC ATG ACC ATG
*Mb*AhpC$_{T5A/D8A}$	Primer 1 (Forward)	TGC TAG CTA TTG GCG CTC AAT TCC CCG CCT ACC AG
	Primer 2 (Reverse)	ATT GAG CGC CAA TAG CTA GCA GTG GCA TGA CCA TG
*Mb*AhpC$_{T5A/D8A/Y13A}$	Primer 1 (Forward)	CCG CCG CTC AGC TCA CCG CTC TCA T
	Primer 2 (Reverse)	AGC TGA GCG GCG GGG AAT TGA GCG C
*Mb*AhpC$_{D22N/K25Q}$	Primer 1 (Forward)	GGT AAT CTG TCC CAA GTC GAC GCC AAG CAG

	Primer 2 (Reverse)	GAC TTG GGA CAG ATT ACC GCC GAT GAG AGC G
*Mb*AhpC$_{D22N/K25Q/D27N}$	Primer 1 (Forward)	GTC AAT GCC AAG CAG CCC GGC
	Primer 2 (Reverse)	GGC ATT GAC TTG GGA CAG ATT ACC GCC
*Mb*AhpC$_{C176S}$	Primer 1 (Forward)	CGC AAG CAA CTG GCG CAA GG
	Primer 2 (Reverse)	TTG CTT GCG CAC AGC TCG TC

PCR reactions were set up on ice, with each composition reflected in Table 2.1. KAPA HiFi DNA polymerase was added last to the PCR reaction mixtures, and the mixtures were immediately placed into the PCR thermocycler where the lid was preheated to 95°C. The program was set as stated in Table 2.2.

Table 2.1: *Composition of PCR reaction mixture and respective volume and concentration.*

Component	Final concentration	Volume (µl)
Water, nuclease-free	-	35.5
5x HiFi GC buffer	1x	10.0
10 mM dNTP mix	0.2 mM of each	1.0
Forward primer (100 µM)	2 µM	1.0
Reverse primer (100 µM)	2 µM	1.0
Template DNA	50 ng/ul	0.5
*KAPA HiFi DNA polymerase	2.5 U/ul	1.0
Total volume = 50 µl		

Table 2.2: *PCR thermocycler program I.*

No.	Step	Cycles	Temperature	Time
I	Initial Denaturation	1	98 °C	2 minutes
II	Denaturation	30	98 °C	20 seconds
III	Primer annealing	30	Varying temperatures	15 seconds
IV	Primer extension	30	72 °C	3 minutes
V	Final extension	1	72 °C	7 minutes

For optimization, four different primer annealing temperatures were programmed into the PCR thermocycler as stated in the Table 2.3. After amplification,

5 µl of each PCR reaction mixture were used to analyze the presence and purity of the gene products. The samples were analyzed on an 1.5% preparative agarose gel, running at 100 V and the PCR fragment size was confirmed using the standard GeneRuler 1 kb ladder (ThermoScientific). Upon confirming the presence of the gene products, the amplified gene products were then subjected to further downstream treatments.

Table 2.3: *Annealing temperatures for PCR thermocycler program.*

Construct	Tm of Primers (°C)		Annealing temperatures for PCR thermocycler (°C)
*Mb*AhpC$_{T5A}$	Primer 1	62.4	60.0, 63.0, 67.0, 69.0
	Primer 2	61.3	
*Mb*AhpC$_{T5A/D8A}$	Primer 1	68.8	61.2, 63.6, 65.9, 68.1
	Primer 2	66.8	
*Mb*AhpC$_{T5A/D8A/Y13A}$	Primer 1	68.6	63.6, 65.9, 68.1, 69.5
	Primer 2	69.5	
*Mb*AhpC$_{D22N/K25Q}$	Primer 1	65.2	61.2, 63.6, 65.9, 68.1
	Primer 2	65.9	
*Mb*AhpC$_{D22N/K25Q/D27N}$	Primer 1	64.4	54.0, 58.8, 63.6, 65.9
	Primer 2	63.2	
*Mb*AhpC$_{C176S}$	Primer 1	62.8	54.0, 58.8, 63.6, 65.9
	Primer 2	61.3	

To remove methylated template DNA, 10 µl of PCR reaction mixture were incubated with DpnI at 37°C for 1 hr (in a total volume of 50 µl), followed by heat inactivation at 80°C for 20 min. The composition of the reaction is listed in Table 2.4.

Table 2.4: *Composition of DpnI treatment and their respective volumes.*

Component	Volume (µl)
Water, nuclease-free	33.0
10x CutSmart buffer	5.0
0.2 mM DpnI (NEB)	2.0
PCR product	10.0
Total volume = 50 µl	

Desalting and concentration of the DpnI treated products were performed thereafter by DNA butanol precipitation. DpnI treated samples were topped up to 100 µl with filtered distilled water. 1 ml of 100% butanol was then added to the mixture to

precipitate the DNA within. After thorough mixing, DNA was pelleted down at 13,000 rpm for 5 min in a table-top microcentrifuge (Eppendorf, Germany). The supernatant was then decanted and the pellet was re-suspended in 200 µl of 70% ethanol to remove excess butanol. The solution was centrifuged again at 13,0000 rpm for 5 min and the supernatant was decanted once again. Subsequently, the DNA pellet was left to air dry in a biosafety cabinet for 5 minutes to remove any remaining ethanol. Next, the DNA was re-dissolved with 7 µl of sterile water.

The precipitated DNA was transformed into electro-competent *E. coli* DH5α cell strain, using a Micropulser Electroporator (Bio-Rad, USA) at 2.5 kV. 1 ml LB media was then added to collect all electroporated cells and recovery was performed at 37°C, 180 rpm for 1 hour before plating on Luria-Bertani (LB) agar plates supplemented with 30 µg/ml kanamycin. The agar plates were then incubated at 37°C overnight.

Ten colonies from the agar plates were incubated into LB media supplemented with 30 µg/ml kanamycin, followed by incubation at 37°C overnight. 4 ml of cell suspensions were centrifuged and the cells were subjected to plasmid isolation following the standard protocol provided by QIAGEN Mini-Prep Kit (QIAGEN, Germany). The sequences of the mutated sites were confirmed by DNA Sequencing (1st Base Asia, Singapore).

2.2.3 Cloning of *Mb*TrxC and *Mb*TrxB2

The construct *Mb*TrxC was designed and generated by Dr. Priya Ragunathan from Professor G. Grüber's laboratory (SBS, NTU) [196]. The isolated plasmid was then utilized in this study.

*Mb*TrxB2 was amplified via PCR using primers incorporated with *NcoI* and BamHI restriction sites (underlined) in the forward and reverse primers, respectively (Table 2.5). *M. bovis* (BCG strain) genomic DNA was used as the template and PCR reaction mixture was prepared following Table 2.1.

Table 2.5: *Oligonucleotide sequences of MbTrxC and MbTrxB2.*

Construct		Oligonucleotide sequence (5'-3')
*Mb*TrxC	Forward	GCA CAA CGC CAT GGC AAT GAC CGA TTC CGA GAA GT
	Reverse	CCG GGA TCC CTA GTT GAG GTT GGG AAC CAC GTC T
*Mb*TrxB2	Forward	TTA ACC ATG GAT ATG ACC GCC CCG CCT GTC
	Reverse	TTA TGG ATC CTC ATC GTT GTG CTC CTA TCA ATG CGT CGG

KAPA HiFi DNA polymerase was added last to the reaction mixture and the reaction mixtures were immediately placed into the PCR thermocycler where the lid was preheated to 95°C. The program was set as stated in Table 2.6.

Table 2.6: *PCR thermocycler program II.*

No.	Step	Cycles	Temperature	Time
I	Initial Denaturation	1	98 °C	2 minutes
II	Denaturation	30	98 °C	20 seconds
III	Primer annealing	30	60 °C	15 seconds
IV	Primer extension	30	72 °C	3 minutes
V	Final extension	1	72 °C	7 minutes

After the PCR program was completed, the presence and purity of gene products were analyzed via an 1.5% agarose gel. If the desired gene size was observed on the gel, gel extraction was performed. The PCR fragment corresponding to the appropriate size was cut-out and DNA was extracted using the QIAquick Gel Extraction Kit (QIAGEN) following the manufacturer's protocol.

The eluted PCR product was then double digested with restriction enzymes, Fast Digest *NcoI* and BamHI for 1 hour in a 37°C water bath (Table 2.7). Following which, the double-digested gene fragments were purified using a QIAquick PCR Purification Kit (QIAGEN) as per manufacturer's protocol.

Table 2.7: *Double digestion components and their respective volume.*

Component	Volume (µl)
PCR Product [DNA] = 154.72 ng/µl	43.0
Fast Digest *NcoI* (ThermoScientific)	1.0
Fast Digest BamHI (ThermoScientific)	1.0
10x Fast Digest buffer (ThermoScientific)	5.0
Total volume = 50 µl	

The purified PCR product was then ligated to *NcoI*/BamHI digested pET9-d1-His6 [202] plasmid using a 3:1 and 1:1 insert-to-vector ratio (Table 2.8). pET9-d1-His_6 [202] plasmid was used for cloning as it contains a histidine tag, making it suitable for affinity purification. Next, ligation was performed at room temperature for 1 hour.

Table 2.8: *Components of ligation mixture.*

Component	Amount
Vector (pET9d-d1-His6)	50 ng
Insert	1- 3 times of vector
T4 DNA Ligase (Promega)	1 µl
10x Ligase Buffer (Promega)	1 µl
Filtered water	Top up to 10 µl

Subsequently, the reaction was topped up to 100 µl of water and DNA butanol precipitation was performed following the protocol mentioned above. The precipitated DNA was transformed into 80 µl of *E. coli* DH5α cells by electroporation. The plasmids were then isolated from the transformants and double-digested and applied onto an 1.5% agarose gel to select the plasmid containing the right insert size. The sequences of the selected plasmids were confirmed by DNA sequencing (1st Base Asia, Singapore).

2.2.4 Electroporation transformation into *E. coli* BL21 (DE3) expression strain

Recombinant plasmids from all *Mb*AhpC mutants and *Mb*TrxB2 were introduced into electro-competent *E. coli* BL21 (DE3) expression cell strain which were prepared according to the protocol from Seidman *et al.* (2001) [207]. The recombinant plasmid from *Mb*TrxC was introduced into electro-competent *E. coli* Rosetta™ (DE3) expression cell strain (Novagen, Singapore). Transformation was performed using 80 µl of electro-competent cells and 1 – 50 ng of plasmid at a constant voltage of 2.5 kV using Micropulser Electroporator (Bio-rad, USA). Afterwards, 920 µl of LB media were added into the electroporation cuvette to collect all electroporated cells. The cells were then recovered by shaking at 37°C, 180 rpm for 1 hour before plating on LB agar plates supplemented with kanamycin. The cells carrying the construct *Mb*TrxC were plated on LB agar plates supplemented with kanamycin and chloroamphenicol.

2.2.5 Assays to analyze the yield and solubility of recombinant proteins

2.2.5.1 Induction test

Five single colonies of *E. coli* cells carrying the genes that encodes *Mb*AhpC and *Mb*TrxB2 recombinant proteins were randomly chosen from the agar plates, and cultured in 6 ml LB media supplemented with 30 µg/ml kanamycin. For *Mb*TrxC recombinant proteins, the single colonies were cultured in LB media supplemented with 30 µg/ml kanamycin and 34 µg/ml chloramphenicol. Subsequently, cells were cultured

at 37°C, with the shaking speed of 180 rpm until it reached an attenuance of optical density at 600 nm (OD_{600}) = 0.6. Cells were then divided into two equal halves, with only one aliquot induced with 1 mM isopropyl-β-D-thiogalactoside (IPTG). Both set of aliquots were incubated at 37°C, with the shaking speed of 180 rpm for an additional 2 hours. After incubation, 1 ml of cell suspension with an OD_{600} = 1.0 was taken out and pelleted down with a table-top centrifuge at 13,000 rpm for 5 min. The supernatant was then decanted and the pellet was re-suspended in 500 µl Milli-Q water, followed by centrifugation at 13,000 rpm for 5 min again. Thereafter, the supernatant was discarded and pellet was re-suspended in a mixture consisting of 30 µl of Milli-Q water, after which it was lysed with 30 µl of 2x lysis buffer in the presence of 12.5 mM dithiothreitol (DTT). The 1x lysis buffer is composed of 62.5 mM Tris/HCl, pH 6.8, 2.3% sodium-dodecyl sulfate (SDS), 10% glycerol and 0.05% bromophenolblue. Thereafter, the mixture was heated at 95°C for 10 min. Analysis of the induction assay was performed with 15 µl of the sample loaded onto a 17% SDS polyacrylamide gel, running at a constant current of 20 mA.

Following gel electrophoresis, the SDS polyacrylamide gel was stained with Coomassie staining solution (0.2% w/v Coomassie brilliant blue, 40% v/v methanol, 1% v/v acetic acid) for 10 min. After staining, the gel was de-stained first with de-staining solution 1 (25% v/v isopropanol, 10% v/v acetic acid) then, de-staining solution 2 (7.5% v/v methanol, 10% acetic acid).

2.2.5.2 Solubility assay for recombinant proteins

Table 2.9: *Buffers used to analyze the solubility of recombinant proteins.*

	Buffers	pH
A	50 mM Tris/HCl, 200 mM NaCl	7.5
B	50 mM Tris/HCl, 200 mM NaCl	8.5
C	50 mM Tris/HCl, 500 mM NaCl	8.5
D	25 mM HEPES, 200 mM NaCl	7.5
E	20 mM Na-Phosphate, 150 mM NaCl	6.5

Following the successful induction of the recombinant proteins, cells were cultured at 37°C, with shaking of 180 rpm until it reached an attenuance of OD_{600} = 0.6 before induction at 20°C overnight. Thereafter, the solubility of the recombinant proteins was tested in various buffers (Table 2.9). Next, 3 ml cell suspension was

harvested at 10,000 rpm for 7 min at 4°C using Sorvall Legend Micro 17R Microcentrifuge (Thermo Scientific, USA). The supernatant was discarded and the pellet was re-suspended in 1 ml of the tested buffer. Re-suspended cells were sonicated 3 times, each lasting a minute with 2 min cooling interval per cycle, using the sonicator tip MS72 at 10% power (Bandelin, Sonopuls, Germany). After sonication, the supernatant was then separated from the cell pellet by centrifugation at 10,000 x g for 7 min at 4°C. Subsequently, the supernatant was transferred to a fresh tube while the pellet was re-suspended in equal volume of the respective tested buffer. All the steps were performed on ice. For analysis of the solubility of the recombinant proteins, 15 µl of sample from each supernatant and pellet were loaded onto a 17% SDS gel. Proteins that are soluble in the corresponding buffer would be found in the supernatant while the insoluble proteins would remain in the pellet.

2.2.6 Production of recombinant proteins from *M. bovis*

2.2.6.1 Large scale production of recombinant *Mb*AhpC and its mutant proteins

To ensure higher protein yield, fresh transformation with recombinant plasmids of *Mb*AhpC and its mutants into *E. coli* BL21 (DE3) cells were performed following the protocol as mentioned in Section 2.2.4. Instead of plating the cells on a LB agar plate, 10 µl of cells after recovery stage was added into 100 ml of LB media supplemented with 30 µg/ml kanamycin to prepare the starter cultures for upscaling the next day. To express the *Mb*AhpC recombinant proteins, cells were shaken in 1-liter LB media containing 30 µg/ml kanamycin for about 4 hours at 37°C until an OD_{600} = 0.6 - 0.7 was reached. Subsequently, cells were induced with IPTG to a final concentration of 1 mM overnight at 18°C. Following incubation, cells were then harvested at 6,500 rpm for 12 minutes at 4°C.

2.2.6.2 Large scale production of recombinant *Mb*TrxC and *Mb*TrxB2 proteins

Recombinant *Mb*TrxC was produced from cells grown in 1-liter LB media supplemented with 30 µg/ml kanamycin and 34 µg/ml chloramphenicol, whereas recombinant *Mb*TrxB2 was produced from cells grown in 1-liter LB media supplemented with 30 µg/ml kanamycin. Subsequent steps involved in protein production followed the protocol mentioned in Section 2.2.6.1.

2.2.7 Protein purification of recombinant proteins

To ensure high purity of proteins, all recombinant proteins were purified using a two-step purification protocol. As all the AhpC mutants and Trx recombinant proteins were attached with a His_6-tag, Ni^{2+}-NTA affinity chromatography was utilized to separate these recombinant proteins from *E. coli* proteins. Affinity chromatography is based on the concept of immobilized-metal affinity chromatography wherein nickel ions (Ni^{2+}) are immobilized to the agarose beads through nitrilotriacetic acid (NTA). His_6-tag engineered in the recombinant proteins would allow the binding of histidine to Ni^{2+}-ions [208].

Thereafter, the cell lysate was incubated with the affinity matrix resin at 4°C. Batch procedure in which gradient imidazole concentration was then utilized to elute the His_6-tag engineered recombinant proteins. In this case, imidazole competes with histidine to bind to Ni^{2+}, thereby leading to the elution of the His_6-tag engineered recombinant proteins.

Next, the purity of these recombinant proteins was further polished using Size Exclusion Chromatography (SEC). Herein, proteins were separated based on their molecular sizes. In this step, the oligomeric forms of proteins can be determined, and the desired oligomeric states can be selected for downstream experiments.

Purification process of wt AhpC and its mutants encompasses the purification of both the oxidized and reduced form of the recombinant proteins. The former does not utilize DTT in all protein purification steps while the latter includes 0.8 mM to 2 mM DTT in the purification buffers. However, the purification process for *Mb*TrxB2 and -TrxC were performed without DTT. The purity of the recombinant proteins was verified using a 17% SDS-gel. The concentrations of all recombinant proteins were determined by a spectrophotometer (BioSpec-Nano, Shimadzu) at an absorbance of 280 nm using the necessary extinction coefficient of each recombinant protein (AhpC; 25105 M^{-1} cm^{-1}, TrxC; 11125 M^{-1} cm^{-1} and TrxB2; 14565 M^{-1} cm^{-1}).

2.2.7.1 Protein purification of wt *Mb*AhpC and its mutant forms in oxidized conditions

After harvesting the cells, cells were re-suspended in buffer A (50 mM Tris/HCl, pH 7.5, 200 mM NaCl) with the addition of 2 mM Pefabloc^{SC} (Biomol, Germany) protease inhibitor. Subsequently, cells were lysed on ice by sonication, using the sonicator tip KE76 at 30% power (3 times for 1 min, with 2 min cooling intervals) in

buffer A. The cell debris were separated from the supernatant by centrifugation with an Eppendorf 5810R Centrifuge (Eppendorf, Germany) at 12,500 x g for 25 min at 4°C (Eppendorf, Germany).

Hereafter, the supernatant was filtered (0.45 μm) and the binding of proteins with Ni^{2+}-NTA agarose was achieved using batch treatment. After incubation with Ni^{2+}-NTA agarose for 60 min at 4°C on a sample rotator (Neolab), the bound proteins were eluted from the Ni^{2+}-NTA agarose beads with an imidazole gradient from 20 mM to 600 mM in buffer A. To remove any free nickel ions that may elute out with the proteins, 10 mM ethylenediaminetetraacetic acid (EDTA) was added into the elution vial.

12 μl of protein sample was then applied to a 17% SDS-gel to identify fractions containing the recombinant proteins. Whenever required, the eluted proteins were pooled and concentrated using Centricon spin concentrators (10 kDa molecular mass cut off; Millipore, Ireland). Following which, samples were applied to an SEC column (Superdex 200 Increase 10/300 GL; GE Healthcare, Sweden), equilibrated with buffer A.

2.2.7.2 Protein purification of wt *Mb*AhpC and its mutant forms in reduced conditions

The purification protocol is similar to that used for the oxidized condition, except that the cells were lysed in buffer A with addition of 0.8 mM DTT, and imidazole-gradient elution was performed in buffer A with the addition of 0.8 mM DTT. Fractions containing the recombinant proteins would then be applied to the SEC column as aforementioned. However, the SEC column was equilibrated in buffer A with the addition of 2 mM DTT.

2.2.7.3 Protein purification of *Mb*TrxB2 and *Mb*TrxC

As *Mb*TrxB2 and *Mb*TrxC do not form oligomers in different redox conditions, the purification protocol is identical to the protocol mentioned in Section 2.2.7.1. However, the recombinant proteins were concentrated using Centricon spin concentrators (3 kDa cut-off) and passed through Superdex 75 10/300 GL column (GE Healthcare, Sweden) instead.

2.2.8 Dynamic Light Scattering (DLS)

DLS data measurements were performed with the Malvern Zetasizer Nano ZS spectrophotometer (Malvern, UK) and a low-volume quartz batch cuvette (ZEN2112). 15 µl of purified recombinant proteins (1 mg/ml) was used for each measurement and data collection was performed at 25°C. After 60 s equilibration time, the backscattering at 173° was detected for all recombinant proteins. Analysis of the scattering intensities was performed using the in-built Zetasizer software v7.01 to calculate the hydrodynamic diameter (D_H), size and volume distribution.

2.2.9 NADPH-dependent peroxidase activity and data analysis

Based on the catalytic cycle of the *Mb*AhpC system in *Mycobacteria*, the decrease in absorbance of NADPH due to transfer of electrons between TrxC and AhpC is proportional to the activity of *Mb*AhpC. This decrease in absorbance can be monitored at 340 nm. Initially, the assay was carried out at 25°C with the components and their concentrations listed in Table 2.10.

Table 2.10: *NADPH-dependent peroxidase reaction components*

Syringe 1	**Concentration**
Hepes, pH 7.0	50 mM
Ammonium sulfate	100 mM
EDTA	1 mM
NADPH	0.1 mM
*Ec*TrxR	0.5 µM
*Ec*Trx	4 µM
MbAhpC or its mutants	6 µM

Syringe 2	**Concentration**
H_2O_2	50 µM

Each syringe contained the components listed in Table 2.10 and the stopflow spectrometer would pump 60 µl of sample from each syringe into the drive cell holder. The reaction was prepared on the spot, with the addition of NADPH last to initiate the start of the reaction. This protocol followed Parsonage *et al.* (2005) [209] whereby the absorbance at 340 nm was monitored for 120 s using a stopped flow spectrometer, SX20 (Applied Photophysics, UK). Triplicates were taken for each measurement. The rate of

NADPH oxidation was calculated by a least square fit to the linear portion of the curve (ε_{NADPH} = 6200 M^{-1} cm^{-1}). NADPH consumption measured in the absence of *Mb*AhpC was taken as a control. The background rate was subtracted from the experimental rate to yield the activity due to *Mb*AhpC. All rates reported here are the average of three measurements and different protein batches.

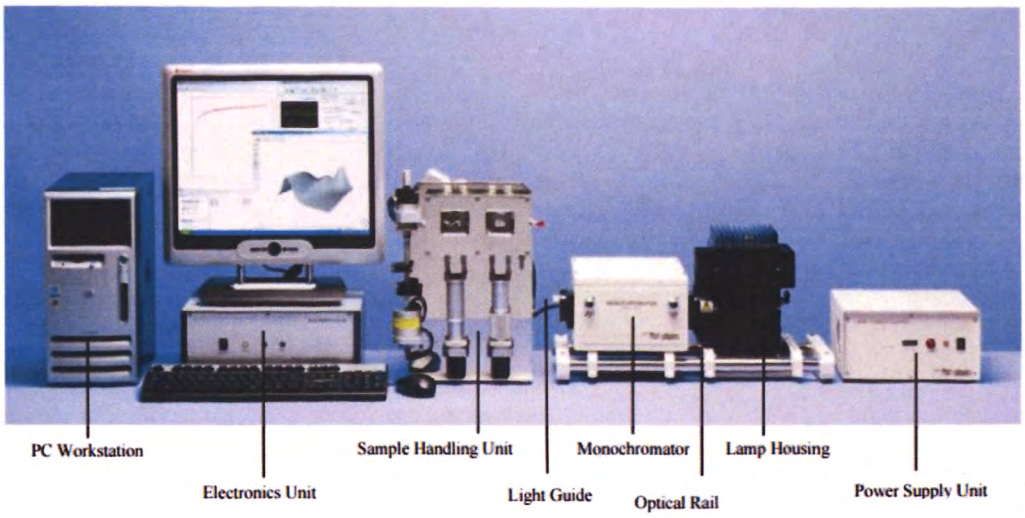

Figure 2.2: Picture of SX20 Stop-flow spectrometer by Applied Photophysics, UK.

However, to accurately measure the activity of *Mb*AhpC, a consortium of *M. bovis* thioredoxin (TrxB2 and TrxC) recombinant proteins were used instead of *Ec*TrxR and *Ec*Trx for this study. In the latter experiments, all components and concentrations listed in Table 2.10 remained constant.

To obtain the Michaelis-Menten plot, peroxidase activity was measured similarly however, with varying concentrations of H_2O_2. *Mb*AhpC was measured using a range of 250 nm to 50 µM of H_2O_2 while *Mb*AhpC$_{T5A/D8A}$ and *Mb*AhpC$_{C176S}$ peroxidase activity was measured from 250 nm to 30 µM of H_2O_2. At least 10 concentrations were used for fitting into the Michaelis-Menten plot using Origin Pro 9 (OriginLab, USA). The Michaelis constant (K_m) was then obtained from these plots. The kinetic parameters such as the turnover number (k_{cat}) and catalytic efficiency (k_{cat}/K_m) were also calculated to give a more holistic understanding of the mutants' activity. The percentage of catalytic efficiency of each mutant were measured with an assumption that *Mb*AhpC has 100% of activity.

2.2.10 Peroxide reduction assay using SDS-PAGE

The peroxide reduction assay is performed based on prior observations that the reduced and oxidized forms of 2-Cys-Peroxiredoxins runs differently on a non-reducing SDS-PAGE gel [210]. Prior to each experiment, recombinant AhpC were purified following Section 2.2.7.2, except that proteins were reduced with 20 mM DTT. This was performed to ensure that all proteins are fully reduced before performing subsequent oxidation with H_2O_2. Subsequently, buffer exchange was performed with a PD-10 desalting column (GE Healthcare, Sweden) in 50 mM Phosphate, pH 7.4 buffer supplemented with 1 mM diethylenetriaminepentaacetic acid and 1 mg/ml catalase. 30 µM of recombinant AhpC were then incubated with varying concentrations of H_2O_2 (0.5 µM to 10 µM) for 5 min before inhibiting the reaction with 50 mM-ethyl maleimide (NEM). 15 µl of sample was then aliquoted and suspended in a 1x sample buffer without DTT and ran on a 17% SDS gel. The gel was then treated as mentioned in Section 2.2.5.1.

2.2.11 Nuclear Magnetic Resonance (NMR) spectroscopy

NMR spectroscopy is a dynamic technique used to study the structural and functional aspects of macromolecules such as proteins. In this study, NMR is utilized to study the biochemical and biophysical properties of *Mb*TrxC. Through titration assays, protein-protein interactions can be demonstrated and new binding partners, be identified. NMR also allows the mapping of these interacting regions down to a single amino acid level. Since hydrogen is one of the most receptive and abundant NMR active nuclei besides other isotopes such as ^{15}N, ^{13}C, ^{31}P etc., it can be observed in magnetic resonance. Any nuclei having mass number, which exhibits net intrinsic magnetic momentum and angular momentum, can be defined as NMR active. All NMR experiments performed were collected on a Bruker Avance 700 MHz machine located in the SBS NMR-core facility with the help of Dr. Shin Joon from Professor G. Grüber's laboratory (SBS, NTU) [196].

2.2.11.1 ^{15}N single labeling of proteins

For NMR experiments, single labelled (^{15}N) recombinant proteins were produced in *E. coli* BL21 (DE3) cells and grown in M9 minimal media to ensure that the amino acids were labelled in the expressed proteins. The reagents used for M9 minimal media are listed in Table 2.11.

Table 2.11: *M9 minimal media components and their concentration.*

Component	Concentration
Na_2HPO	42 mM
KH_2PO_4	22 mM
NaCl	8.5 mM
$^{15}NH_4Cl$	1 g/l
$CaCl_2$	0.1 mM
$MgSO_4$	2 mM
D-Glucose	10 g/l
Trace Elements (1 mM Cu^{2+}, Zn^{2+}, Mn^{2+}, Co^{2+}, Ni^{2+}, MoO^{4-})	1 ml
$FeCl_3$	30 uM
Thiamine	5 ng/l
Kanamycin	30 ug/ml
Chloramphenicol	34 ug/ml

Cell cultures were prepared in 30 ml LB media serving as overnight culture and subsequently, pelleted down at 6,000 rpm, for 10 min at 25°C and washed with minimal media prior to transferring to a large volume of M9 media with OD_{600} of 0.1. The culture was then incubated at 37°C with shaking of 180,000 rpm till an OD_{600} of 0.6-0.8 (10 hours) and subsequently induced with 1 mM IPTG overnight at 18 °C. After which, cells were harvested and stored at -80°C.

To obtain a pure and homogenous protein, the identical purification protocol mentioned in Section 2.2.7.3 was performed. However, the buffer used in Ni^{2+}-NTA and SEC was 20 mM Sodium Phosphate, pH 6.5, 100 mM NaCl. For NMR measurements, 2 mM DTT was added to the purified ^{15}N-*Mb*TrxC obtained from SEC. Preparation of NMR samples included the use of 10% D_2O and 0.001% sodium azide (NaN_3).

2.2.11.2 NMR Titration experiments of *Mb*TrxC with *Mb*AhpC, -AhpC$_{T5A/D8A}$ or -AhpC$_{D22N/K25Q/D27N}$

NMR titration experiments were performed on a Bruker Avance 700 MHz Spectrometer (Bruker, Billerica, MA), equipped with a 5 mm z-axis-gradient cryogenic probe at 24.85°C. Prior to data collection, the pulse was calibrated, and baseline corrections were applied wherever necessary. The proton chemical shift was referenced to 0 ppm using the methyl signal of 2, 2-dimethyl-2-silapentane-5-sulphonate (DSS) (Cambridge Isotope Laboratories) as an external reference.

To study the interaction between *Mb*TrxC and AhpC, 0.1 mM of ^{15}N-labelled *Mb*TrxC proteins were titrated stepwise with unlabeled *Mb*AhpC or -AhpC$_{T5A/D8A}$ or -AhpC$_{D22N/K25Q/D27N}$ proteins in molar ratios of 1:0 (*Mb*TrxC:AhpC), 1:0.5, 1:1 and 1:2. Under the supervision of Dr. Shin Joon, ^{1}H-^{15}N HSQC (Hetero nuclear Single Quantum Coherence) spectra were recorded with 2048 complex data points in t_2 and 240 t_1 increments. Spectral widths of 2270 and 11160 Hz were employed respectively in F1 (^{15}N) and F2 (^{1}H). All data were processed with NMRPipe and NMRDraw [211], and subsequently analyzed using SPARKY [212]. The resonance assignments of ^{15}N and NH resonances were achieved based on the previously reported NMR chemical shift data of *Mb*TrxC from BioMagnetic Resonance Bank (BMRB, accession code: 17242 [213]). To identify residues involved in the interaction between TrxC and AhpC, the reported reduced form of *Mt*TrxC (PDB ID: 2L4Q [213]) was used and residues were visualized using PyMOL [214]. Measurements of the differences in chemical shifts due to the interaction between *Mb*TrxC and *Mb*AhpC or -AhpC$_{T5A/D8A}$ or-AhpC$_{D22N/K25Q/D27N}$ was calculated using the formula $\Delta\delta = [(^{1}H_{free} - {}^{1}H_{bound})^2 + (^{15}N_{free} - {}^{15}N_{bound})_2)]^{½}$.

2.2.12 2D Image analysis of *Mb*AhpC and its mutants

Prior to 2D image analysis, electron micrographs of *Mb*AhpC and *Mb*AhpC$_{\Delta 23-34}$ were recorded and reported in my previous study and published thereafter in *Scientific Reports* [195, 196]. To (i) identify the number of monomers present in the particles, and (ii) confirm the crystal structure of AhpC reported [193] with data collected in solution, a 2D image analysis was performed. The data analysis was kindly performed by Asst Prof. Sashi Bhushan and Ms. Zhan Yin from NTU Institute of Structural Biology (SBS, NTU) [196]. To identify the number of monomers present, the reduced form of *Mb*AhpC was used and a total of 4054 particles were selected for 2D projection analysis. Only particles with clear visibility of single molecules and are separated from neighboring particles were selected. Particles were picked using EMAN2 [215] and processed with RELION 1.4 [216].

2.2.13 *In silico* High Ambiguity Driven DOCKing (HADDOCK) modelling

Experimentally identified binding interfacial residues of *Mb*TrxC were used to perform docking studies to model the complex formation of *Mb*TrxC with *Mt*AhpC$_{C176S}$ using the HADDOCK webserver [217]. The data analysis was performed with guidance

from Dr. Malathy Sony Subramanian Manimekalai from Professor G. Grüber's laboratory (SBS, NTU) [196]. The coordinates for *Mb*TrxC (PDB ID: 2L4Q [213]) and AhpC (PDB ID: 2BMX [193]) were obtained from the Protein Data Bank. Surface-exposed residues experiencing significant chemical shift perturbation (CSP) and intensity loss above 1 δ) during titration were used as restrains. Since HADDOCK requires a set of ambigous interaction restraints to be specified, residues interacting directly at the interace was specified as "active" residues while neighbouring residues, as "passive". In the case of TrxC, the directly interacting residues obtained experimentally were specified as "active" and neighbouring residues, as "passive". In the case of AhpC, the "active" region consists of the well-known redox center consisting of the catalytic cysteines whilst the "passive" residues is composed of the surrounding region. The submitted residues were then placed with an approximate distance of 25 Å and a complex was formed through rigid body energy minimization, which resulted in an initial 1000 structures. Models with the top 200 lowest energy from the above minimization were then subjected to a simulated annealing with a torsion angle space procedure and subsequent flexible refinement in explicit solvents. Models which fulfilled the interface root mean square deviation (RMSD) cutoff of 5 Å were clustered into seven groups. The best model in the highest scoring cluster was selected for analysis and visualization was performed through the PyMOL software package.

2.2.14 Crystallization of wt *Mb*AhpC and *Mb*AhpC$_{C176S}$

Recombinant *Mb*AhpC and *Mb*AhpC$_{C176S}$ proteins were purified using a similar purification protocol mentioned in Section 2.2.7.3. However, the buffer used during SEC was 20 mM Tris/HCl, pH 7.5. To perform crystallization, the recombinant proteins were then pooled and concentrated to 16 mg/ml. The initial screening of crystallization conditions was performed using an in-house made precipitant solution (0.1 M Sodium Citrate, pH 6.0, 16% Ammonium Sulfate). Hanging drop vapor diffusion strategy was utilized in setting up the initial screening. Hanging drops were set up by mixing 1 µl of purified recombinant protein with 1 µl of precipitant solutions, and incubated at 18°C.

Single-wavelengths datasets of *Mb*AhpC$_{C176S}$ crystals were collected remotely by Dr. Asha M. Balakrishna and Ms. Bharti Singal, both from Professor Gerhard Grüber's laboratory (SBS, NTU), at 140 K on beamline 13B1 at the National Synchrotron Radiation Research Center (NSRRC, Hsinchu, Taiwan) using ADSC Quantum 315 CCD detector. Staff at beamline 13B1 (NSRRC) kindly provided technical assistance.

Thereafter, the data was analyzed with the help of Dr. Malathy Sony Subramanian Manimekalai from Professor G. Grüber's laboratory (SBS, NTU).

3. Results

Results

3.1 Sequence analysis of *Mb*AhpC

3.1.1 Sequence analysis of *Mb*AhpC with other bacteria species

The protein sequences of full-length AhpC from different mycobacteria and other infectious bacteria (Table 3.1) were retrieved from Uniprot database and analyzed using Jalview [203]. For analysis, multiple sequence alignments were performed using two main algorithms provided by Clustal-Omega and ClustalW with the retrieved protein sequences as the input. It was observed that the sequence alignment provided by both Clustal-Omega and ClustalW showed crucial differences in AhpC from mycobacteria (Figure 3.1 and 3.2).

Table 3.1: *Accession ID and entry name of bacteria species obtained from Uniprot.*

Bacteria species	Uniprot Accession ID / Entry name
M. tuberculosis	P9WQB7 / AHPC_MYCTU
M. bovis	Q79CV0 / Q79CV0_MYCBI
M. ulcerans	A0PS67 / A0PS67_MYCUA
M. africanum	F8M203 / F8M203_MYCA0
M. smegmatis	A0R1V9 / AHPC_MYCS2
M. sinense	F5Z3R3 / F5Z3R3_MYCSD
M. leprae	Q9CBF5 / Q9CBF5_MYCLE
Bacillus subtilis	P80239 / AHPC_BACSU
Enterococcus faecalis	D4EHS4 / D4EHS4_ENTFL
E. coli	P0AE08 / AHPC_ECOLI
Klebsiella pneumoniae	A0A0V9SPI3 / A0A0V9SPI3_KLEPN
S. typhimurium	P0A251 / AHPC_SALTY
Shigella flexneri	P0AE11 / AHPC_SHIFL
Staphylococcus aureus	P0A0B7 / AHPC_STAA8

In Figure 3.1, the sequence alignment from Clustal-Omega revealed a region of highly conserved amino acids (Residues 1 to 40) in mycobacteria. Interestingly, this is not present in other species of bacteria. Mutational studies were performed with the *M. bovis* (BCG Strain) instead of *M. tuberculosis*, since both strains have 100% identical amino acid sequence. A deletion mutant, *Mb*AhpC$_{41\text{-}195}$, was generated to understand the importance of the highly conserved N-terminal region. In addition, it was observed that the additional residues were specifically located at the far front of the N-terminus (Figure 3.1, red dashed box). In my previous study, a mutant with the first 15 amino acids deleted, was generated and characterized [195, 196]. This study illustrated that

*Mb*AhpC$_{15-195}$ was less soluble and unable to form defined oligomers. In the current study, the focus is on the mutant, *Mb*AhpC$_{41-195}$, which is further elaborated in the following sections.

Interestingly, it was observed that the changes in algorithm between Clustal-Omega and ClustalW revealed differences in the sequence alignment. Clustal-Omega incorporates a position-specific scoring scheme that allows down weighting in the represented sequence groups in part to increase its functionality and sensitivity [218]. Despite this, Clustal-Omega was also derived from ClustalW. In the results obtained from the sequence alignment performed with ClustalW (Figure 3.2), it was observed that the highly conserved region of mycobacteria was found in the amino acids 23-34 instead of the far-left N-terminus. In comparison with crystallographic structures obtained from these species, the highly conserved regions in mycobacteria noticeably forms an additional loop in between the N-terminus instead of the far-front region of the N-terminus (Figure 3.3). Based on the sequence alignment by ClustalW and the structural alignment, the mutant *Mb*AhpC$_{\Delta 23-34}$ was generated in my previous study. Characterization of the recombinant mutant protein via SEC, DLS and EM was performed as well [195, 196]. In the current study, point mutations were performed in this region to understand the significance of these additional residues. This is further elaborated in the following sections.

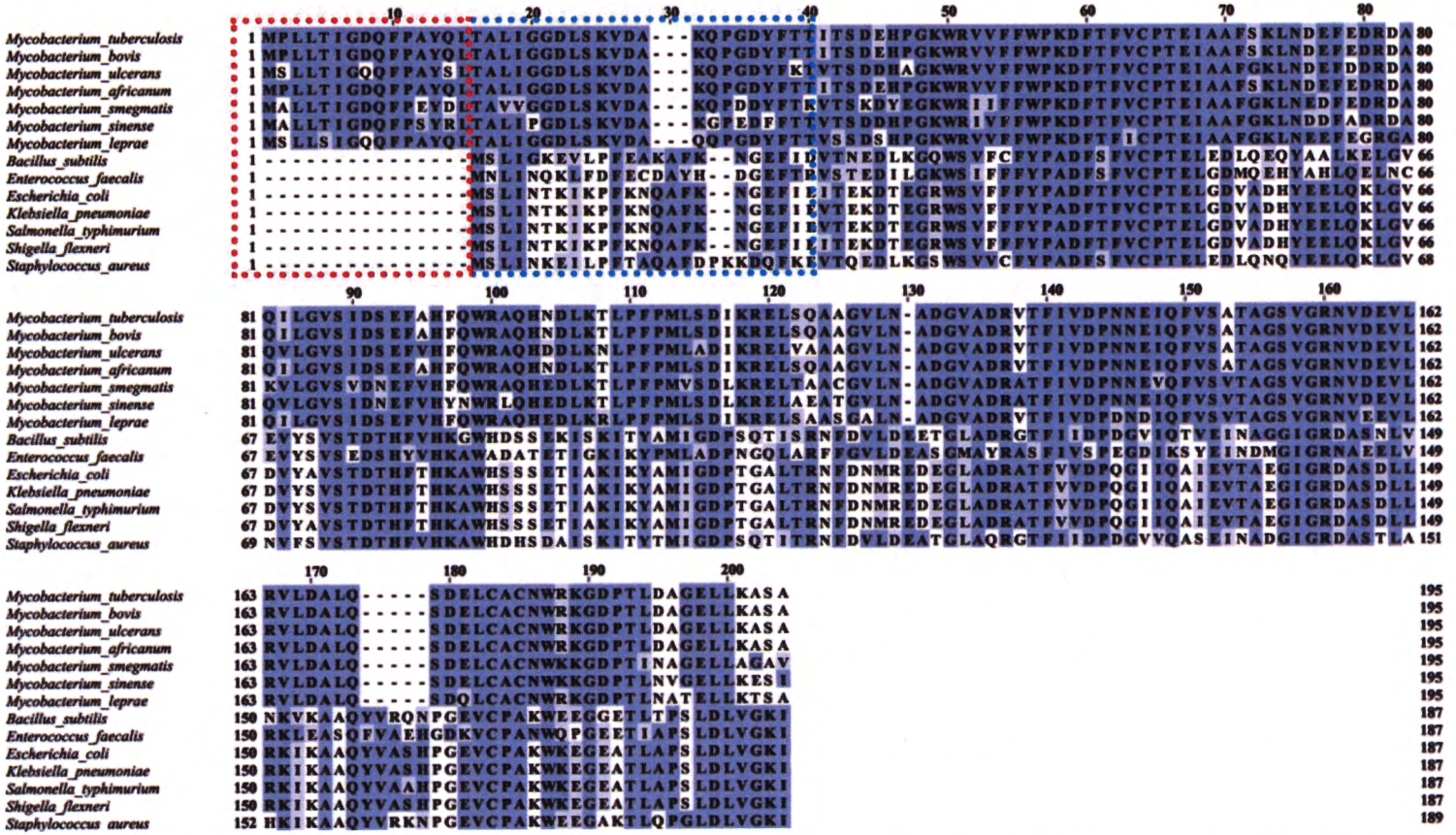

Figure 3.1: *Multiple sequence alignment from Clustal-Omega.* Results from Clustal-Omega revealed residues in the N-terminus of mycobacteria AhpC. that are absent in other species. The analysis also revealed the absence of a conserved region across all species from residues 1 to 40 (*blue dashed box*). Specifically, the presence of the first 15 amino acids (*red dashed box*) that is highly conserved in mycobacteria but absent in other infectious bacteria. To understand the differences between these species, mutants were generated to highlight the significance of the N-terminus extension.

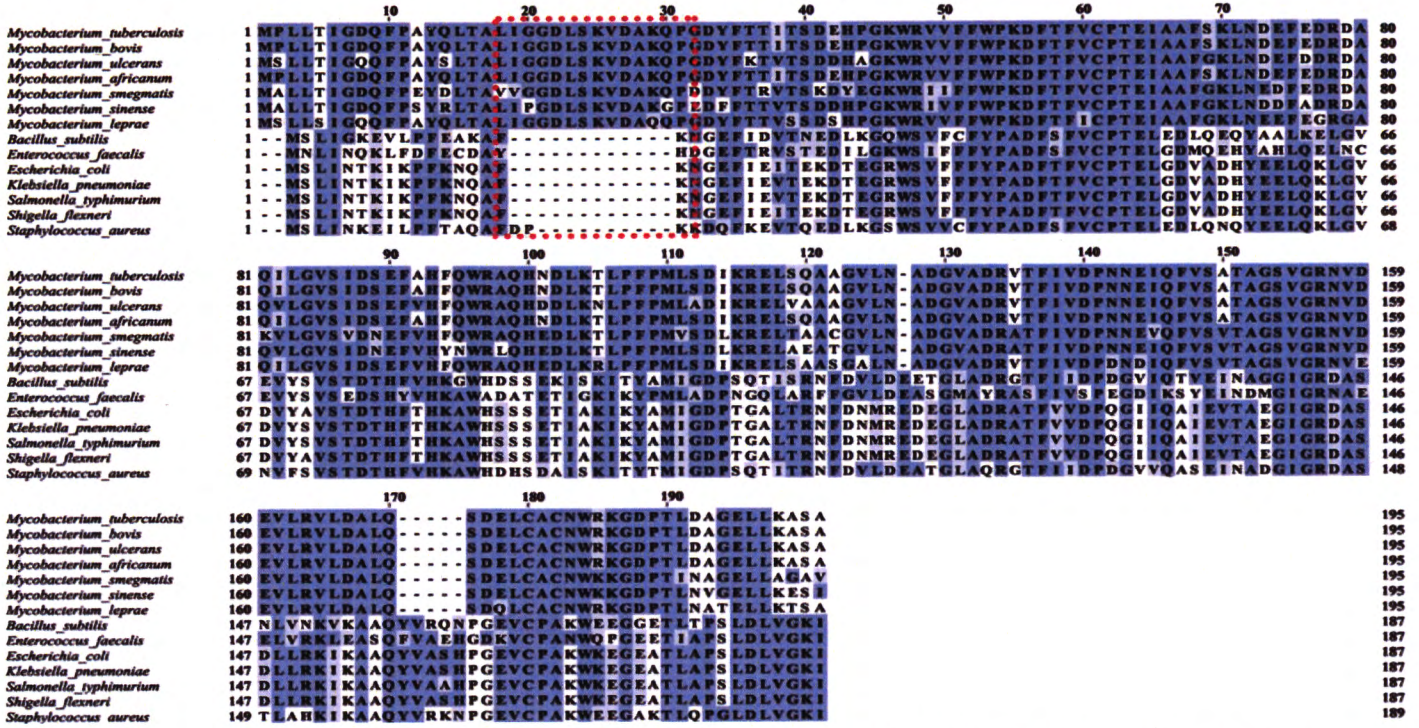

Figure 3.2: *Multiple sequence alignment from ClustalW. The* alignment results from ClustalW revealed that AhpCs from mycobacteria showed a region of amino acids (23-34) that are absent in other species of AhpCs. This region is represented with a *red dashed box*. From the previously reported data [195, 196], it was observed that the deletions of residues 23-34 resulted in no redox-oligomerization and activity of the recombinant mutant, *Mb*AhpC$_{\Delta 23\text{-}34}$. For this study, point mutations were performed in this region of amino acid, to identify critical residues resulting in such results.

Figure 3.3: *Crystallographic structure alignment.* Crystallographic structures of AhpCs of *M. tuberculosis* (PDB ID: 2BMX [193]; *orange*), *E. coli* (PDB ID: 4O5R [188]; *light blue*), *S. enterica* (PDB ID: 4MA9 [185]; *blue*), *H. pylori* (PDB ID: 1ZOF [219]; *magenta*) and *E. faecalis* (unpublished data; *green*) revealed that AhpC structure is highly conserved across all species. However, a region of additional amino acids (23-34), highlighted in *yellow-orange* with *red dashed box*, is observed. This coincides with the sequence alignment analysis from ClustalW (*Figure 3.2*).

3.2 Characterization of wt *Mb*AhpC in solution

In the previous study, the oligomeric states of wt *Mb*AhpC were investigated and results reported that wt *Mb*AhpC in solution showed redox-sensitive oligomerization. Through different techniques such as SEC, DLS and electron microscopy, it was confirmed that *Mb*AhpC$_{OX}$ forms a dimer whereas *Mb*AhpC$_{RED}$ forms a higher order oligomer in solution. In the same study, the NADPH-dependent peroxidase assay performed also demonstrated the enzymatic activity of *Mb*AhpC [195, 196]. These results instigated the need to thoroughly investigate *Mb*AhpC. Therefore, in the current study, 2-dimensional (2D) classifications of electron micrographs, NADPH-dependent peroxidase assay, NMR and HADDOCK modelling experiments were performed, and the results obtained are reported in the subsequent sections.

3.2.1 Effects of redox modulation revealed through electron microscopy

Despite numerous studies postulating that *Mb*AhpC forms a higher oligomer in the reduced state, the number of monomers present was still a debate [180]. The electron micrographs from my previous study confirmed the presence of the ring-like structure of *Mb*AhpC$_{RED}$ in solution [195, 196]. Hence, further analysis on the electron micrographs were performed to confirm the number of dimers present. The analysis was performed kindly by Ms. Zhan Yin and Asst. Prof. Shashi Bhushan from NTU Institute of Structural Biology (SBS, NTU). Two rounds of 2D classifications in RELION were performed. The first round was achieved through the selection of micrographs that

presents particles that can be utilized for 2D class averaging. In this analysis, 37 micrographs were selected for 2D classification and subsequently, the particles were sorted into 32 different classes (Figure 3.4A). The second round of 2D classification was achieved though the selection of 3744 particles and the further averaging of four different classes to improve the image contrast. Results from the final averaged projection showed 12 defined masses (Figure 3.4B, highlighted in asterisks). This result confirms that *Mb*AhpC$_{RED}$ forms a dodecameric-ring in solution.

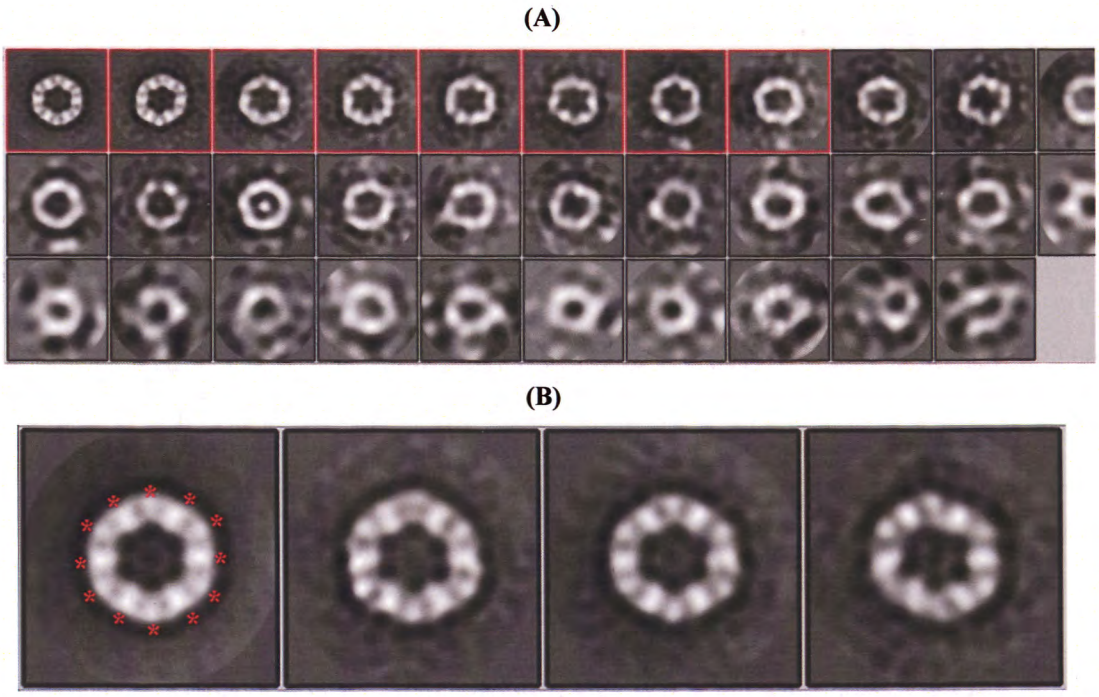

Figure 3.4: *2D-image projections revealing insights into the structure of MbAhpC in solution.* **(*A*)** First-run classifications of electron micrographs. Particles from the red boxed classes were further classified into four classes to improve the quality of 2D classifications. **(*B*)** 2D projection analysis revealed a dodecameric *Mb*AhpC. Each monomer is represented with an asterisk sign, and in total 12 monomers were identied. (Figures A and B are adapted and modified from Wong C.F., *et al* (2017) [196]).

3.2.2 Cloning, expression and purification of *Mb*TrxC and *Mb*TrxB2

In the previous study, it was confirmed that the recombinant *Mb*AhpC was enzymatically active [196]. Therefore, to establish the Michaelis-Menten kinetics of *Mb*AhpC, the thioredoxin system from *M. bovis* was generated. Recombinant *Mb*TrxC and *Mb*TrxB2 will then be utilized to investigate the enzymatic kinetics of *Mb*AhpC.

Following successful molecular cloning (Section 2.2.3), an induction assay and solubility assay (Section 2.2.5) were performed to ensure that *Mb*TrxC and *Mb*TrxB2 were produced in *E. coli* BL21 (DE3) expression strain. This was confirmed on a 17%

SDS-gel. Following which, the recombinant proteins were over-expressed and purified. The recombinant *Mb*TrxC and *Mb*TrxB2 were eluted from Ni^{2+}-NTA column at an imidazole concentration of 150 mM - 250 mM (Figure 3.5A) and 100 mM - 150 mM, respectively (Figure 3.5C).

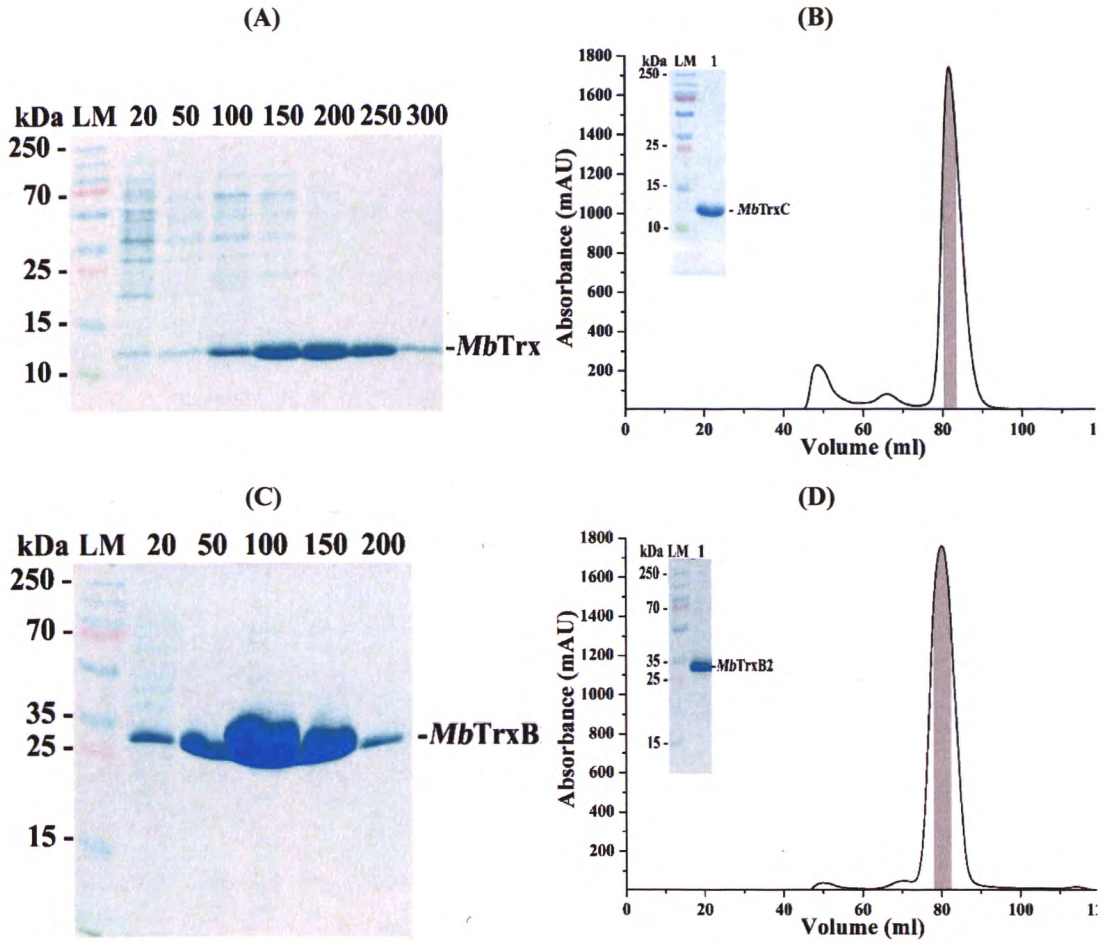

Figure 3.5: *Purification of MbTrxC and MbTrxB2.* **(*A*)** The SDS-gel containing fractions from Ni^{2+}-NTA elution of *Mb*TrxC revealed a high yield of proteins in 150 mM to 250 mM imidazole fraction. **(*B*)** SEC elution profile of *Mb*TrxC revealed that the protein was eluted at approximately 82 ml. The purity of *Mb*TrxC was further confirmed on a 17% SDS-gel, which revealed a clean and homogenous protein at 12 kDa (*inset*). **(*C*)** The SDS-gel containing fractions from Ni^{2+}-NTA elution of *Mb*TrxB2 revealed the presence of a high yield of proteins in 100 mM to 150 mM imidazole fractions. **(*D*)** SEC elution profile of *Mb*TrxB2 revealed that the protein eluted at approximately 80 ml. The purity of *Mb*TrxB2 was further confirmed on a 17% SDS-gel, revealing a clean and homogenous protein at approximately 35 kDa (*inset*).

The fractions containing the protein of interest were then concentrated using a 3 kDa cut off centricon and subjected to size exclusion chromatography to obtain a pure and homogenous protein. Due to the large amount of proteins present in *Mb*TrxC and *Mb*TrxB2, the S75 HiLoad pg and S200 XK16 (GE Healthcare, Sweden) column were used respectively, instead of that mentioned in Section 2.2.7.3. As shown in Figure 3.5B

and 3.5D, a high yield of protein was obtained in the SEC elution profile and only the top 20% (highlighted in grey) of eluted proteins was further utilized for enzymatic kinetic assay.

3.2.3 Enzymatic characterization of wt *Mb*AhpC

After obtaining the consortium of *M. bovis* thioredoxin antioxidant system of recombinant proteins, an enzymatic kinetics assay was performed to confirm the activity of *Mb*AhpC. Previous studies have hypothesized the ability of TrxC to interact with AhpC, however, none have confirmed so [180, 198]. Utilizing TrxC and TrxB2 to provide electrons for *Mb*AhpC, NADPH would then be actively consumed following H_2O_2 reduction. Following the protocol mentioned in Section 2.2.9, this assay confirmed that *Mb*TrxC interacts with *Mb*AhpC as shown in Figure 3.6A, green line. Unlike the control measurement in which no *Mb*AhpC was injected (Figure 3.6A, black line), the decline of NADPH absorbance at 340 nm exemplifies that NADPH oxidation is occurring when *Mb*AhpC interacts with 50 µM of H_2O_2.

Upon confirming that *Mb*AhpC is active with *Mb*TrxC, the enzymatic kinetics of *Mb*AhpC was fully characterized using the Michaelis-Menten plot (Section 2.2.9). The assay performed with increasing concentrations of H_2O_2 from 250 nm to 50 µM, and the outcomes revealed that the Michaelis-constant (K_m) was 2.57 ± 0.36 µM and the catalytic turnover number (k_{cat}) was 0.021 ± 0.001 s^{-1}. *Mb*AhpC exhibited the typical substrate saturation kinetics of the Michaelis-Menten type (Figure 3.6B). To exemplify the significance of this results in comparison to the reported results, the Michaelis-Menten plot was performed with *tert*-butyl hydroperoxide (*t*-BOOH) as the substrate in place of H_2O_2. In the reported study, it was observed that the K_m of *Mt*AhpC with *Mf*TrxC was 5.6 µM [198]. However, in this study, the K_m observed was 2.23 ± 0.49 µM (Table 3.2). This difference may be attributed to the different systems utilized in both studies. In the study performed by Jaeger *et al.* (2004) [198], NADH was utilized as the electron donor as compared to NADPH utilized in the current study. Herein, NADPH was the more relevant electron donor. Therefore, to delineate the importance of *Mb*AhpC enzymatic traits, the same components was utilized apart from the substrate in the current study. The collected enzymatic results have illustrated that the activity of wt *Mb*AhpC with the change in substrate to *t*-BOOH was insignificant when compared with utilizing H_2O_2 as the substrate. With the substrate *t*-BOOH, *Mb*AhpC illustrated a lower K_m of approximately 0.34 µM when compared to utilizing H_2O_2 as the substrate.

However, the k_{cat} values obtained through the utilization of *t*-BOOH as the substrate was insignificantly higher (0.0062 s^{-1}) as compared to utilizing H_2O_2 as the substrate. However, there is a notable change in k_{cat} wherein the utilization of *t*-BOOH as the substrate was approximately 4.03 $M^{-1}s^{-1}$ higher than when compared to utilizing H_2O_2 as the substrate. Nonetheless, both substrates have further confirmed that *Mb*TrxC does indeed interact with *Mb*AhpC (Table 3.2).

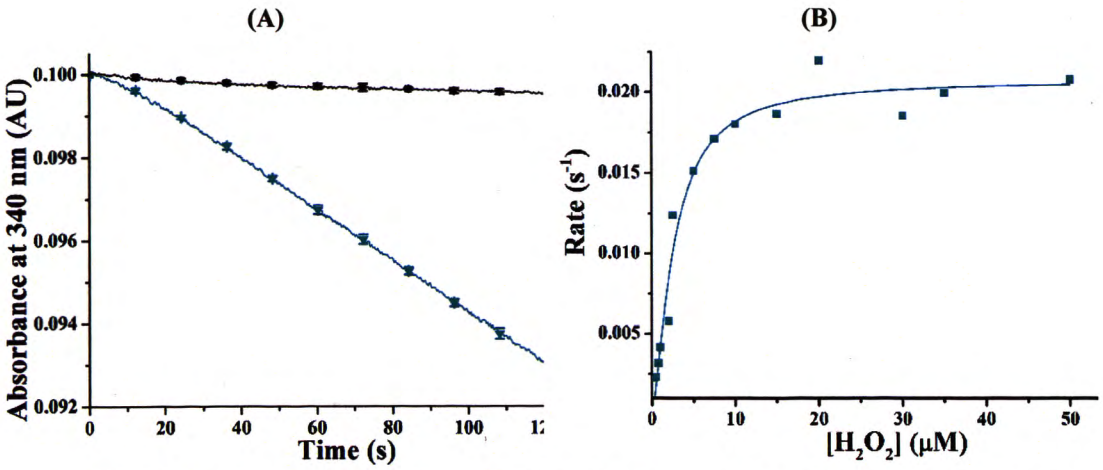

***Figure 3.6**: Enzymatic kinetics analysis of MbAhpC.* **(*A*)** Enzymatic kinetics assay performed with *Mb*TrxC and *Mb*TrxB2 revealed that the consortium of both proteins is capable in reducing *Mb*AhpC. The control (*black line*) is measured to elucidate the accurate activity of *Mb*AhpC (*green line*). Results revealed the decline in NADPH absorbance which illustrates the enzymatic activity of *Mb*AhpC. **(*B*)** Michealis-Menten plot of *Mb*AhpC. The figure illustrates the best fit line with experimental results and the K_m and k_{cat} were determined. The standard deviation of this plot is extremely low, and therefore, cannot be observed from the plot. As such, results of the standard deviation are not plotted in this figure.

***Table 3.2:** Kinetic parameters of mycobacterial AhpC with TrxC*

Protein	k_{cat} ± SD (s^{-1})	K_m ± SD (μM)	k_{cat}/K_m ($M^{-1}s^{-1}$)
H_2O_2 as substrate			
*Mb*AhpC + *Mb*TrxC	0.021 ± 0.001	2.57 ± 0.36	8.17 x 10^3
t-BOOH as substrate			
*Mb*AhpC + *Mb*TrxC	0.0272 ± 0.003	2.23 ± 0.49	12.20 x 10^3

3.2.4 Important binding epitopes of *Mb*TrxC-*Mb*AhpC complex revealed

From the above experiments, it was clearly demonstrated that *Mb*TrxC provides electrons for the successful reduction of H_2O_2 via the reduction of AhpC. Using NMR titration experiments, the binding epitopes of *Mb*TrxC with *Mb*AhpC were studied. The data collection and data analysis were performed under the supervision of Dr. Shin Joon

from Professor G. Grüber's laboratory. ^{15}N-labelled *Mb*TrxC was titrated stepwise with unlabeled *Mb*AhpC and the molecular interaction between both proteins were examined using ^{1}H-^{15}N-HSQC spectrums as mentioned in Section 2.2.12. The interactions were studied from the disappearance and/or decrease in cross peak intensities of ^{15}N-*Mb*TrxC in the ^{1}H-^{15}N-HSQC spectrums (Figure 3.7A).

In addition, slight alterations in ^{15}N- HN-resonances of some residues, gradual line broadening and increase line widths (Figure 3.7B) with increasing molar ratios of *Mb*TrxC to *Mb*AhpC were also observed. This result demonstrates the binding between *Mb*TrxC and *Mb*AhpC. Because of the formation of the *Mb*TrxC-AhpC complex, it resulted in the slow molecular tumbling and fast T2 relaxation time. It was observed that the increase of averaged line-widths before and after complex formation is ~120% of NH and ~90% of ^{15}N resonances, respectively. Significant chemical shift perturbations were also observed in the plot illustrating the chemical shifts at molar ratio of 1:2 (*Mb*AhpC to ^{15}N-*Mb*TrxC). Particularly, in the backbone resonances of C37, C40, M42, V43, E70 and T71 (Figure 3.7C). The increase in CSP for these residues were significantly above the averaged 0.04 $\Delta\delta$ ppm wherein residues C40, M42, V43 and E70 showed increase in CSP of 0.05 to 0.1, and residues C37 and T71 showed increase in CSP of more than 0.1. Hence, these regions are considered as important epitopes for the interaction of *Mb*TrxC with *Mb*AhpC. There are also other residues that may have been affected indirectly because of the protein-protein interactions (Figure 3.7C). These residues include S4, K6, T9, W33, T52, R54, V60, L63, F75, L83, V92, V96, K99, A102 and L115.

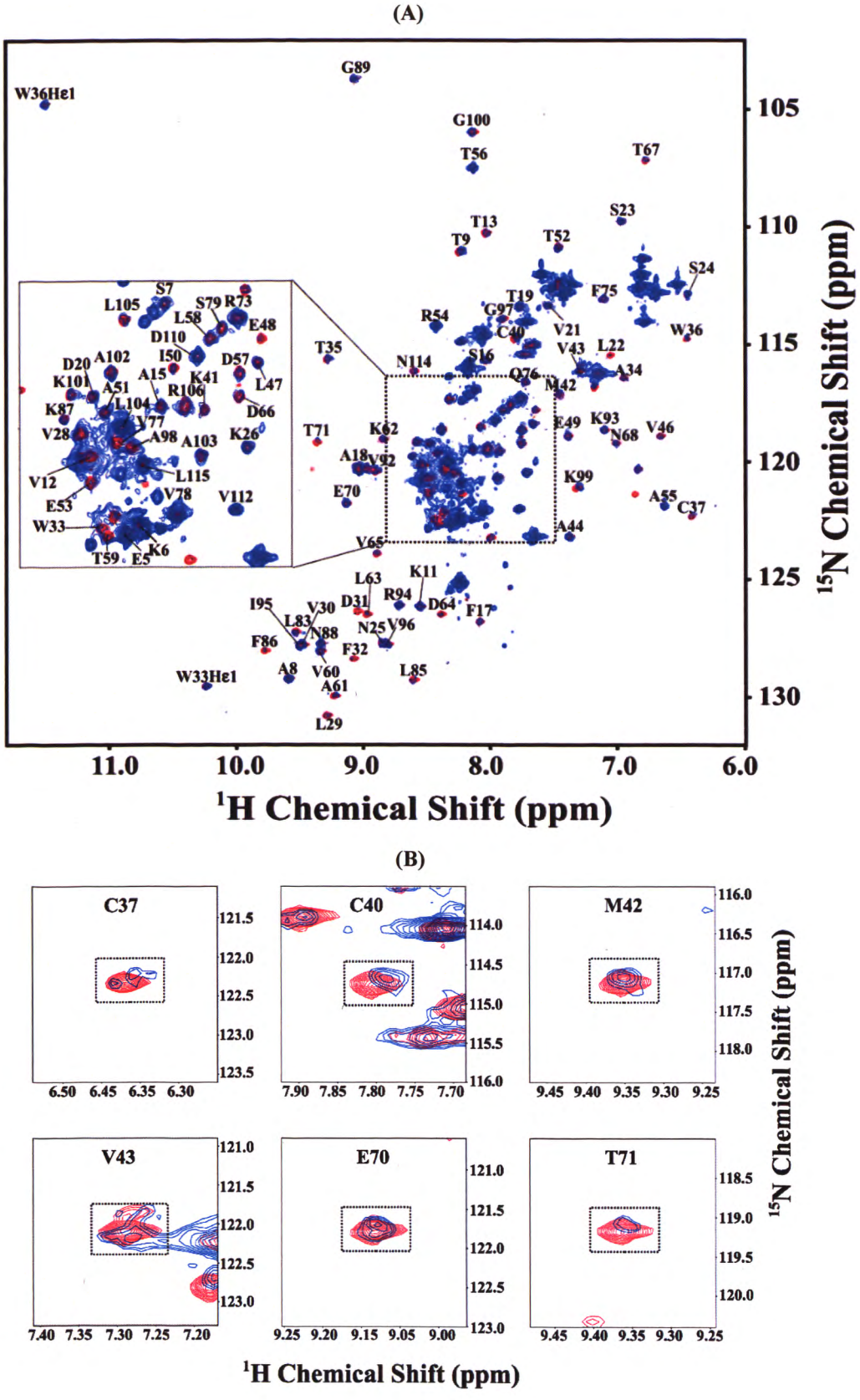

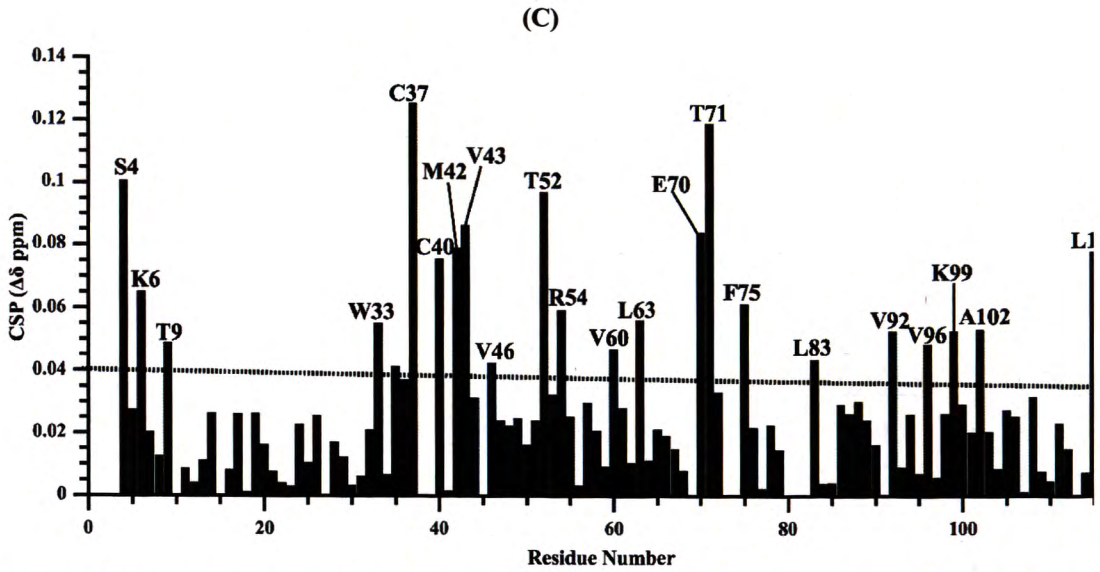

Figure 3.7: *Overlay NMR ^{1}H-^{15}N-HSQC spectra of MbTrxC upon titration with MbAhpC (1:2 molar ratio).* ***(A)*** Superimposition of ^{1}H-^{15}N HSQC spectra of *Mb*TrxC without titration (*represented in red*) and after titration of *Mb*AhpC (*represented in blue*). Backbone resonance assignments are indicated with one-letter amino acid code and sequence number. The disappearance and/or decrease in cross-peak intensities are observed in this superimposition, therefore highlighting the interaction between TrxC and AhpC. ***(B)*** Some residues were zoomed in and selected to highlight cross-peaks that are undergoing significant chemical shift perturbation (CSP). Particularly, it was observed that there are gradual line broadening and increase in line widths upon higher concentration of AhpC titration. This further highlights the interaction between TrxC and AhpC. ***(C)*** A plot shift of CSP at 1:2 molar ratio of *Mb*TrxC:*Mb*AhpC. Differences in chemical shifts were calculated using the formula; $\Delta\delta = [(^{1}H_{free} - {}^{1}H_{bound})^2 + (^{15}N_{free} - {}^{15}N_{bound})_2)]^{½}$. The *dashed line* represents the averaged CSP. The figure illustrated significant chemical shifts particularly in the backbone resonances of C37-V43 and E70-T71 regions.

Figure 3.8A illustrates the identified binding epitopes of *Mb*TrxC and AhpC based on the CSP and NMR linewidth analysis data. The catalytic cysteine residue which provides closer proximity for electron transfer to *Mb*AhpC is also highlighted. Apart from the above-mentioned residues, based on the CSP analysis, D64, V65 and D66 have also been identified as the residues directly involved in the interaction with *Mb*AhpC.

In addition, it was observed in the electrostatic charge distribution of *Mb*TrxC, that residues C37-V43 are more positively charged while the region containing residues E70-T71 are more negatively charged. This may allow several charged interactions between AhpC and TrxC (Figure 3.8B). Figure 3.8C shows the significant changes due to increase in line widths of more than 150% of NH and/or 120% of ^{15}N observed in the backbone resonances of T13, S16-A18, L29, V30, A34, W36, C37, C40, M42-44, V46, E49, I50, D57, A61, D64-D66, T71, A72, F75, V77, S79, L83, G97-K99, A103, L105 and R106, with disappearances in residues D31 and L85.

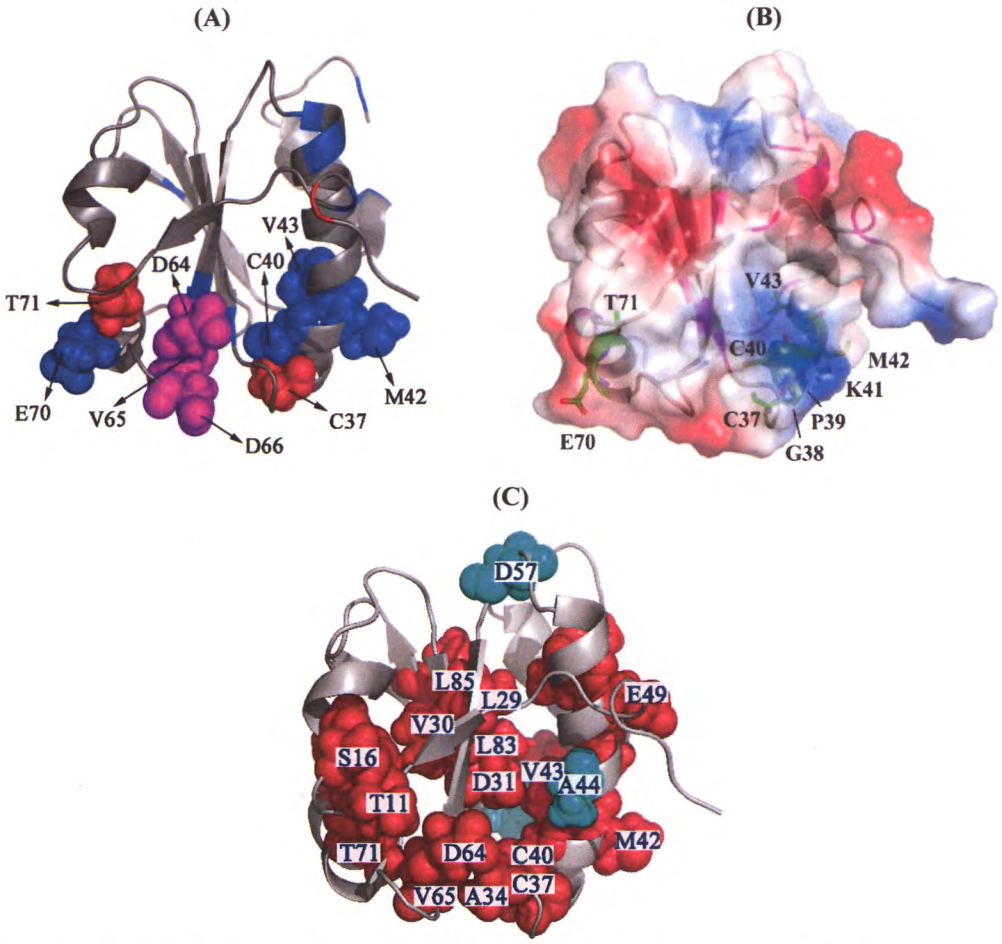

Figure 3.8: **(*A*)** *Sphere* representation of *Mb*TrxC mapped by CSP results. The residues presenting CSP of 0.05 to 0.1 are represented in *blue spheres* whereas the residues presenting CSP more than 0.1 are represented in *red spheres*. From the CSP analysis, residues that interacts with *Mb*AhpC are represented in *magenta spheres*. **(*B*)** *Surface representation* of the electrostatic potential of *Mb*TrxC. Residues more positively charged are highlighted in *blue*, while residues more negatively charged are highlighted in *red*. **(*C*)** Residues showing increased linewidths of more than 150% for NH are represented in *red spheres*, whilst those showing increased linewidths of more than 120% ^{15}N only, are represented in *cyan spheres*.

3.2.5 Model of *Mb*Trx-AhpC complex

To further understand the interaction between *Mb*TrxC-AhpC, the obtained NMR restraints from *Mb*TrxC were used to drive a HADDOCK-docking simulation as described in Section 2.2.13, with the redox-center containing the peroxidatic cysteine C61 and resolving cysteine C174, selected as the binding region for AhpC. The top scoring HADDOCK model was selected with a HADDOCK score of -35 ± 5.9, restraint violation energy of 27.7 ± 14.55 kcal/mol, buried surface area of 1124.8 ± 41.4 Å and Z-score of -0.1.

The resulting *Mb*TrxC-AhpC model revealed the spatial proximity of the catalytic sites; C37 of TrxC was at a distance of 4 Å from C174 of AhpC. One subunit

of the dimer of *Mt*AhpC$_{C176S}$ was shown to have several distributed interactions with TrxC while the other subunit was concentrated near the C-terminal residues of the catalytic side. NMR results performed prior to HADDOCK modeling was further confirmed; by the presence of various hydrogen bonding interactions in this region. Some interactions that were also identified include C37 and G38 of TrxC with D172 of AhpC, and C40 of TrxC with N177 of AhpC. The interacting residues; C37, G48 and C40 of the C37-V43 region of TrxC are herein confirmed with both NMR and HADDOCK modeling. In addition to these residues, the HADDOCK model also revealed other hydrogen bonding interactions with Q76 and V78 of TrxC with K70 and T63 of AhpC, respectively. A strong salt-bridge interaction was also observed in other interfacial region, formed between residues R73 of TrxC and D102 of AhpC, which lies closer to the E70-T71 epitope, wherein E70 interacts with N101 of AhpC through a hydrogen bond (Figure 3.9). It was observed that the inclusion of the additional residues that showed increased line widths in the NMR experiment, did not produce a better complex model in the *Mb*TrxC-AhpC HADDOCK docking.

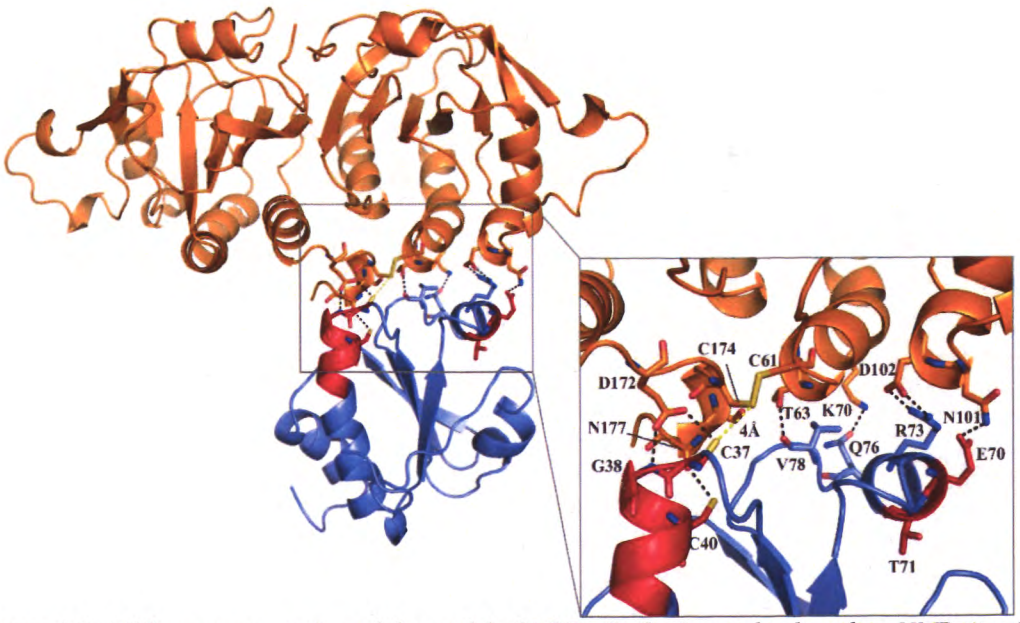

Figure 3.9: *Ribbon representation of the model of MbTrxC-AhpC complex based on NMR titration assays.* TrxC (PDB ID: 2L4Q [213]) is represented in blue and *Mt*AhpC$_{C176S}$ (PDB ID: 2BMX [193]) is represented in orange color. ***(Inset)*** Zoomed in view of the interactions between TrxC and AhpC in the model complex.

3.2.6 *Mb*AhpC hyperoxidation studies

Studies have proposed that hyperoxidation helps in controlling the levels of H_2O_2 in the cell. With controlled levels of H_2O_2, cells maintain a decameric AhpC structure

resulting in the peroxidases' ability to act as chaperones [210]. Hence, it is important to understand if *Mb*AhpC also undergoes the same hyperoxidation. To understand that, the experiment was performed as mentioned in Section 2.2.10.

Results revealed that in comparison to *Ec*AhpC, *Mb*AhpC does not undergo a hyperoxidation reaction even with excess of H_2O_2. In Figure 3.10A, hyperoxidation was observed in *Ec*AhpC where at 0 uM H_2O_2, *Ec*AhpC runs as a monomer. With increasing concentrations of H_2O_2 (from 0.1 mM to 20 mM), the recombinant protein then transits from a monomer to a dimer. Subsequently, it hyperoxidizes to a monomeric form with high H_2O_2 concentrations at 30 mM to 50 mM. On the other hand, *Mb*AhpC (Figure 3.10B) does not form the hyperoxidized monomer. Instead, *Mb*AhpC forms an undefined oligomer at increasing concentrations of H_2O_2 (from 0.1 mM to 20 mM). Instead of forming a hyperoxidized monomer, some of the undefined oligomers start to disappear at higher concentrations of H_2O_2 (from 30 mM to 50 mM). This highly suggests the plausibility that *Mb*AhpC does not undergo hyperoxidation reaction, unlike *Ec*AhpC.

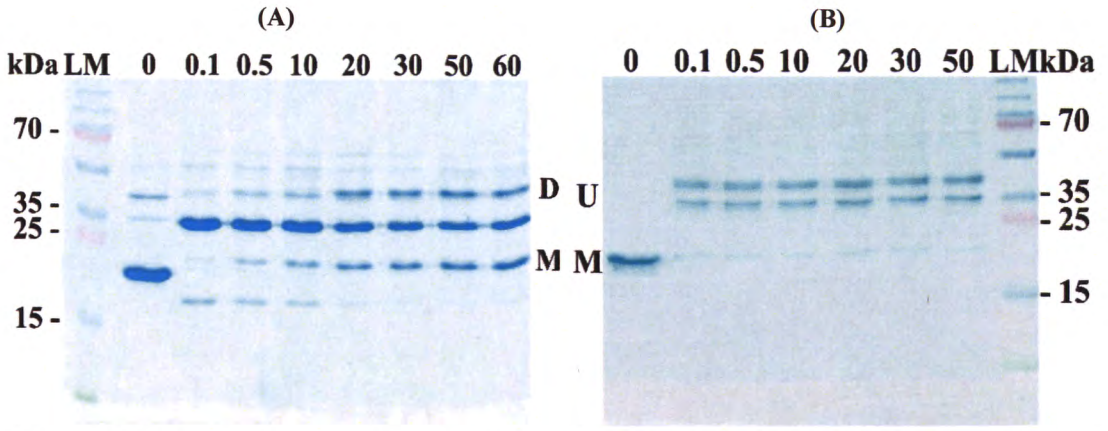

Figure 3.10: *Hyperoxidation studies of EcAhpC and MbAhpC.* **(*A*)** At low concentrations of H_2O_2, *Ec*AhpC forms a defined dimer (*labeled with D*). However, at an increasing concentration of H_2O_2 a gradient formation of the hyperoxidized monomer (*labeled with M*) is observed is *Ec*AhpC. **(*B*)** Unlike *Ec*AhpC, *Mb*AhpC does not form a defined dimer. Instead, presence of undefined oligomers (*labeled with U*) appeared at low concentrations of H_2O_2. Instead of forming the hyperoxidized monomer, the undefined oligomers started to disappear at higher concentrations of H_2O_2.

3.3 Understanding the importance of the N-terminus of *Mb*AhpC

3.3.1 Mutants generated in the N-terminus of *Mb*AhpC

In the previous study, the mutation with the first 15 residues deleted (*Mb*AhpC$_{16\text{-}195}$) resulted in a less soluble protein. Further structural studies into the crystallographic structure of *Mt*AhpC$_{C176S}$ revealed that the deletion in the first 15 residues disrupted the secondary structure of the protein (Figure 3.11A). As such, a second mutant with the first 40 amino acids deleted (*Mb*AhpC$_{41\text{-}195}$) was generated, based on the sequence alignment (Figure 3.1), without disrupting its secondary structure.

Protein production and solubility assays were performed as mentioned in Section 2.2.5, except that to ensure the consistency of results and for comparison purposes, only one buffer was used in solubility test. The buffer used is the same as wt *Mb*AhpC; 50 mM Tris/HCl, pH 7.5, 200 mM NaCl. In the solubility assay, if a protein is soluble, it will be present in the supernatant. An insoluble or less soluble protein will be reflected in the pellet. In spite of avoiding the disruption of the secondary structure, *Mb*AhpC$_{41\text{-}195}$ did not improve in its solubility. On the other hand, it was insoluble as compared to *Mb*AhpC$_{15\text{-}195}$ (Figure 3.11B), whereby majority of the proteins were present in the pellet. This mutation highly suggests the plausibility of the disruption of the secondary structure of *Mb*AhpC and/or the folding of the recombinant protein.

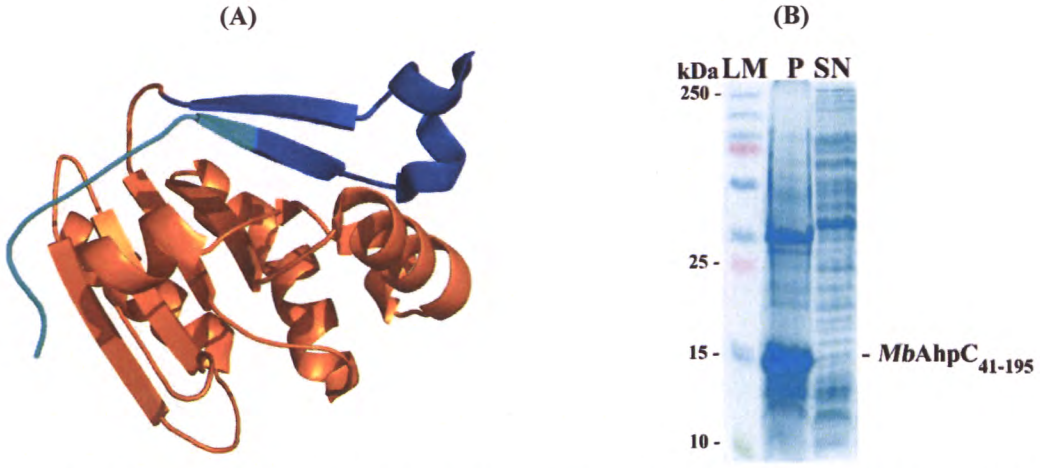

Figure 3.11: *Understanding the N-terminal extension.* **(*A*)** PyMOL visualization of the crystallographic structure of *Mt*AhpC$_{C176S}$ (PDB ID: 2BMX [193]) reveals that the deletion of the first 15 residues disrupts the secondary beta-strand (*highlighted in cyan*). As such *Mb*AhpC$_{41-195}$ was generated with the deletion in the N-terminal residues (*represented in dark blue*). As shown in the solubility assay **(*B*)**, recombinant proteins were present mostly in the pellet as compared to the supernatant, whereby there were no prominent *Mb*AhpC$_{41-195}$ band.

3.3.2 Important residues at the N-terminus of *Mb*AhpC

After understanding the importance of the entire N-terminus, point mutations were generated to highlight the critical residues present in the N-terminus that are important for the functionality of *Mb*AhpC. The mutants generated targeted two specific parts of the N-terminus, firstly, the far end of the N-terminal and secondly, the additional loop observed in *Mb*AhpC that is absent in other bacteria (Figure 3.12, labelled 1 and 2, respectively). The mutants generated are highlighted in the Table 3.3.

Table 3.3: *Point mutations generated to understand the significance of the N-terminal extension and loop residues.*

Mutants	Amino Acid and Residue Number	Change in amino acid
*Mb*AhpC$_{T5A}$	T5	Alanine
*Mb*AhpC$_{T5A/D8A}$	T5	Alanine
	D8	Alanine
*Mb*AhpC$_{T5A/D8A/Y13A}$	T5	Alanine
	D8	Alanine
	Y13	Alanine
*Mb*AhpC$_{D22N/K25Q}$	D22	Asparagine
	K25	Glutamine
*Mb*AhpC$_{D22N/K25Q/D27N}$	D22	Asparagine
	K25	Glutamine
	D27	Asparagine

The choice for mutation of T5 and D8 to alanine to remove charged side chains, thereby increasing the hydrophobic surface. The choice for the mutation in Y13 to alanine is to remove the presence of a bulky side chain such that a simple amino acid would be in its place. The mutation from D22/D27 and K25 to asparagine and glutamine is to remove the presence of charged side chains and replace them with a polar uncharged amino acid. All mutations generated were performed on highly conserved residues in mycobacteria.

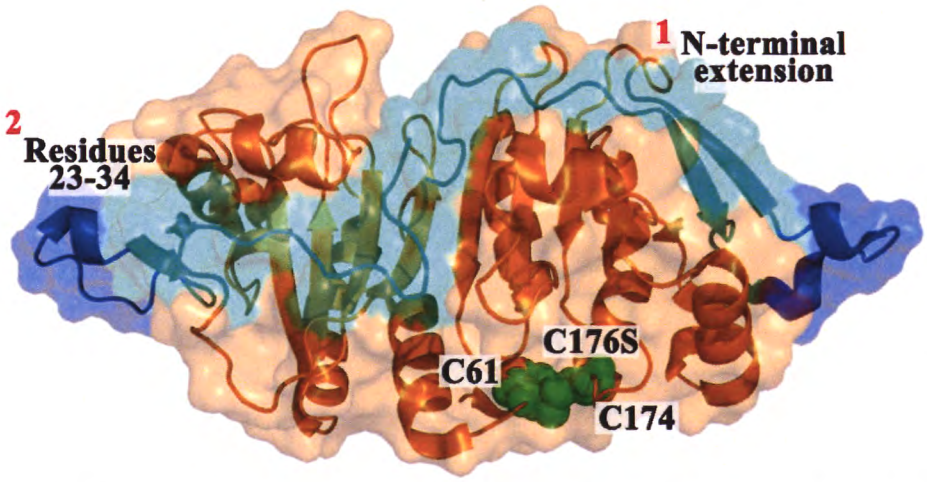

Figure 3.12: *Cartoon and surface representation of MtAhpC$_{C176S}$.* Firstly, *Mt*AhpC carries additional amino acid residues in the N-terminus (*labelled 1*); in which the extension is observed with Clustal-Omega. Secondly, sequence alignment with ClustalW and crystallographic structure alignment revealed that the additional residues reside in the loop (*labelled 2*). Point mutations were made in both regions to identify critical amino acids in *Mt*AhpC that may alter its redox-oligomerization and/or enzymatic activity.

3.3.2.1 Purification of mutants and characterization revealing novel insights into the N-terminal extension

After knowing that the N-terminal deletions (*Mb*AhpC$_{41-195}$ and -AhpC$_{16-195}$) affects the stability of *Mb*AhpC, it is important to identify critical residues that are responsible for this effect. After obtaining the mutants from molecular cloning, the expression and solubility of the proteins were tested following the protocols mentioned in Section 2.2.5. Results revealed that apart from *Mb*AhpC$_{T5A/D8A/Y13A}$, all mutants (-AhpC$_{T5A}$ (Figure 3.13A) and -AhpC$_{T5A/D8A}$ (Figure 3.13B)), showed high expression and solubility. *Mb*AhpC$_{T5A/D8A/Y13A}$ on the other hand, was insoluble, as shown in Figure 3.13C.

Subsequently, to obtain a pure and homogenous *Mb*AhpC$_{T5A}$ and -AhpC$_{T5A/D8A}$, purification was performed as elaborated in Section 2.2.7. All proteins were eluted in

the same imidazole fractions as the wt *Mb*AhpC (at 100 mM imidazole to 250 mM imidazole fractions) [195] and showed no difference on a 17% SDS gel. Thereafter, proteins were pooled and concentrated wherever necessary before subjecting to SEC. Interestingly, these mutants revealed differences in their elution profile as compared to the wt *Mb*AhpC. These elution profiles were further confirmed with DLS.

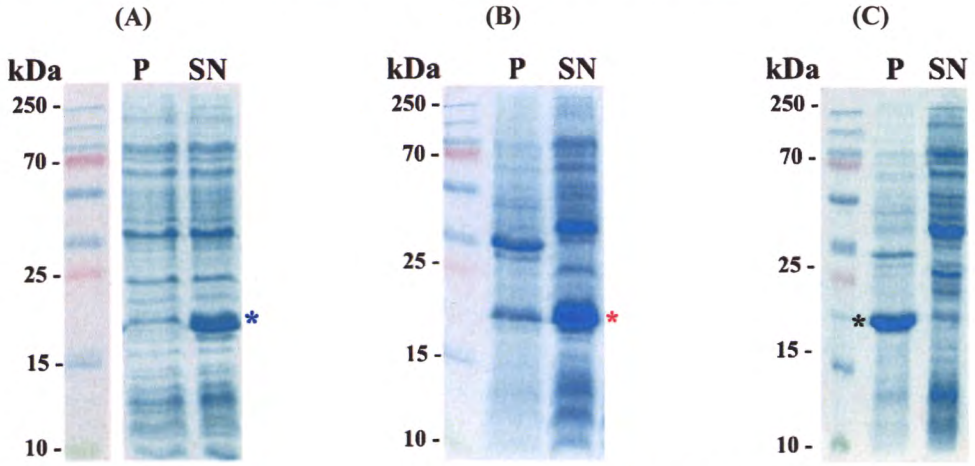

Figure 3.13: *Solubility assay on the N-terminal extension mutants.* **(*A*)** *Mb*AhpC$_{T5A}$ single mutant (*blue asterisk*) and **(*B*)** *Mb*AhpC$_{T5A/D8A}$ double mutant (*red asterisk*) showed high solubility in the solubility assay where majority of the proteins are present in the supernatant (SN). **(*C*)** *Mb*AhpC$_{T5A/D8A/Y13A}$ triple mutant (*black asterisk*) revealed that majority of the proteins are eluted in the pellet (P), revealing the presence of an insoluble protein.

As shown in Figure 3.14A, *Mb*AhpC$_{T5A}$ was eluted as a dimer in the oxidized state, at 16 ml, resembling wt *Mb*AhpC [195]. However, there is an undefined oligomer which also eluted at approximately 13 ml, instead of just a homogenous dimer. Upon reduction with 2 mM DTT, the recombinant protein was unable to form a defined oligomer and instead eluted with a mixture of higher order oligomers (from 12 ml to 16 ml) apart from the dodecamer (*represented by the broadening of the peak*). Herein, it further confirms that the mutation in T5 has disrupted the oligomeric interface, and as such, *Mb*AhpC$_{T5A}$ does not form a defined dodecamer nor dimer on the SEC. The DLS profile (Figure 3.14B) also revealed that the hydrodynamic diameter of *Mb*AhpC$_{T5A\ OX}$ and *Mb*AhpC$_{T5A\ RED}$ is approximately the same (7.071 ± 2.005 nm and 6.752 ± 2.464 nm respectively). Moreover, the percentage of polydispersity was relatively high in the DLS analysis for *Mb*AhpC$_{T5A\ OX}$ (56.8%) and *Mb*AhpC$_{T5A\ RED}$ (49.6%). Both the hydrodynamic diameter and percentage of polydispersity reiterates that the mutation from T5 to alanine has disrupted the stability of *Mb*AhpC$_{T5A}$ redox-sensitive oligomerization, thereby leading to the formation of undefined oligomers. This further confirms the results obtained from the SEC elution profile, wherein the mutation has

altered the oligomeric interface and thereby, also the ability of the protein to form a defined dimer (in oxidizing conditions) or dodecamer (in reducing conditions).

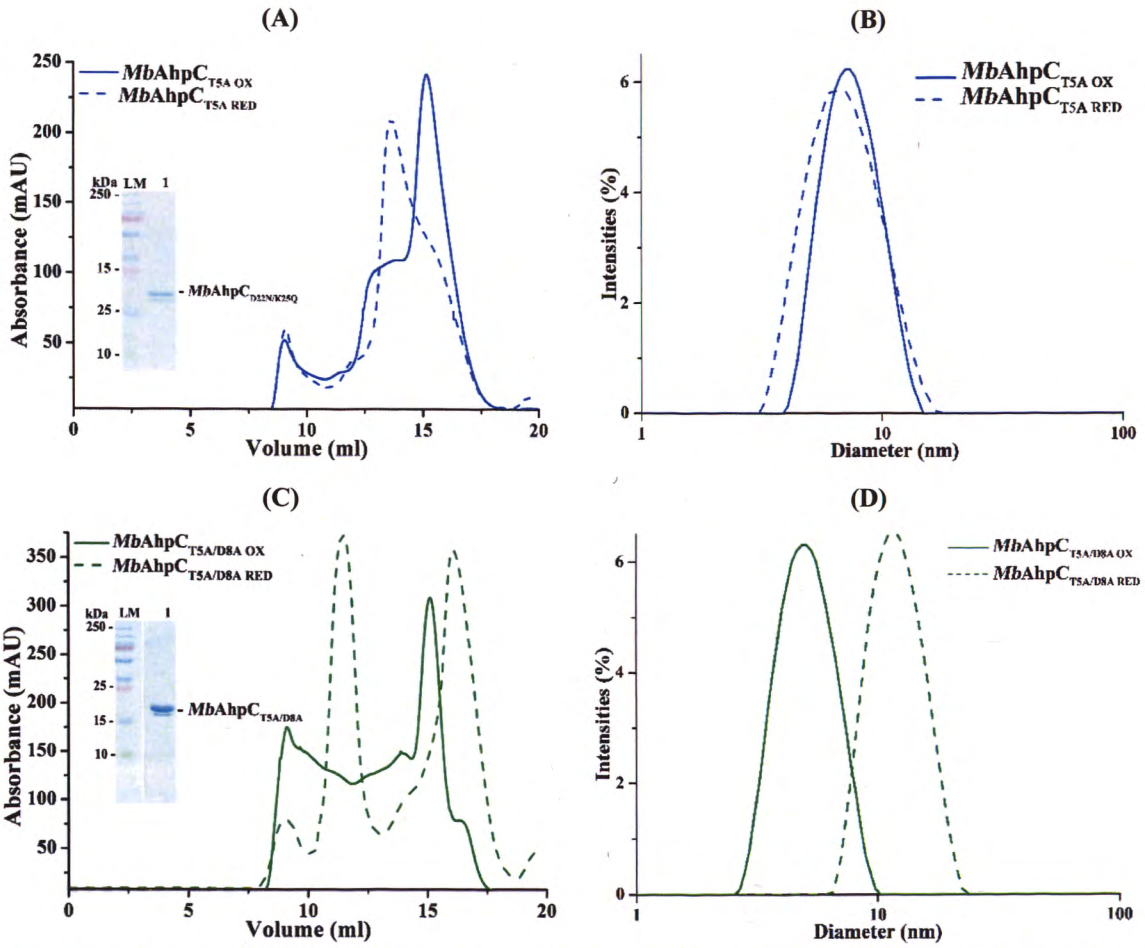

Figure 3.14: *Purification and DLS results for mutants.* **(*A*)** *Mb*AhpC$_{T5A\ OX}$ SEC elution profile highlights that the protein could not be separated well on the SEC wherein no homogenous dimer was present and instead, three peaks were observed (*blue solid line*). *Mb*AhpC$_{T5A\ RED}$ SEC elution profile revealed a mixture of higher order oligomers under reducing conditions (*blue dashed line*). **(*B*)** DLS profiles affirms that the hydrodynamic diameter of the oxidized and reduced *Mb*AhpC$_{T5A}$ was approximately the same. **(*C*)** *Mb*AhpC$_{T5A/D8A\ OX}$ SEC elution profile revealed that the protein could not be separated well with the SEC (*green solid line*) and eluted as a mixture of oligomers and dimers. Despite the addition of the 2 mM DTT, *Mb*AhpC$_{T5A/D8A\ RED}$ SEC elution profile revealed that the protein eluted as both a dodecamer and a dimer (*green dashed line*). **(*D*)** DLS profiles highlights the hydrodynamic diameter of the oxidized and reduced forms of *Mb*AhpC$_{T5A/D8A}$.

Figure 3.14C shows that *Mb*AhpC$_{T5A/D8A}$ was also unable to form a distinct dimer in the oxidized conditions. Instead, higher order oligomers were eluted from 9 ml to 14 ml. Despite the presence of a homogenous oligomer in the reduced conditions, the ratio of oligomers to dimers was 1:1. Unlike wt *Mb*AhpC [195], the presence of a 1:1 ratio in the reduced conditions may indicate that the protein does not form a stable oligomer. This may in part be due to the mutation in the oligomeric interface, which may have altered the redox-sensitive oligomerization of the protein. Results from the

SEC elution profile are further confirmed with DLS (Figure 3.14D), which revealed that the polydispersity of the sample was high (*Mb*AhpC$_{T5A/D8A\ OX}$ = 30.9% and *Mb*AhpC$_{T5A/D8A\ RED}$ = 46.3%), suggesting the possibility of a mixture of oligomeric forms. The study showed that the hydrodynamic diameter of *Mb*AhpC$_{T5A/D8A\ OX}$ was 8.620 ± 2.505 nm, whilst *Mb*AhpC$_{T5A/D8A\ RED}$ was 22.29 ± 10.33 nm. Although the former revealed a similar hydrodynamic diameter when compared with wt *Mb*AhpC, the latter had a significantly higher standard deviation. The presence of a high standard deviation could highlight that the protein forms different oligomers, and as such, during the DLS analysis, the hydrodynamic diameter of *Mb*AhpC$_{T5A/D8A\ RED}$ could not be accurately determined.

3.3.2.2 Characterization of the N-terminal extension mutants via NADPH-peroxidase reduction assay

To examine the effects of the mutations on the functionality of the protein, the mutants were further characterized based on their enzymatic activities following the protocol mentioned in Section 2.2.9. The absorbance of NADPH at 340 nm is proportional to the amount of NADPH utilized by the *Mb*AhpC$_{T5A}$ and -AhpC$_{T5A/D8A}$, whereby the decrease in NADPH absorbance is in proportion to the increase in activity.

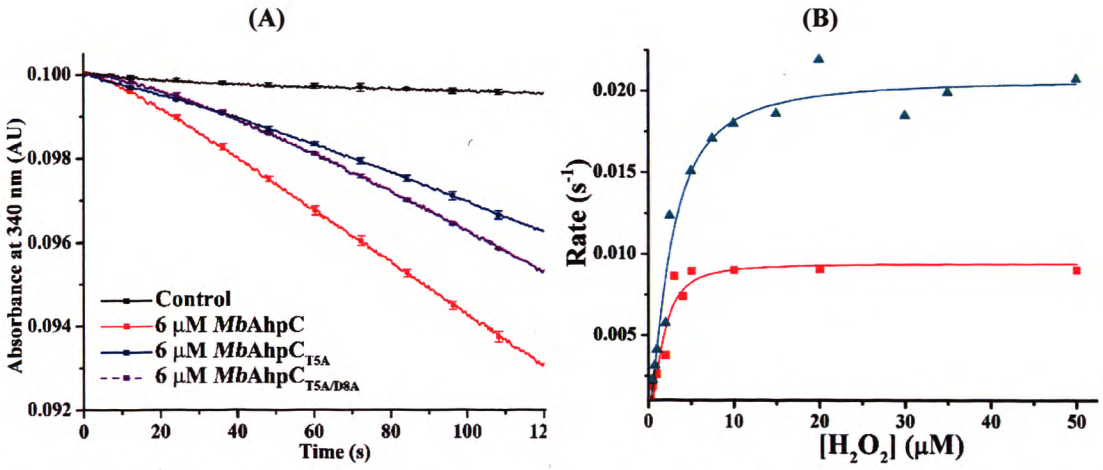

Figure 3.15: *Enzymatic kinetics of the N-terminal extension mutants.* **(*A*)** Overall enzymatic kinetics analysis of *Mb*AhpC$_{T5A}$ and -AhpC$_{T5A/D8A}$ with 50 μM H_2O_2. Results revealed that *Mb*AhpC$_{T5A}$ had approximately less than half of the enzymatic activity whereas *Mb*AhpC$_{T5A/D8A}$ had half of the enzymatic activity when compared with wt *Mb*AhpC. **(*B*)** Michealis-Menten plots of *Mb*AhpC$_{T5A/D/8A}$ (*red solid line*) and wt *Mb*AhpC (*cyan solid line*). The figure illustrates the best fit line with experimental results, and the K_m and k_{cat} were calculated. From the plot, *Mb*AhpC$_{T5A/D/8A}$ shows that the protein reaches its *Vmax* at a much lower concentration as compared to wt *Mb*AhpC.

To fully illustrate the enzymatic aspect of the N-terminal extension, the full Michaelis-Menten plot was obtained for the double mutant only, as both the single and double mutants have approximately the same enzymatic activity.

Results revealed that the inability to form a distinct oligomer reduced the enzymatic activity of *Mb*AhpC$_{T5A/D8A}$ by almost half (Figure 3.15A). To determine its kinetic parameters, the Michaelis-Menten curve was plotted as shown in Figure 3.15B. The results revealed that the K_m and k_{cat} of the *Mb*AhpC$_{T5A/D8A}$ mutant are 1.65 ± 0.32 μM and 0.009 ± 0.001 s^{-1}, respectively. Also, the peroxidatic efficiency (k_{cat}/K_m (H_2O_2)) is 5.44 x10^3 M^{-1} s^{-1}. In comparison to the wt *Mb*AhpC [195, 196], the *Mb*AhpC$_{T5A/D8A}$ mutant has a significant decline in K_m and k_{cat} (0.92 ± 0.04 μM and 0.012 ± 0.001 s^{-1}, respectively).

Furthermore, the peroxidatic efficiency of the mutant also reduced by 34% when compared with wt *Mb*AhpC. This decline of the enzymatic activity suggests that the absence of a stable dodecamer alters the activity of the mutant. Herein, it can be postulated that the effect of redox-modulation is crucial for the enzymatic activity of *Mb*AhpC. Particularly, the crucial amino acids involved in this alteration in both redox-oligomerization and activity, are T5 and D8.

3.3.2.3 NMR titration assays to understand the mutations in the N-terminal extension region

Since the mutant *Mb*AhpC$_{T5A/D8A}$ revealed significant differences in the enzymatic assay, it is important to identify whether the interaction with *Mb*TrxC is hindered. NMR titration assays were performed according to Section 2.2.11.

Results revealed that *Mb*AhpC$_{T5A/D8A}$ did not show significant changes when compared with wt *Mb*AhpC upon titration with ^{15}N-TrxC. In comparison with the wt *Mb*AhpC, the disappearance of resonances and/or chemical shift for residues previously identified as binding epitopes did not significantly alter in the *Mb*AhpC$_{T5A/D8A}$ NMR spectrum (Figure 3.16). This suggests that the mutations did not alter how *Mb*AhpC$_{T5A/D8A}$ interacts with TrxC.

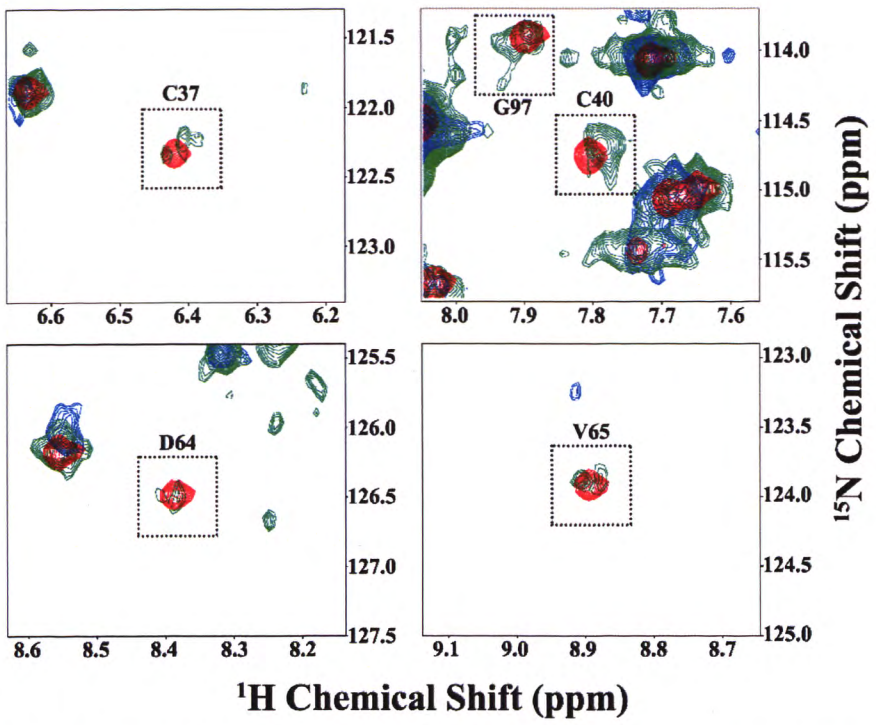

Figure 3.16: *Overlay NMR ^{1}H-^{15}N-HSQC spectra of MbTrxC upon titration with wt MbAhpC and MbAhpC$_{T5A/D8A}$ (1:2 molar ratio).* Superimposition of ^{1}H-^{15}N HSQC spectrum of *Mb*TrxC without titration (*represented in red*) and after titration of *Mb*AhpC (*represented in green*) and *Mb*AhpC$_{T5A/D8A}$ (*represented in blue*). Residues identified that were undergoing significant CSP in wt *Mb*AhpC were also observed in *Mb*AhpC$_{T5A/D8A}$ mutant. Particularly, the gradual line broadening and increase in line widths upon higher concentration of AhpC titration.

3.3.3 N-terminal mutants from residues 23-34

3.3.3.1 Purification of mutants and characterization revealing novel insights into N-terminal region; residues 23-34

From the mutant *Mb*AhpC$_{\Delta 23\text{-}34}$, it was observed that the N-terminal residues 23-34 played a significant role in the redox-oligomerization and activity. The next step is to identify critical residues that alter the functionality of AhpC in this region.

The mutants *Mb*AhpC$_{D22N/K25Q}$ and -AhpC$_{D22N/K25Q/D27N}$ were generated and the expression and solubility of the recombinant proteins were tested. Subsequently, to obtain a pure and homogenous proteins, purification was performed as elaborated in Section 2.2.7. Both proteins were eluted in the same imidazole fractions as the wt *Mb*AhpC (at 100 mM imidazole to 250 mM imidazole fractions), and showed no difference on a 17% SDS-gel. Thereafter, proteins were pooled and concentrated wherever necessary before subjecting to SEC. Interestingly, these mutants did not reveal significant differences when compared with the wt *Mb*AhpC.

Figure 3.17A shows the elution profile of *Mb*AhpC$_{D22N/K25Q\ OX}$. The oxidized form of the recombinant protein showed a defined homogenous dimer, eluting at approximately 16 ml. This coincides with the results of wt *Mb*AhpC$_{OX}$. However, in reducing conditions. *Mb*AhpC$_{D22N/K25Q}$ was eluted as an oligomer and dimer with an approximate ratio of 7:3 respectively. Unlike in wt *Mb*AhpC, the ratio of oligomer to dimer was approximately 9:1. Nonetheless, the majority of the *Mb*AhpC$_{D22N/K25Q\ RED}$ mutant were eluted at the same volume as wt *Mb*AhpC$_{RED}$ (at 12 ml).

On the other hand, *Mb*AhpC$_{D22N/K25Q/D27N}$ also showed a relatively similar elution profile (Figure 3.17C) when compared with the wt *Mb*AhpC. Here, in oxidizing condition, *Mb*AhpC$_{D22N/K25Q/D27N}$ was eluted as a homogenous dimer at 16 ml whereas in the reducing condition, the majority of *Mb*AhpC$_{D22N/K25Q/D27N}$ were eluted as a dodecamer at 12 ml.

Nonetheless, both mutants formed defined oligomers when reduced. The elution profiles were then further confirmed with DLS. Results showed that neither *Mb*AhpC$_{D22N/K25Q\ OX}$ nor -AhpC$_{D22N/K25Q/D27N\ OX}$ showed significant differences in their hydrodynamic diameter when compared with the wt *Mb*AhpC (Figure 3.17B and Figure 3.17D). The hydrodynamic diameter of *Mb*AhpC$_{D22N/K25Q\ OX}$ was 14.14 ± 4.076 nm with 27.5% polydispersity and the hydrodynamic diameter of *Mb*AhpC$_{D22N/K25Q/D27N\ OX}$ was 9.27 ± 4.30 nm, with 46.4% polydispersity. Both oxidized mutants revealed their similarities when compared with wt *Mb*AhpC. Similarly, the hydrodynamic diameter of *Mb*AhpC$_{D22N/K25Q\ RED}$ is 17.01 ± 5.272 nm, with a polydispersity of 29.3%, and *Mb*AhpC$_{D22N/K25Q/D27N\ RED}$ revealed a hydrodynamic diameter of 39.08 ± 20.73 nm, with a polydispersity of 44.6%. Herein, both reduced mutants revealed a similar hydrodynamic diameter when compared with wt *Mb*AhpC, except that the mutants had a higher standard of error. The high standard error could be attributed to the inability of the reduced mutants in forming a defined oligomer.

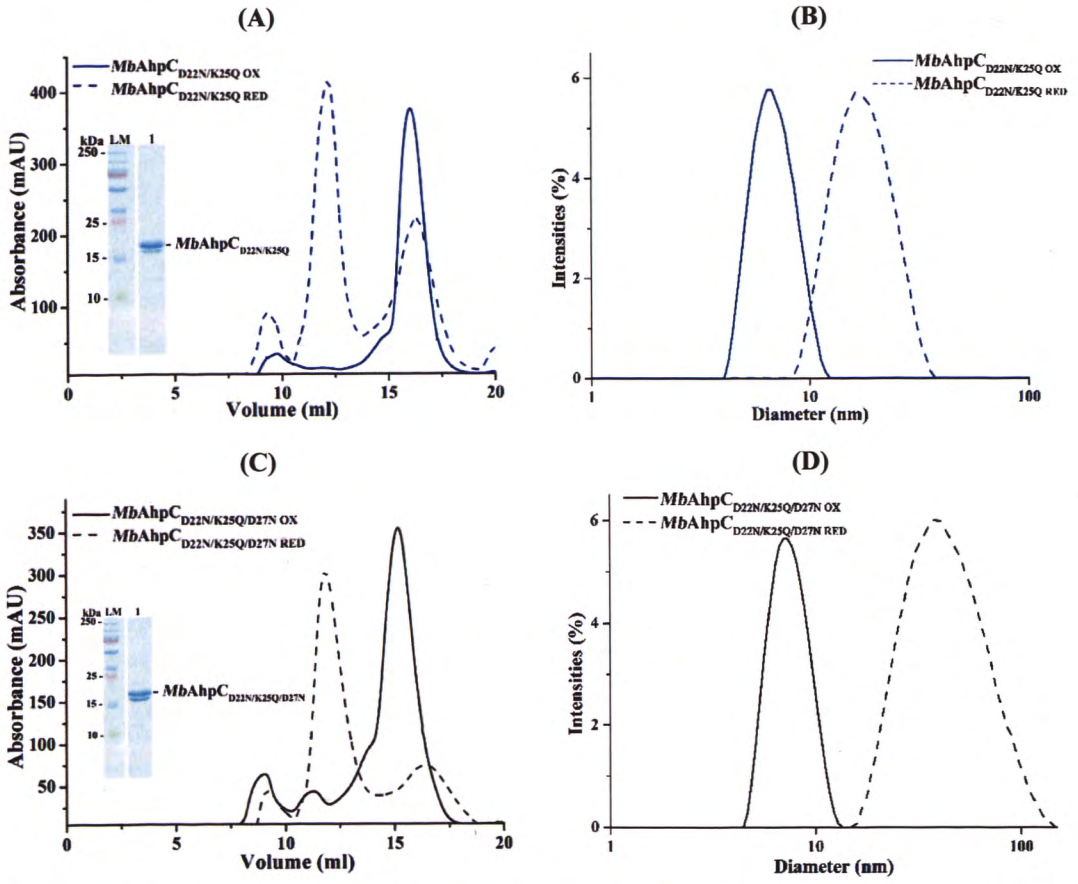

Figure 3.17: *Purification and DLS results for mutants.* Both the **(*A*)** *Mb*AhpC$_{D22N/K25Q\ OX}$ (*blue solid line*) and **(C)** *Mb*AhpC$_{D22N/K25Q/D27N\ OX}$ (*black solid line*) revealed a clean and homogenous dimer on the SEC elution profile. However, in the reduced SEC elution profile of **(*A*)** *Mb*AhpC$_{D22N/K25Q\ RED}$, the ratio of oligomers to dimers was 7:3 (*blue dashed line*) whereas **(*C*)** *Mb*AhpC$_{D22N/K25Q/D27N\ RED}$ had a higher proportion of oligomers as compared to dimers. **(*B*)** DLS profiles of *Mb*AhpC$_{D22N/K25Q}$ in the oxidized (*blue solid line*) and reduced (*blue dashed line*) conditions. **(D)** DLS profiles of *Mb*AhpC$_{D22N/K25Q/D27N}$ in the oxidized (*black solid line*) and reduced (*black dashed line*) conditions. In both reduced mutants, the DLS profiles confirmed the presence of higher order oligomers, from the shift towards the right.

3.3.3.2 Characterization of N-terminal region; residues 23-34, mutants via NADPH-peroxidase reduction assay

Since both the SEC elution profiles and DLS profiles showed that the double and triple mutant did not have significant changes, it is crucial to examine if the activity of the recombinant protein is altered. The enzymatic activities of the mutants were performed based following the protocol mentioned in Section 2.2.9. The results of NADPH-peroxidase reduction assay revealed that *Mb*AhpC$_{D22N/K25Q}$ and -AhpC$_{D22N/K25Q/D27N}$ showed insignificant difference in the NADPH-oxidation when compared to wt *Mb*AhpC (Figure 3.18). This supports the SEC and DLS data, in which the mutants resembled the wt *Mb*AhpC in terms of its redox-sensitive oligomerization and enzymatic activities.

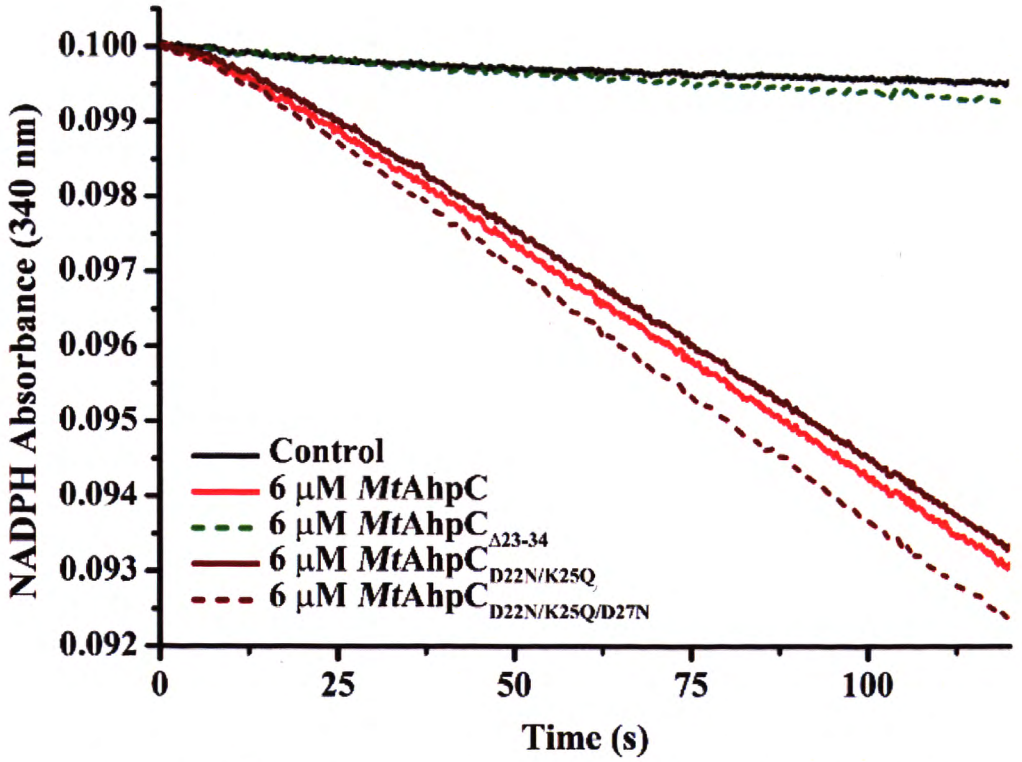

Figure 3.18: *Enzymatic kinetics of N-terminal residues 23-34 mutants.* Results revealed that neither the double (*Mb*AhpC$_{D22N/K25Q}$; *brown solid line*) nor the triple (*Mb*AhpC$_{D22N/K25Q/D27N}$; *brown dashed line*) mutants altered significantly in enzymatic kinetics when compared with wt *Mb*AhpC (*red solid line*). Since neither mutant showed significant changes in enzymatic activity when compared with the wt *Mb*AhpC, no further kinetics assay was performed.

3.3.3.3 NMR titration assays to understand the mutations in the N-terminal region; residues 23-34 region

Since *Mb*AhpC$_{D22N/K25Q}$ and -AhpC$_{D22N/K25Q/D27N}$ did not reveal much significance in their elution profile nor activity, the next question was to understand, if the binding epitopes between *Mb*AhpC-TrxC is altered. NMR titration assays were performed according to Section 2.2.11. The triple mutant, *Mb*AhpC$_{D22N/K25Q/D27N}$ was titrated step-wise into ^{15}N-TrxC. This mutant was selected instead of *Mb*AhpC$_{D22N/K25Q}$ due to its closer similarities to wt *Mb*AhpC. However, results revealed that *Mb*AhpC$_{D22N/K25Q/D27N}$ reacted similarly when compared with the wt *Mb*AhpC. The disappearance of resonances and/or chemical shift in *Mb*AhpC$_{D22N/K25Q/D27N}$ resembled wt *Mb*AhpC (Figure 3.19). This suggests that the selected mutations performed in this region are not significantly important in redox-oligomerization and/or interaction with *Mb*TrxC.

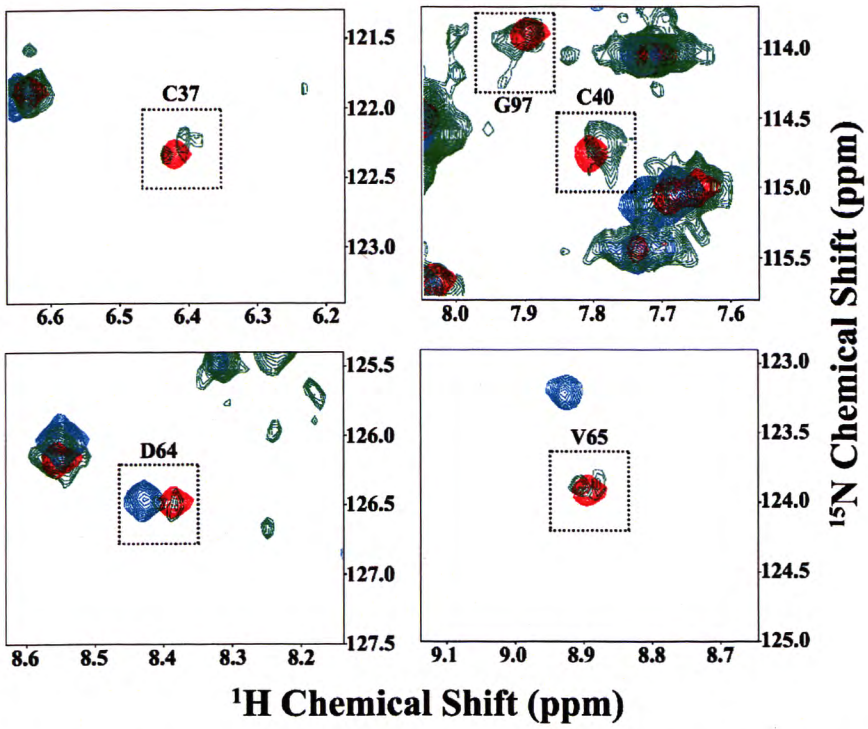

Figure 3.19: *Overlay NMR ^{1}H-^{15}N-HSQC spectr of MbTrxC upon titration with MbAhpC$_{D22N/K25Q/D27N}$ (1:2 molar ratio).* Superimposition of ^{1}H-^{15}N HSQC spectrum of *Mb*TrxC without titration (*represented in red*) and after titration of *Mb*AhpC (*represented in green*). Residues identified that were undergoing significant CSP in wt *Mb*AhpC is also observed in *MbAhpC*$_{D22N/K25Q/D27N}$ mutant (*represented in cyan*). Particularly, the gradual line broadening and increase in line widths upon higher concentration of AhpC titration. This highlights that the binding between TrxC and AhpC may not have been altered with the mutation in D22, K25 and D27.

3.4 Crystallization studies on *Mb*AhpC

Till date, the wt *Mt*AhpC crystallographic structure is not resolved. In addition, the reported crystallographic structure of the *Mt*AhpC$_{C176S}$ mutant was not fully resolved [193]. There are three monomers in *Mt*AhpC$_{C176S}$; monomers A, B and C. However, only amino residues 2 to 170 (out of 195) in monomers A and C and amino acids 2 to 179 in monomer B are resolved and the last 17 residues located at the C-terminal end of the *Mt*AhpC$_{C176S}$ mutant are not resolved in the crystallographic structure. However, structural studies performed thus far has highlighted the significance of the C-terminus in which, it is important for the interaction with its dimeric AhpC partner. In the *St*AhpC$_{C47S}$ mutant, the two dimers form polar interactions at the extreme C-terminus [186]. Also, in *Ec*AhpC, C-terminal truncation studies revealed that the truncations at the very C-terminus prevented the formation of decameric rings. Furthermore, the C-terminus in *Ec*AhpC plays a crucial role in forming a binding epitope with the N-terminal domain of its reducing partner, *Ec*AhpF [220]. Therefore, in the current study,

attempts were made to resolve the full crystal structure of wt *Mb*AhpC in order to establish a crystallization protocol for future atomic structure determination of the mutants generated.

Following the protocol established by Guimaraes *et al.* (2005) [193], wt *Mb*AhpC both in oxidized and reducing conditions were purified using 50 mM Tris/HCl, pH 7.5, 200 mM NaCl and crystal drops were set up in 0.1 M sodium citrate, pH 6.0, 16% ammonium sulfate. Both set-ups were performed with 16 mg/ml of protein concentration. However, as observed in Figure 3.20A, no wt *Mb*AhpC crystals were formed. This could indicate that the mother liquor solution was not appropriate for crystallization conditions or that the salt utilized during purification affected the growth of the crystals. Instead, in Figure 3.20C, wt *Mb*AhpC$_{RED}$ formed a huge precipitate upon setting up of the crystal drop. This also highly indicates that the precipitant (ammonium sulfate) concentration is extremely high for the protein and/or that the pH may have affected the crystal formation. Therefore, with such differences in results, attempts were made to re-purify the protein in 20 mM Tris/HCl, pH 7.5. However, despite optimizing the buffer conditions to the conditions proposed by Guimaraes *et al.*, (2005) [193] (20 mM Tris/HCl, pH 7.5), no crystals were observed in wt *Mb*AhpC$_{OX}$ (Figure 3.20B) whereas a huge precipitate was still observed in wt *Mb*AhpC$_{RED}$ (Figure 3.20D).

Thereafter, the protein concentrations were optimized in both buffers (50 mM Tris/HCl, pH 7.5, 200 mM NaCl and 20 mM Tris/HCl, pH 7.5). Since no protein crystals was observed with 16 mg/ml for wt *Mb*AhpC$_{OX}$, the protein concentration was increased to 20 mg/ml. This increase was performed from the background knowledge that the protein concentration may have been too low for crystals to form. However, the protein concentration for wt *Mb*AhpC$_{RED}$ was reduced to 8 mg/ml, to observe if the precipitation observed before would still form. Nonetheless, Figure 3.20E and 3.20G showed no crystal formation. Therefore, it was further confirmed that 50 mM Tris/HCl, pH 7.5, 200 mM NaCl was not the optimal buffer conditions to use for protein purification. Hence, all crystallization conditions set up thereafter, were performed with proteins purified in 20 mM Tris/HCl, pH 7.5. When wt *Mb*AhpC$_{OX}$ was purified in this buffer conditions and set up in the same mother liquor mentioned above, there were presence of microcrystalline precipitations (Figure 3.20F). This highly indicates a promising sign, in which such hits could be further optimized to lower the nucleation events. On the other hand, Figure 3.20H showed slightly lesser precipitation as compared to Figure

3.20C and 3.20D. Nonetheless, the presence of large precipitation highly suggests that the protein has crashed. Although studies have shown that protein crystals may still form out of these aggregates, there was insufficient time to optimize the conditions utilized for *Mb*AhpC$_{RED}$.

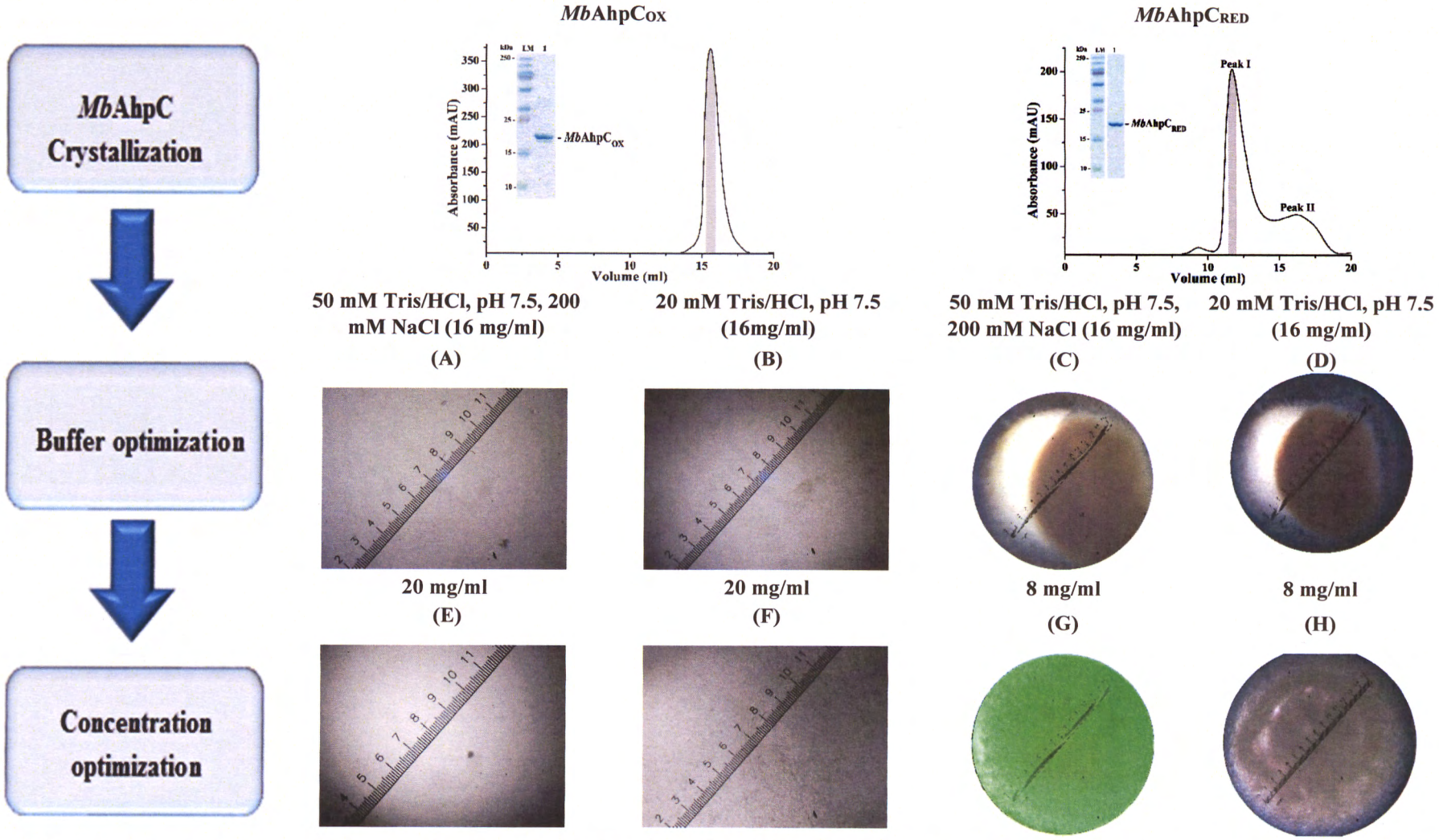

Figure 3.20: *Different crystallization optimization techniques I.* In summary, the SEC elution diagram of *Mb*AhpC$_{OX}$ and *Mb*AhpC$_{RED}$ have been displayed to show the differences in elution patterns of both proteins. Crystallization was performed in hanging drop vaporization and the buffers as well as concentrations are optimized in (A), (B), (C), (D), (E), (F), (G) and (H).

Moving forward, further optimization for wt *Mb*AhpC$_{OX}$ was performed. The methods of setting crystal drops, pH, temperature as well as precipitant concentration were then further optimized in hopes of obtaining crystals. In each optimization process, only one component is altered. This means that an optimization of temperature for example, 10°C, would mean that all other parameters (crystallization buffer and days of incubation) were kept constant. The results of crystallization were illustrated in Figure 3.21.

However, the temperature optimization to lower temperature (10°C and 4°C) in order to initiate a slower process of nucleation, resulted in no growth of crystals (Figure 3.21A and 3.21B). However, as all other parameters were kept constant, the incubation days were also consistent. To rule out that the *Mb*AhpC$_{OX}$ crystals do not form at low temperatures, the crystal drops were analyzed once again after a month. Despite so, there was no presence of microcrystalline precipitates. Here, it highly suggests that low temperature did not induce slower nucleation for *Mb*AhpC$_{OX}$ proteins.

The next parameter for optimization is the concentration of the precipitant. Two precipitant concentrations were chosen, 10% and 12%. However, in both optimization conditions, *Mb*AhpC$_{OX}$ crystallized into microcrystalline precipitates. This suggest that the concentration of the precipitant did not alter significantly the nucleation process of the crystals.

Lastly, the alternative parameter chosen for optimization was the level of pH. Studies have shown that crystal drops set-up with a pH around the pK_a of the protein may form polar contacts and thereby form crystals [221]. However, it is important to also note that slight changes in pH may also induce the formation of crystals. Despite so, in the results observed in the current study, only microcrystalline precipitates were formed (Figure 3.21E and 3.21F).

Although few parameters have been optimized in hopes of getting crystals, none of the chosen parameters induced the growth of crystals. Studies have also advised about the difficulties in crystallizing wt *Mb*AhpC due to its highly flexible C-terminus, which remains unsolved [193]. Due to time constraint, the wt *Mb*AhpC crystallization was put for a stop and attempts were made to crystalize the exact same mutant published in Guimaraes *et al.* (2005) [193]. The mutant *Mb*AhpC$_{C176S}$ was then generated, over-expressed and purified. This was performed to ensure that there are crystallization conditions which could be utilized for crystallizing other mutants.

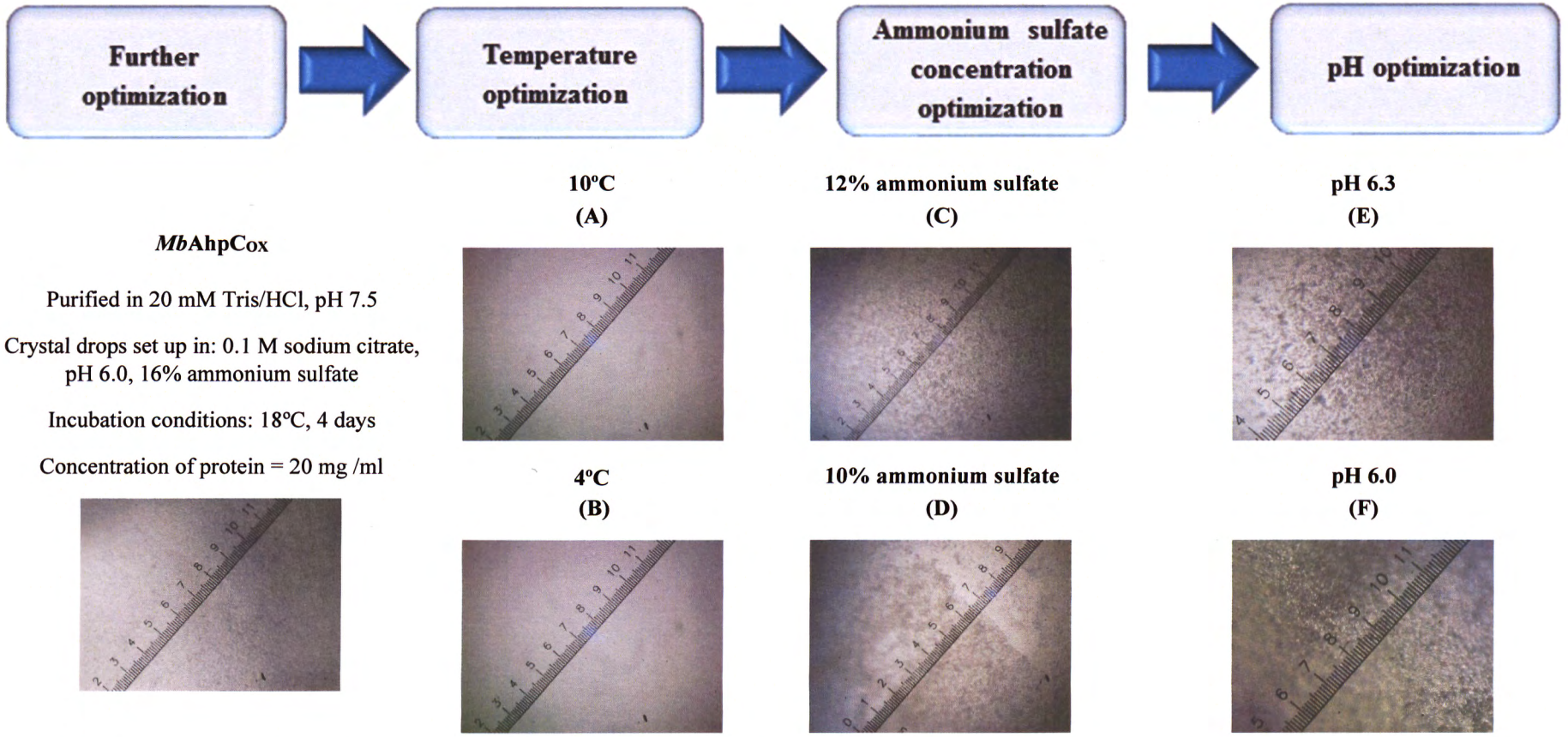

Figure 3.21: *Different crystallization optimization techniques II.* In summary, the SEC elution diagram of *Mb*AhpC$_{OX}$ and *Mb*AhpC$_{RED}$ have been displayed to show the differences in elution patterns of both proteins. Crystallization was performed in hanging drop vaporization and the buffers as well as concentrations are optimized in (A), (B), (C), (D), (E) and (F).

In a comparable manner, crystal drops were set up in attempt to resolve the full crystal structure of *Mb*AhpC. Within four days, large crystals were observed on the drops (Figure 3.22A). As the crystals were obtained just before the beamline time at NSRCC, Hsinchu, Taiwan, the crystals were sent to NSRRC and datasets were collected remotely. Results revealed that the diffraction of the crystals obtained were poor and no further analysis could be performed, as such the cell parameters could not be obtained (Figure 3.22B). Unfortunately, despite following exactly the buffer conditions and crystallization conditions stated in the reported *Mt*AhpC$_{C176S}$ [193], the results published were not reproducible. With that, attempts were made thereafter to optimize the crystallization conditions.

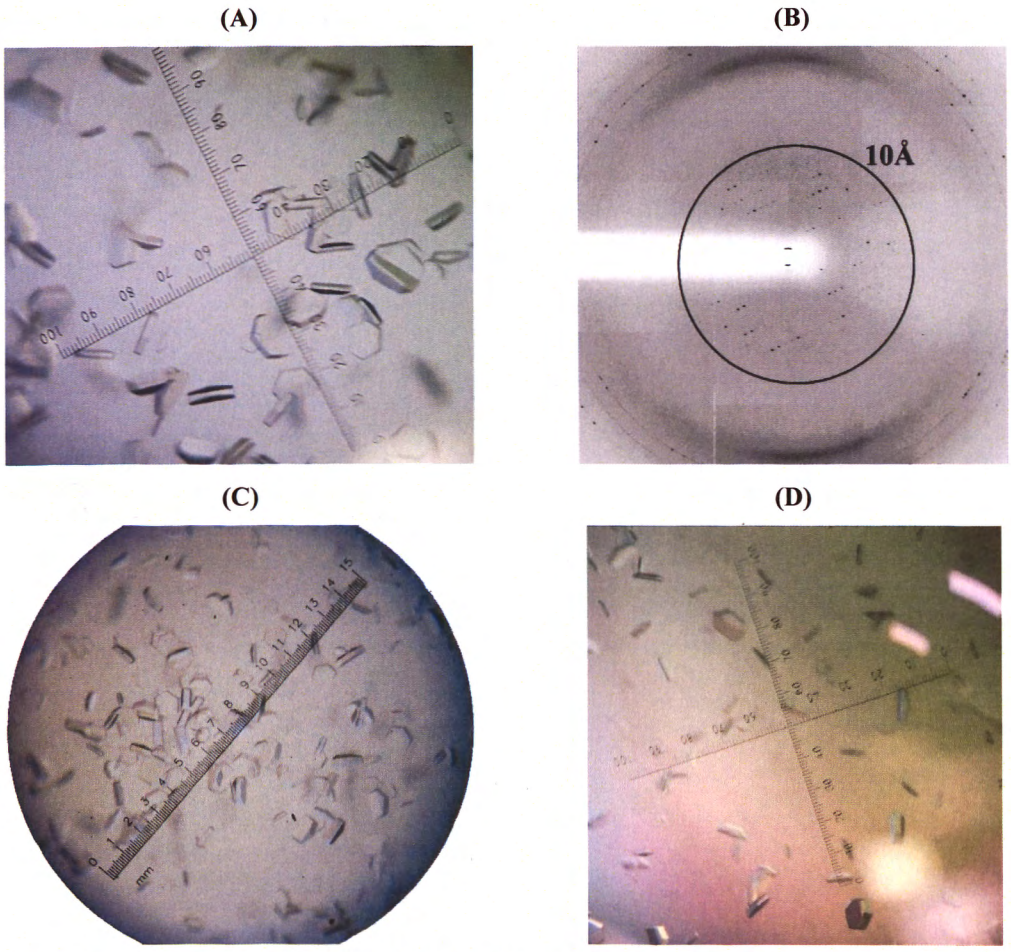

Figure 3.22: *Crystallization of wt MbAhpC and C176S mutant.* **(*A*)** After four days of incubation, large hexagonal crystals were observed. **(*B*)** Diffraction pattern of the *Mb*AhpC$_{C176S}$ mutant revealed that the crystal was approximately 10 Å. As such, optimization **(*C*)** and **(*D*)** were performed to optimize the crystal growth and diffraction.

The initial step of optimization was performed to utilize different vaporization techniques. Instead of using hanging drop vaporization, the sitting drop vaporization technique was utilized. Sitting drop vaporization enforces slower diffusion of the reservoir solution, thereby allowing a slower approach towards supersaturation of the crystals. In addition, the same set up with an incubation at 10°C was set up simultaneously.

However, in both optimization conditions, the diffraction pattern was not obtained yet as the current experiment is still in progress for further optimization. Nonetheless, Figure 3.22C and 3.22D showed that the size of the crystals was approximately the same. With advice from Dr. Asha M. Balakrishna from Professor G. Grüber's laboratory, further optimization may have to be performed to enhance the diffraction of the crystals.

4. Discussion

Discussion

4.1 Structural insights into *Mt*AhpC in solution

Understanding the structure of *Mt*AhpC is crucial in designing possible drug targets to target INH-resistant *M. tuberculosis*. The expression of AhpC for *M. tuberculosis* to adapt to the loss of *katG* functions in patients treated with INH allows the bacteria to enhance its virulence [222]. With increased cases of MDR-TB, it is therefore necessary to characterize this peroxiredoxin to cope with resistant strains of *M. tuberculosis*. Unlike numerous studies performed on other strains of AhpC, few have targeted AhpC produced in mycobacteria. Interestingly, the sequence alignment of AhpC across various pathogenic bacteria has proved that there is a need to study AhpCs in mycobacteria. Here, different sequence alignment algorithms have shown that mycobacteria are unique from other bacteria. The presence of additional residues is located at different regions of the N-terminus in mycobacteria (Figure 3.1 and Figure 3.2). Moreover, the crystallographic structure alignment of AhpC with other bacteria have highlighted significant differences in mycobacteria (Figure 3.13). Henceforth, this further reiterates the need to study the structural aspect of AhpC from mycobacteria.

Despite having solved the crystal structure of the *Mt*AhpC$_{C176S}$ mutant, it remains an enigma. With knowledge from previous studies on peroxiredoxins, scientists around the world are uncertain whether *Mt*AhpC still forms a dodecamer in solution instead of the usual decamer [183]. Studies have argued the plausibility of crystal forces packing, which results in the formation of a dodecameric ring [193]. As such, studies still refer *Mt*AhpC as either a decamer or a dodecamer [180]. Hence, for a suitable drug target design, the unique structure of *Mt*AhpC in solution should be understood. The previous study that was performed have concluded that *Mb*AhpC in solution, elucidates redox-sensitive oligomerization in which *Mb*AhpC$_{OX}$ forms a dimer and *Mb*AhpC$_{RED}$ forms a higher order oligomer. The current study has revealed the presence of a dodecamer in *Mb*AhpC$_{RED}$ (Figure 3.5B) through 2D projections of electron micrographs. The current study has thereby for the first time, confirmed the largely postulated dodecameric structure of *Mb*AhpC$_{RED}$ in solution. Together with the already published data of the *Mb*AhpC$_{C176S}$ mutant crystallographic studies [193], the enigma for the dodecameric ring of *Mb*AhpC in solution, is herein, confirmed.

The next aspect of characterization is to understand the enzymatic kinetics of wt *Mb*AhpC. Through NADPH-hydroperoxide reduction assays, the Michaelis-Menten kinetics was obtained. For a comprehensive comparison, NADPH-hydroperoxide reduction assay was performed both with H_2O_2 and *t*-BOOH as a substrate. Results

show that the *Km* values of both substrates with *Mb*AhpC are similar (Table 3.2). However, there is an increased peroxidatic efficiency of *Mb*AhpC with *t*-BOOH (Table 3.2). The increase in peroxidatic efficiency may indicate the plausibility of *t*-BOOH functioning as a more suitable substrate for *Mb*AhpC instead of the well-known, H_2O_2. This data is different as compared to the data reported by Jaeger *et al* [198], in which NADH was used instead of NADPH for electrons transfer. However, it was reported that the natural electron donor of TrxC is NADPH instead of NADH [199]. Therefore, the current study has shown the first ever measurement of the true *Km* and k_{cat} of wt *Mb*AhpC with its natural electron donor, NADPH.

Many studies performed thus far have elucidated that the enzymatic efficiency of peroxiredoxins in general, are "comparatively poor" in comparison to selenocysteine-containing peroxidases and hemeperoxidases [223]. However, in a study published by Personage *et al.*, (2005), the peroxidatic efficiency of *St*AhpC was equivalently as enzymatically efficient (~10^7 M^{-1} s^{-1}) when compared to selenocysteine-containing peroxidases (~10^8 M^{-1} s^{-1}) and hemeperoxidases (~10^7 M^{-1} s^{-1}) [209]. However, in the current study, it was observed that the overall efficiency of *Mb*AhpC is approximately four orders of magnitude lower (~10^3 M^{-1} s^{-1}). Unlike the experiment performed with *St*AhpC, in which its natural reductant *St*AhpF was utilized, the current study utilizes *Mb*TrxC (a general thioredoxin system). Therefore, the results report in the current study could not be comparative to *St*AhpC. Instead, the current study resolves the enigma [180] as to whether *Mt*TrxC is able to reduce *Mt*AhpC effectively. It is possible to look into the aspect of utilizing *Mt*AhpD, the natural reductant of *Mt*AhpC, in future to make comparative results with *St*AhpC. Also, the results illustrated in the current study utilizes a stopped-flow spectrophotometer to measure the peroxidatic efficiency of *Mb*AhpC. However, in the measurement performed by Personage *et. al.*, (2005) [209], a new assay was established to measure the peroxidatic efficiency of *St*AhpC wherein fluorescence was utilized alongside a stopped-flow spectroflurometer. It is important to note that the utilization of different stopped-flow spectrophotometer and its accuracy of the system may thereby result in the differences in peroxidatic efficiencies observed between *St*AhpC and *Mb*AhpC. To accurately exemplify that *Mb*AhpC is inefficient as a peroxiredoxin, an exact system utilized in *St*AhpC should be utilized as well.

Moving forward, in yet another paper published on the peroxidatic efficiencies of wt *Ec*AhpC revealed that the peroxidatic efficiency of *Ec*AhpC with *Ec*AhpF was approximately 10^4 $M^{-1}s^{-1}$ [224]. Together with this study, a comparative study can be

performed. The study performed utilized the same protocol as established in the current study, and it was clear that the peroxidatic efficiency of both AhpCs are relatively similar. Despite so, another alternative to utilize *Mt*AhpD could also be performed in future to make this comparison more accurate.

With knowledge of the enzymatic kinetics of *Mb*AhpC, it is important to understand if the peroxiredoxin also undergoes hyperoxidation. Hyperoxidation is a process that allows peroxiredoxins to function as molecular chaperones [210]. Previous studies have suggested that instead of undergoing a recycling reaction, hyperoxidation occurs to compete with the formation of disulfide bonds [225]. As shown in Figure 3.11A, *Ec*AhpC undergoes hyperoxidation with increasing concentrations of H_2O_2. The presence of monomers instead of dimers (7:10 ratio) on a SDS-PAGE non-reducing gel clearly indicates the plausibility of hyperoxidation. However, in *Mb*AhpC, at a high concentration (50 μM) of H_2O_2, the amount of monomeric *Mb*AhpC was observed at a ratio of 1:10 (Figure 3.11B). This insignificance may suggest that unlike *Hp*AhpC, excess amount of H_2O_2 may not induce a functional switch to molecular chaperones in *Mt*AhpC [189]. In addition, it is also uncertain whether the process of hyperoxidation is crucial for *Mb*AhpC. Therefore, to fully comprehend whether *Mb*AhpC is able to switch from a peroxiredoxin to a molecular chaperone, further studies should be performed. In a study performed by Dip, P.V (2013), the utilization of an acidic pH (4.4) induced the stacking of the decameric ring in *Ec*AhpC [226], which was further confirmed with electron micrographs (Figure 4.1). It could be possible that although *Mb*AhpC does not undergo a hyperoxidation reaction, the peroxiredoxin could still switch to a molecular chaperone at lower pH.

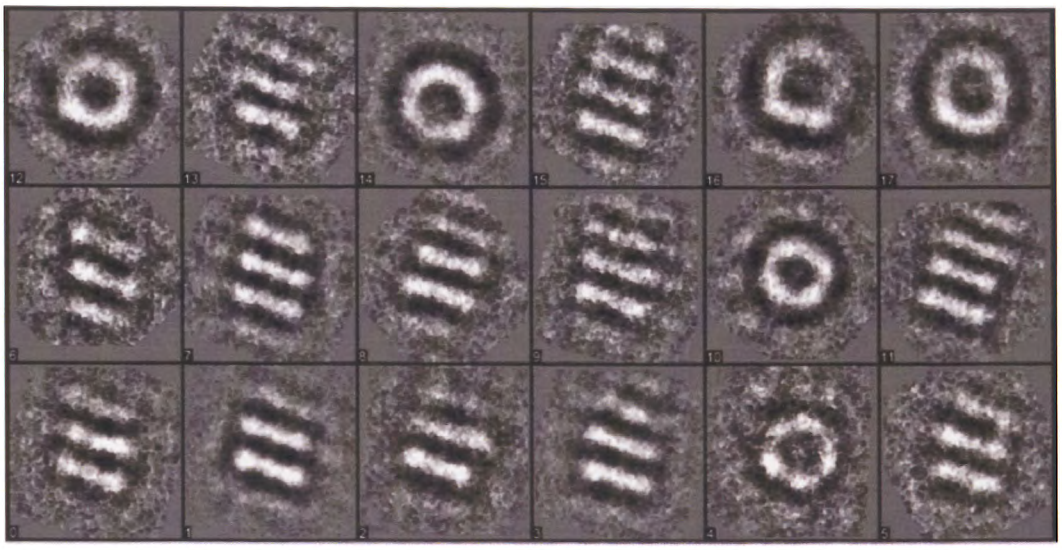

Figure 4.1: *Electron micrographs of the elongated EcAhpC in pH 4.4.* The figure shows that the decameric ring of *Ec*AhpC undergoes a stacking conformation. This figure is adapted from Dip, P.V (2013) [226].

4.2 Biochemical, biophysical and structural studies into the unique N-terminus

The presence of addition conserved N-terminal residues in mycobacteria AhpC can also highlight the structural aspects of this peroxiredoxin. After understanding that deleting the very N-terminus (*Mb*AhpC$_{16\text{-}195}$ and *Mb*AhpC$_{41\text{-}195}$) renders the peroxiredoxin to be highly insoluble and thereby forming undefined oligomers, it is crucial to pinpoint exactly which N-terminal residues results in this phenomenon.

Further studies on the deletion mutant, *Mb*AhpC$_{\Delta 23\text{-}34}$ allowed a comprehensive understanding of the N-terminus. It was observed that the dimer-dimer interface in *Mt*AhpC$_{C176S}$ was stabilized with hydrophobic interactions from residues F57, T58, F91, I114 and V130. Particularly, it was observed that the residues from 23-34 occludes with F91, which is at a distance of 5.5 Å (Figure 4.2). Furthermore, studies have reported a highly-conserved residue W96, that is involved directly with the redox-oligomerization in peroxiredoxins [193]. In *Mt*AhpC$_{C176S}$, W96 is placed alongside F91, F94 and A98 and are present in the helix α2. Residues V26, P31, Y34 and F35 in this extra loop is found to form an ample hydrophobic environment for helix α2. Therefore, the mutant, *Mb*AhpC$_{\Delta 23\text{-}34}$, with these residues removed, may destabilize the hydrophobic environment. Without residues 23-34, the hydrophobic environment occluded by F91 is reduced. In turn, this alters the dimer-dimer stability.

Furthermore, mutations performed at the very N-terminus (*Mb*AhpC$_{T5A}$ and *Mb*AhpC$_{T5A/D8A}$) highlighted important residues for redox-oligomerization. Instead of increasing the hydrophobic environment with the mutation to alanine, the single and

double mutant showed an inability to form a defined dodecamer. In the crystallographic structure, the amino acid, T5 makes water-mediated hydrogen bonding interactions with D132 and G123 of another subunit (Figure 4.3). Hence, the redox-oligomerization may have been affected when T5 is mutated to alanine. Additional studies performed have also showed a significant decline in enzymatic activity of approximately 33% when compared with wt *Mb*AhpC. Herein, the amino acid D8 of one subunit is shown to interact with P2 of another subunit through a water-bridge interaction in the crystallographic structure (Figure 4.3). This occurs at the functional dimer interface. With the mutation to a non-polar alanine, these interactions may have been abolished, thereby weakening the dimeric interface. As a result, both the single and double mutant presented unstable dimer-dodecamers forms as well as decreased activity.

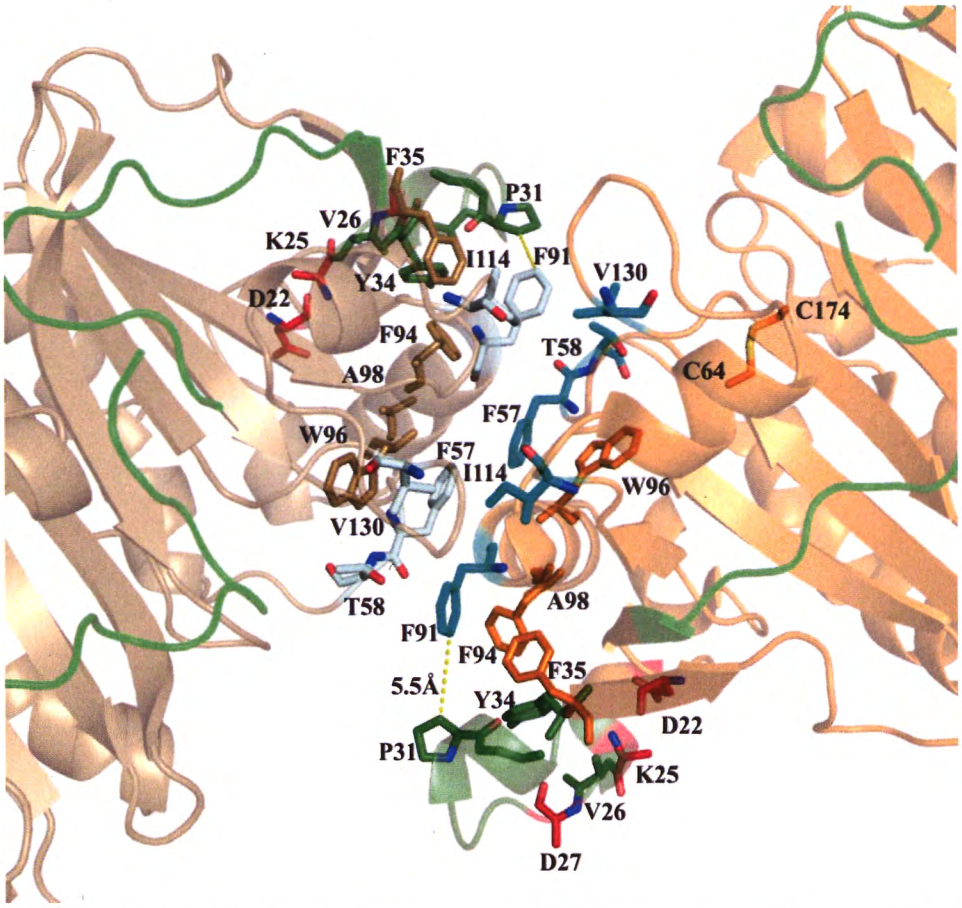

Figure 4.2: *Cartoon representation of the dimeric interface of MtAhpC$_{C176S}$ crystallographic structure (PDB ID: 2BMX)[193].* The first monomer is represented in *orange* and the second monomer in *sand* color. The N-terminal extension (residues 1-15) are highlighted in *green* whereas the N-terminal extra loop (residues 23-34) are highlighted in *forest green*. Hydrophobic residues that are involved in stabilizing the dimeric interface are F57, T58, F91, I114 and V130 (*represented in cyan*). The mutants in the N-terminal residues (D22, K25 and D27) are represented in *red*.

Interestingly, the double and triple mutants, *Mb*AhpC$_{D22N/K25Q}$ and *Mb*AhpC$_{D22N/K25Q/D27N}$ did not show significant changes in the redox-oligomerization or the enzymatic activity. This may be in part due to the location of these residues in the crystallographic structure. The substitutions were made on the charged residues to a polar uncharged amino acid. However, as these residues of the extra loop face the solvent region, it may not alter significantly the hydrophobic environment of the dimeric interface (Figure 4.1 and 4.2). Therefore, the hydrophobic environment, which is formed partially by the N-terminal residues, highlights the importance of these residues.

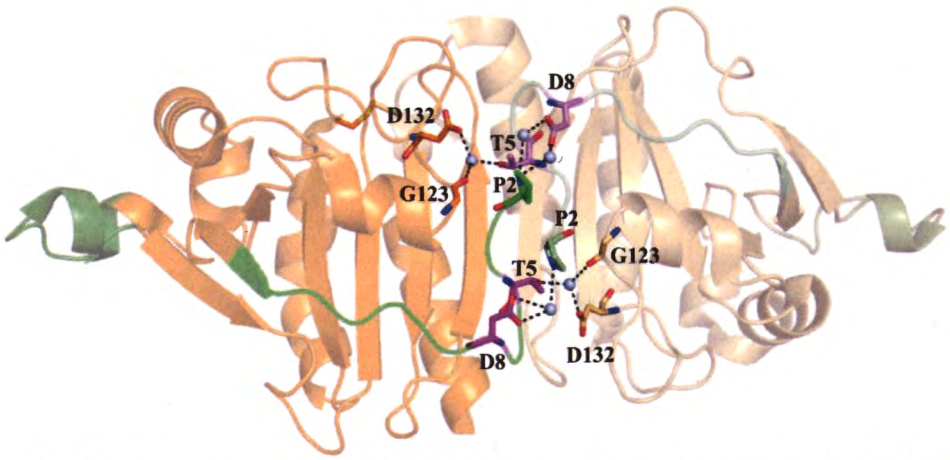

Figure 4.3: *Cartoon representation of MtAhpC$_{C176S}$ crystallographic structure (PDB ID: 2BMX [193]).* Residues that are present in the dimer interface of mycobacteria AhpC are highlighted here where the first subunit is in *orange* and the second in *lighter shade of orange*. The mutants T5 and D8 are represented with *magenta sticks*. The N-terminal extension residues 1-15 are highlighted in *green* and the extra loop (residues 23-34) are highlighted in *forest green*. The water molecules necessary for water mediated interactions are represented in *light blue spheres*.

Contrastingly, the NMR titration results of *Mb*TrxC with the N-terminal mutants did not reveal much. Although the redox-oligomerization of *Mb*AhpC$_{T5A/D8A}$ and *Mb*AhpC$_{D22N/K25Q/D27N}$ as well as its activity were affected, titration results did not reveal significant chemical shift (^{15}N-labelled *Mb*TrxC) changes when compared with wt *Mb*AhpC in the NMR spectrum. Evolution has driven the need for protein-protein interactions to perform their function *in vivo* [227, 228]. NMR spectroscopy is an *in vitro* method to derive protein-protein interactions. The presence of protein-protein interactions will change the chemical environment which subsequently causes chemical shifts. Despite not having much interactions *in vitro*, it is unclear whether the *in vivo* interactions of the mutants with TrxC is affected. Further studies could be performed from the *in vivo* aspect. This could possibly highlight the possible alterations the mutants could have with its interaction with *Mb*TrxC *in vivo*. In addition, TrxC being

one of the many reducing partners for AhpC, might not have been significantly affected. AhpD, as a natural reductant for AhpC [180], on the other hand might reveal differential results in the NMR spectrum when compared with *Mb*TrxC. It would however, be interesting, to understand whether the double and triple mutants would alter the interaction between AhpC-AhpD. Nonetheless, both mutants revealed that there is an ongoing interaction between ^{15}N-*Mb*TrxC and *Mb*AhpC$_{T5A/D8A}$, -AhpC$_{D22N/K25Q/D27N}$.

With these results from the N-terminus, the significance of the additional residues is enhanced. This helps to highlight also into the structural aspect of *Mt*AhpC. The next step after understanding the structural aspect of *Mb*AhpC is to debunk previous contradictory hypothesis about the reducing partner of *Mb*AhpC. From the NADPH-hydroperoxide reduction assay, it is confirmed that *Mb*TrxC reduces *Mb*AhpC effectively (Figure 3.7). Furthermore, NMR titration assays have also confirmed the interaction and its interacting residues between *Mb*TrxC and *Mb*AhpC. In addition, the results of Jaeger *et al.* [198] also support this study. With this, it refutes the proposal that *Mb*AhpC is only reduced by AhpD [180]. Knowing that *Mb*TrxC is efficient in reducing *Mb*AhpC, the question of interest now is the possible interacting residues that form the TrxC-AhpC complex.

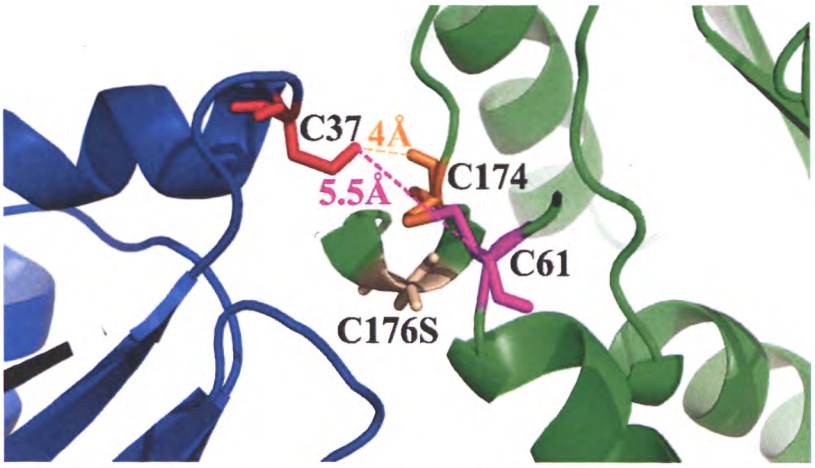

Figure 4.4: *Distance map between MtTrxC (represented in blue) and MtAhpC$_{C176S}$ (represented in green).* The distance of TrxC-C37 is closer in proximity to C174 than to AhpC-C61.

To address the interacting residues, molecular docking was performed with the results obtained from NMR titration assays. Results revealed its interacting residues and thereby allowed a better understanding of the TrxC-AhpC complex formation. Two crucial interactions between *Mt*TrxC and *Mt*AhpC were observed (Figure 3.19). As F68 from *Mt*AhpC lies on the helix α1, it highly suggests that these interactions may induce

a rearrangement of phenylalanine side chains. This rearrangement aids in a helical displacement which is crucial for the formation of an internal cavity. Together with previous studies, the three phenylalanine side chains (F51, F68, F108) have been proposed to be crucial for the rigid-body movement whereby C_P61 and C_R174 are in close proximity. Furthermore, it was observed that C37 of TrxC lies at 4 Å from C_R174 of AhpC. However, the distance between C37 of TrxC and the C_P61 of AhpC was 5.5 Å (Figure 4.4). From this study, the role of the third cysteine might be resolved. In another study performed, it was proposed that three, instead of two cysteines are involved in catalysis [193]. The formation of a disulfide bond between C_P61-C_R174 after condensation reaction would be reduced by C176. Subsequently, a second intramolecular disulfide bond is formed between C174 and C176 [193]. The molecular docking results favor this postulation in which the proximity of C37-TrxC to the C_R174 of AhpC suggests that the second intramolecular disulfide bond can then be reduced by an external thiol, in this case, C37-TrxC.

5. Conclusion

Conclusion

5 Conclusion

Unlike other peroxiredoxins, the crystallographic structure of *Mt*AhpC$_{C176S}$ [193] have brought about various debates about the structure of *Mt*AhpC in solution. However, no structural nor biochemical studies have been performed on *Mt*AhpC. For the first time, the current study has (i) revealed the presence of a dodecameric ring of *Mb*AhpC in solution, (ii) identified the enzymatic kinetic parameters of *Mb*AhpC, (iii) confirmed the reducing equivalent of *Mb*AhpC and its interacting residues and (iv) highlighted the uniqueness of the conserved N-terminus of mycobacteria.

Apart from confirming the highly debatable structure of *Mt*AhpC in solution, the current study has also shown that this peroxiredoxin is unlike others. Instead of forming a decamer, *Mb*AhpC in solution, forms a dodecamer. For the first time ever, the kinetic parameters have been identified for *Mb*AhpC-TrxC. From a superficial comparison to other peroxiredoxins, *Mb*AhpC-TrxC may have presented lower enzymatic kinetics. However, future studies have to be performed to look into the natural reducing partner, AhpD, and its interaction with AhpC to conclude that *Mb*AhpC does indeed have lower peroxidatic efficiency. Nonetheless, the current study has highlighted the substrate specificity of *Mb*AhpC, in which it has been observed that the natural substrate of *Mb*AhpC could likely be *t*-BOOH. In addition, the interacting residues of *Mb*AhpC to *Mb*TrxC were identified. This study provided the much-needed knowledge on the interacting partners of *Mb*AhpC.

Moving forward, the current study has also confirmed the importance of the highly conserved N-terminus of mycobacteria. Mutational studies performed on the charged residues that were predicted to interact with AhpD and/or TrxC have shown that the absence of a stable dodecameric ring alters the enzymatic activity of *Mb*AhpC. To confirm this, further studies such as mutations on the oligomeric interface should be performed to highlight its enzymatic effects. Despite so, the current studies have highlighted, for the first time, that the highly conserved N-terminus, is critical for the stability of *Mb*AhpC.

This study has provided many structural insights into *Mb*AhpC which may bring forward the understanding of how *M. tuberculosis* developed resistance towards INH. With these information, suitable cocktail drugs may then be designed to target the overexpressed protein.

6. References

References

1. World Health Organization. *Global Tuberculosis Report 2015*. 2015; Available from: http://www.who.int/tb/publications/global_report/en/.
2. World Health Organization. *Global Tuberculosis Report 2016*. 2016; Available from: http://www.who.int/tb/publications/global_report/en/.
3. Pai, M., et al., *Tuberculosis.* Nat. Rev. Dis. Primers, 2016. **2**: p. 16076.
4. Centers for Disease Control and Prevention. *Tuberculosis - Get the Facts!* 2016 January 7, 2016; Available from: https://www.cdc.gov/features/tbsymptoms/index.html.
5. Centers for Disease Control and Prevention. *Tuberculosis (Diagnosis of Tuberculosis Disease)*. May 11, 2016; Available from: https://www.cdc.gov/tb/publications/factsheets/testing/diagnosis.htm.
6. Havlir, D.V., et al., *Opportunities and challenges for HIV care in overlapping HIV and TB epidemics.* JAMA, 2008. **300**(4): p. 423-30.
7. Stead , W.W., *Pathogenesis of the Sporadic Case of Tuberculosis.* N. Engl. J. Med., 1967. **277**(19): p. 1008-1012.
8. Esmail, H., et al., *The ongoing challenge of latent tuberculosis.* Philos. Trans. R. Soc. Lond. B Biol. Sci., 2014. **369**(1645): p. 20130437.
9. Ai, J.W., et al., *Updates on the risk factors for latent tuberculosis reactivation and their managements.* Emerg Microbes Infect, 2016. **5**: p. e10.
10. Morrison, J., M. Pai, and P.C. Hopewell, *Tuberculosis and latent tuberculosis infection in close contacts of people with pulmonary tuberculosis in low-income and middle-income countries: a systematic review and meta-analysis.* Lancet Infect. Dis. **8**(6): p. 359-368.
11. Grzybowski, S., G.D. Barnett, and K. Styblo, *Contacts of cases of active pulmonary tuberculosis.* Bull. Int. Union Tuberc., 1975. **50**(1): p. 90-106.

12. McPhedran, F.M. and E.L. Opie, *The Spread Of Tuberculosis In Families12.* Am. J. Epidemiol., 1935. **22**(3): p. 565-643.

13. Frost, W.H., *Risk of Persons in Familial Contact with Pulmonary Tuberculosis.* Am. J. Public Health Nations Health, 1933. **23**(5): p. 426-432.

14. Narasimhan, P., et al., *Risk Factors for Tuberculosis.* Pulm. Med., 2013. **2013**: p. 11.

15. Lonnroth, K., et al., *A consistent log-linear relationship between tuberculosis incidence and body mass index.* Int. J. Epidemiol., 2010. **39**(1): p. 149-55.

16. Raviglione, M.C., et al., *Tuberculosis and HIV: current status in Africa.* AIDS, 1997. **11 Suppl B**: p. S115-23.

17. Harries, A.D., et al., *Deaths from tuberculosis in sub-Saharan African countries with a high prevalence of HIV-1.* The Lancet. **357**(9267): p. 1519-1523.

18. Salaniponi, F.M., et al., *Care seeking behaviour and diagnostic processes in patients with smear-positive pulmonary tuberculosis in Malawi.* Int. J. Tuberc. Lung Dis., 2000. **4**(4): p. 327-32.

19. Harries, A.D., et al., *Treatment outcome of an unselected cohort of tuberculosis patients in relation to human immunodeficiency virus serostatus in Zomba Hospital, Malawi.* Trans. R. Soc. Trop. Med. Hyg., 1998. **92**(3): p. 343-7.

20. Salaniponi, F.M., et al., *Time between sputum examination and treatment in patients with smear-negative pulmonary tuberculosis.* Int. J. Tuberc. Lung Dis., 2000. **4**(6): p. 581-3.

21. Daley, C.L., et al., *An outbreak of tuberculosis with accelerated progression among persons infected with the human immunodeficiency virus. An analysis using restriction-fragment-length polymorphisms.* N. Engl. J. Med., 1992. **326**(4): p. 231-5.

22. Girardi, E., et al., *Incidence of Tuberculosis among HIV-infected patients receiving highly active antiretroviral therapy in Europe and North America.* Clin. Infect. Dis., 2005. **41**(12): p. 1772-82.

23. Girardi, E., et al., *Impact of the HIV epidemic on the spread of other diseases: the case of tuberculosis.* AIDS, 2000. **14 Suppl 3**: p. S47-56.

24. Tan, B.H., et al., *Macrophages acquire neutrophil granules for antimicrobial activity against intracellular pathogens.* J. Immunol., 2006. **177**(3): p. 1864-71.

25. Martineau, A.R., et al., *Neutrophil-mediated innate immune resistance to mycobacteria.* J. Clin. Invest., 2007. **117**(7): p. 1988-94.

26. Young, D.B., H.P. Gideon, and R.J. Wilkinson, *Eliminating latent tuberculosis.* Trends Microbiol., 2009. **17**(5): p. 183-8.

27. Boshoff, H.I. and C.E. Barry, 3rd, *Tuberculosis - metabolism and respiration in the absence of growth.* Nat. Rev. Microbiol., 2005. **3**(1): p. 70-80.

28. Esmail, H., C.E. Barry, and R.J. Wilkinson, *Understanding latent tuberculosis: the key to improved diagnostic and novel treatment strategies.* Drug Discov. Today, 2012. **17**(9-10): p. 514-521.

29. Reed, M.B., et al., *The W-Beijing lineage of Mycobacterium tuberculosis overproduces triglycerides and has the DosR dormancy regulon constitutively upregulated.* J. Bacteriol., 2007. **189**(7): p. 2583-9.

30. Comas, I., et al., *Out-of-Africa migration and Neolithic coexpansion of Mycobacterium tuberculosis with modern humans.* Nat. Genet., 2013. **45**(10): p. 1176-82.

31. Atkinson, Q.D., R.D. Gray, and A.J. Drummond, *mtDNA variation predicts population size in humans and reveals a major Southern Asian chapter in human prehistory.* Mol. Biol. Evol., 2008. **25**(2): p. 468-74.

32. Thomas, T.Y. and S. Rajagopalan, *Tuberculosis and Aging: A Global Health Problem.* Clin. Infect. Dis., 2001. **33**(7): p. 1034-1039.

33. McMurray, D.N., *Guinea Pig Model of Tuberculosis*, in *Tuberculosis*. 1994, American Society of Microbiology.

34. Collins, F.M., *Protection against mycobacterial disease by means of live vaccines tested in experimental animals.* The Mycobacteria: A Sourcebook. Eds, GP Kubica and LG Wayne. New York: Marcel Dekker, 1984: p. 787-839.

35. Collins, F.M., *Animal Models for Tuberculosis Research*, in *Mycobacteria: I Basic Aspects*, P.R.J. Gangadharam and P.A. Jenkins, Editors. 1998, Springer US: Boston, MA. p. 292-307.

36. Lurie, M.B., *Resistance to tuberculosis: experimental studies in native and acquired defensive mechanisms.* Resistance to Tuberculosis: Experimental Studies in Native and Acquired Defensive Mechanisms., 1964.

37. Lurie, M.B., et al., *The response to the intracutaneous inoculation of BCG as an index of native resistance to tuberculosis.* J. Immunol., 1952. **68**(4): p. 369-387.

38. Dutta, N.K., et al., *Genetic requirements for the survival of tubercle bacilli in primates.* J. Infect. Dis., 2010. **201**(11): p. 1743-52.

39. Lin, P.L., et al., *Early events in Mycobacterium tuberculosis infection in cynomolgus macaques.* Infect. Immun., 2006. **74**(7): p. 3790-803.

40. Kaushal, D., et al., *The non-human primate model of tuberculosis.* J. Med. Primatol., 2012. **41**(3): p. 191-201.

41. Clay, H., H.E. Volkman, and L. Ramakrishnan, *Tumor necrosis factor signaling mediates resistance to mycobacteria by inhibiting bacterial growth and macrophage death.* Immunity, 2008. **29**(2): p. 283-294.

42. Davis, J.M., et al., *Real-time visualization of mycobacterium-macrophage interactions leading to initiation of granuloma formation in zebrafish embryos.* Immunity, 2002. **17**(6): p. 693-702.

43. Tobin, D.M. and L. Ramakrishnan, *Comparative pathogenesis of Mycobacterium marinum and Mycobacterium tuberculosis.* Cell. Microbiol., 2008. **10**(5): p. 1027-1039.

44. Sturgill-Koszycki, S., et al., *Lack of acidification in Mycobacterium phagosomes produced by exclusion of the vesicular proton-ATPase.* Science, 1994. **263**(5147): p. 678-681.

45. *Corrections and Clarifications.* Science, 1994. **263**(5152): p. 1359-1359.

46. Lee, B.Y., D.L. Clemens, and M.A. Horwitz, *The metabolic activity of Mycobacterium tuberculosis, assessed by use of a novel inducible GFP expression system, correlates with its capacity to inhibit phagosomal maturation and acidification in human macrophages.* Mol. Microbiol., 2008. **68**(4): p. 1047-60.

47. Pethe, K., et al., *Isolation of Mycobacterium tuberculosis mutants defective in the arrest of phagosome maturation.* Proc. Natl. Acad. Sci., 2004. **101**(37): p. 13642-13647.

48. Simeone, R., et al., *Phagosomal rupture by Mycobacterium tuberculosis results in toxicity and host cell death.* PLoS Pathog., 2012. **8**(2): p. e1002507.

49. Houben, D., et al., *ESX-1-mediated translocation to the cytosol controls virulence of mycobacteria.* Cell. Microbiol., 2012. **14**(8): p. 1287-1298.

50. van der Wel, N., et al., *M. tuberculosis and M. leprae translocate from the phagolysosome to the cytosol in myeloid cells.* Cell, 2007. **129**(7): p. 1287-98.

51. Watson, R.O., et al., *The Cytosolic Sensor cGAS Detects Mycobacterium tuberculosis DNA to Induce Type I Interferons and Activate Autophagy.* Cell Host Microbe, 2015. **17**(6): p. 811-819.

52. Mishra, B.B., et al., *Mycobacterium tuberculosis protein ESAT-6 is a potent activator of the NLRP3/ASC inflammasome.* Cell. Microbiol., 2010. **12**(8): p. 1046-63.

53. Russell, D.G., *The ins and outs of the Mycobacterium tuberculosis-containing vacuole.* Cell. Microbiol., 2016. **18**(8): p. 1065-1069.

54. Kupz, A., et al., *ESAT-6–dependent cytosolic pattern recognition drives noncognate tuberculosis control in vivo.* J. Clin. Invest., 2016. **126**(6): p. 2109-2122.

55. Manzanillo, P.S., et al., *Mycobacterium tuberculosis activates the DNA-dependent cytosolic surveillance pathway within macrophages.* Cell Host Microbe, 2012. **11**(5): p. 469-80.

56. Novikov, A., et al., *Mycobacterium tuberculosis triggers host type I IFN signaling to regulate IL-1beta production in human macrophages.* J. Immunol., 2011. **187**(5): p. 2540-7.

57. Stanley, S.A., et al., *The Type I IFN response to infection with Mycobacterium tuberculosis requires ESX-1-mediated secretion and contributes to pathogenesis.* J. Immunol., 2007. **178**(5): p. 3143-52.

58. Manca, C., et al., *Virulence of a Mycobacterium tuberculosis clinical isolate in mice is determined by failure to induce Th1 type immunity and is associated with induction of IFN-alpha /beta.* Proc. Natl. Acad. Sci. U. S. A., 2001. **98**(10): p. 5752-7.

59. Kunnath-Velayudhan, S. and M.L. Gennaro, *Immunodiagnosis of tuberculosis: a dynamic view of biomarker discovery.* Clin. Microbiol. Rev., 2011. **24**(4): p. 792-805.

60. Rook, G.A.W., K. Dheda, and A. Zumla, *Immune responses to tuberculosis in developing countries: implications for new vaccines.* Nat. Rev. Immunol., 2005. **5**(8): p. 661-667.

61. Lin, P.L., et al., *Sterilization of granulomas is common in active and latent tuberculosis despite within-host variability in bacterial killing.* Nat. Med., 2014. **20**(1): p. 75-79.

62. Boros, D.L. and K.S. Warren, *The bentonite granuloma: Characterization of a model system for infectious and foreign body granulomatous inflammation using soluble mycobacterial, histoplasma and schistosoma antigens.* Immunology, 1973. **24**(3): p. 511-529.

63. Prophylaxis, I.U.A.T.C.o., *Efficacy of various durations of isoniazid preventive therapy for tuberculosis: five years of follow-up in the IUAT trial.* Bull. W.H.O., 1982. **60**(4): p. 555.

64. Manabe, Y.C. and W.R. Bishai, *Latent Mycobacterium tuberculosis-persistence, patience, and winning by waiting.* Nat. Med., 2000. **6**(12): p. 1327-1330.

65. Lillebaek, T., et al., *Molecular evidence of endogenous reactivation of Mycobacterium tuberculosis after 33 years of latent infection.* J. Infect. Dis., 2002. **185**(3): p. 401-404.

66. Comas, I., et al., *Human T cell epitopes of Mycobacterium tuberculosis are evolutionarily hyperconserved.* Nat. Genet., 2010. **42**(6): p. 498-503.

67. Bustamante, J., et al., *Mendelian susceptibility to mycobacterial disease: genetic, immunological, and clinical features of inborn errors of IFN-γ immunity.* Semin. Immunol., 2014. **26**(6): p. 454-470.

68. Frank, S.A. and R.M. Bush, *Barriers to antigenic escape by pathogens: trade-off between reproductive rate and antigenic mutability.* BMC Evol. Biol., 2007. **7**: p. 229.

69. Giacomini, E., et al., *Infection of human macrophages and dendritic cells with Mycobacterium tuberculosis induces a differential cytokine gene expression that modulates T cell response.* J. Immunol., 2001. **166**(12): p. 7033-7041.

70. Flynn, J.L., et al., *Tumor necrosis factor-alpha is required in the protective immune response against Mycobacterium tuberculosis in mice.* Immunity, 1995. **2**(6): p. 561-72.

71. Kindler, V., et al., *The inducing role of tumor necrosis factor in the development of bactericidal granulomas during BCG infection.* Cell, 1989. **56**(5): p. 731-40.

72. Roach, D.R., et al., *TNF regulates chemokine induction essential for cell recruitment, granuloma formation, and clearance of mycobacterial infection.* J. Immunol., 2002. **168**(9): p. 4620-4627.

73. Saunders, B.M. and A.M. Cooper, *Restraining mycobacteria: role of granulomas in mycobacterial infections.* Immunol. Cell Biol., 2000. **78**(4): p. 334.

74. Smith, S., et al., *Local role for tumor necrosis factor alpha in the pulmonary inflammatory response to Mycobacterium tuberculosis infection.* Infect. Immun., 2002. **70**(4): p. 2082-2089.

75. Tsao, T.C.Y., et al., *Imbalances Between Tumor Necrosis Factor-α and Its Soluble Receptor Forms, and Interleukin-1β and Interleukin-1 Receptor*

Antagonist in BAL Fluid of Cavitary Pulmonary Tuberculosis. Chest, 2000. **117**(1): p. 103-109.

76. Tracey, K., et al., *Cachectin/tumor necrosis factor induces cachexia, anemia, and inflammation.* J. Exp. Med., 1988. **167**(3): p. 1211-1227.

77. Furst, D., et al., *Recapitulation of the round-table discussion--assessing the role of anti-tumour necrosis factor therapy in the treatment of rheumatoid arthritis.* Rheumatology (Oxford), 1999. **38**: p. 50-53.

78. Keane, J., et al., *Tuberculosis associated with infliximab, a tumor necrosis factor α–neutralizing agent.* N. Engl. J. Med., 2001. **345**(15): p. 1098-1104.

79. Manadan, A., et al. *Tuberculosis and etanercept.* in *Proceedings of American College of Rheumatology Conference*. 2002.

80. Baker, D.G., et al., *Tuberculosis Occurring In Patients Receiving The Anti-tnf Agent Infliximab.* Arthritis Rheum., 2001. **44**(9): p. S105.

81. Gardam, M.A., et al., *Anti-tumour necrosis factor agents and tuberculosis risk: mechanisms of action and clinical management.* Lancet Infect. Dis., 2003. **3**(3): p. 148-55.

82. Newport, M.J., et al., *A mutation in the interferon-gamma-receptor gene and susceptibility to mycobacterial infection.* N. Engl. J. Med., 1996. **335**(26): p. 1941-9.

83. Jouanguy, E., et al., *Interferon-gamma-receptor deficiency in an infant with fatal bacille Calmette-Guerin infection.* N. Engl. J. Med., 1996. **335**(26): p. 1956-61.

84. de Jong, R., et al., *Severe mycobacterial and Salmonella infections in interleukin-12 receptor-deficient patients.* Science, 1998. **280**(5368): p. 1435-8.

85. Altare, F., et al., *Impairment of mycobacterial immunity in human interleukin-12 receptor deficiency.* Science, 1998. **280**(5368): p. 1432-5.

86. de Beaucoudrey, L., et al., *Revisiting human IL-12Rbeta1 deficiency: a survey of 141 patients from 30 countries.* Medicine (Baltimore), 2010. **89**(6): p. 381-402.

87. Schejbel, L., et al., *Combined IL-12 receptor and IgA deficiency in an adult man intestinally infested by an unknown, non-cultivable mycobacterium.* Scand. J. Immunol., 2011. **74**(6): p. 548-53.

88. Lurie, M.B., *Studies on the mechanism of immunity in tuberculosis.* J. Exp. Med., 1942. **75**(3): p. 247-268.

89. Dannenberg Jr, A., *Pathogenesis of tuberculosis: native and acquired resistance in animals and humans.* Microbiology, 1984. **344**.

90. Wengenack, N.L. and F. Rusnak, *Evidence for isoniazid-dependent free radical generation catalyzed by Mycobacterium tuberculosis KatG and the isoniazid-resistant mutant KatG(S315T).* Biochemistry, 2001. **40**(30): p. 8990-6.

91. Andersen, P., *Tuberculosis vaccines - an update.* Nat. Rev. Microbiol., 2007. **5**(7): p. 484-7.

92. Ottenhoff, T.H.M. and S.H.E. Kaufmann, *Vaccines against Tuberculosis: Where Are We and Where Do We Need to Go?* PLoS Pathog., 2012. **8**(5): p. e1002607.

93. Colditz, G.A., et al., *The efficacy of bacillus Calmette-Guerin vaccination of newborns and infants in the prevention of tuberculosis: meta-analyses of the published literature.* Pediatrics, 1995. **96**(1): p. 29-35.

94. Andersen, P. and T.M. Doherty, *The success and failure of BCG - implications for a novel tuberculosis vaccine.* Nat. Rev. Microbiol., 2005. **3**(8): p. 656-62.

95. Hart, P.D. and I. Sutherland, *BCG and vole bacillus vaccines in the prevention of tuberculosis in adolescence and early adult life.* Br. Med. J., 1977. **2**(6082): p. 293-5.

96. Comstock, G.W., S.F. Woolpert, and V.T. Livesay, *Tuberculosis studies in Muscogee County, Georgia. Twenty-year evaluation of a community trial of BCG vaccination.* Public Health Rep., 1976. **91**(3): p. 276-80.

97. Sterne, J.A., L.C. Rodrigues, and I.N. Guedes, *Does the efficacy of BCG decline with time since vaccination?* Int. J. Tuberc. Lung Dis., 1998. **2**(3): p. 200-7.

98. Fine, P.E., *Variation in protection by BCG: implications of and for heterologous immunity.* The Lancet, 1995. **346**(8986): p. 1339-1345.

99. Datta, M., S. Vallishayee, and S. Diwakara, *Fifteen year follow up of trial of BCG vaccines in south India for tuberculosis prevention.* Indian J. Med. Res., 1999. **110**: p. 56-69.

100. Horwitz, M.A. and G. Harth, *A new vaccine against tuberculosis affords greater survival after challenge than the current vaccine in the guinea pig model of pulmonary tuberculosis.* Infect. Immun., 2003. **71**(4): p. 1672-1679.

101. Horwitz, M.A., et al., *Recombinant bacillus Calmette–Guérin (BCG) vaccines expressing the Mycobacterium tuberculosis 30-kDa major secretory protein induce greater protective immunity against tuberculosis than conventional BCG vaccines in a highly susceptible animal model.* Proc. Natl. Acad. Sci., 2000. **97**(25): p. 13853-13858.

102. Tullius, M.V., et al., *A replication-limited recombinant Mycobacterium bovis BCG vaccine against tuberculosis designed for human immunodeficiency virus-positive persons is safer and more efficacious than BCG.* Infect. Immun., 2008. **76**(11): p. 5200-5214.

103. Hoft, D.F., et al., *A new recombinant bacille Calmette-Guerin vaccine safely induces significantly enhanced tuberculosis-specific immunity in human volunteers.* J. Infect. Dis., 2008. **198**(10): p. 1491-1501.

104. Sun, R., et al., *Novel recombinant BCG expressing perfringolysin O and the over-expression of key immunodominant antigens; pre-clinical characterization, safety and protection against challenge with Mycobacterium tuberculosis.* Vaccine, 2009. **27**(33): p. 4412-4423.

105. Kupferschmidt, K., *Taking a new shot at a TB vaccine.* Science, 2011. **334**(6062): p. 1488-1490.

106. Conradt, P., J. Hess, and S.H.E. Kaufmann, *Cytolytic T-cell responses to human dendritic cells and macrophages infected with Mycobacterium bovis BCG and recombinant BCG secreting listeriolysin.* Microb. Infect., 1999. **1**(10): p. 753-764.

107. Grode, L., et al., *Cell-mediated immunity induced by recombinant Mycobacterium bovis Bacille Calmette-Guerin strains against an intracellular bacterial pathogen: importance of antigen secretion or membrane-targeted antigen display as lipoprotein for vaccine efficacy.* J. Immunol., 2002. **168**(4): p. 1869-1876.

108. Grode, L., et al., *Increased vaccine efficacy against tuberculosis of recombinant Mycobacterium bovis bacille Calmette-Guerin mutants that secrete listeriolysin.* J. Clin. Invest., 2005. **115**(9): p. 2472.

109. Skeiky, Y.A., et al., *Non-clinical efficacy and safety of HyVac4: IC31 vaccine administered in a BCG prime–boost regimen.* Vaccine, 2010. **28**(4): p. 1084-1093.

110. Dietrich, J., et al., *Exchanging ESAT6 with TB10. 4 in an Ag85B fusion molecule-based tuberculosis subunit vaccine: efficient protection and ESAT6-based sensitive monitoring of vaccine efficacy.* J. Immunol., 2005. **174**(10): p. 6332-6339.

111. Doherty, T.M., et al., *Comparative Analysis of Different Vaccine Constructs Expressing Defined Antigens from Mycobacterium tuberculosis.* J. Infect. Dis., 2004. **190**(12): p. 2146-2153.

112. Frick, M., *The tuberculosis vaccines pipeline.* Clayden P, Collins S, Daniels C, et al.; i-Base/Treatment Action Group, 2014.

113. Skeiky, Y.A., et al., *Differential immune responses and protective efficacy induced by components of a tuberculosis polyprotein vaccine, Mtb72F, delivered as naked DNA or recombinant protein.* J. Immunol., 2004. **172**(12): p. 7618-7628.

114. Reed, S.G., et al., *Defined tuberculosis vaccine, Mtb72F/AS02A, evidence of protection in cynomolgus monkeys.* Proc. Natl. Acad. Sci., 2009. **106**(7): p. 2301-2306.

115. Santosuosso, M., et al., *Intranasal boosting with an adenovirus-vectored vaccine markedly enhances protection by parenteral Mycobacterium bovis BCG immunization against pulmonary tuberculosis.* Infect. Immun., 2006. **74**(8): p. 4634-4643.

116. Radošević, K., et al., *Protective immune responses to a recombinant adenovirus type 35 tuberculosis vaccine in two mouse strains: CD4 and CD8 T-cell epitope mapping and role of gamma interferon.* Infect. Immun., 2007. **75**(8): p. 4105-4115.

117. Abel, B., et al., *The novel tuberculosis vaccine, AERAS-402, induces robust and polyfunctional CD4+ and CD8+ T cells in adults.* Am. J. Respir. Crit. Care Med., 2010. **181**(12): p. 1407-1417.

118. McShane, H., et al., *Recombinant modified vaccinia virus Ankara expressing antigen 85A boosts BCG-primed and naturally acquired antimycobacterial immunity in humans.* Nat. Med., 2004. **10**(11).

119. Cardona, P., *RUTI: a new chance to shorten the treatment of latent tuberculosis infection.* Tuberculosis (Edinb), 2006. **86**(3): p. 273-289.

120. von Reyn, C.F., et al., *Prevention of tuberculosis in Bacille Calmette–Guérin-primed, HIV-infected adults boosted with an inactivated whole-cell mycobacterial vaccine.* AIDS, 2010. **24**(5): p. 675-685.

121. Cardona, P.-J., et al., *Immunotherapy with fragmented Mycobacterium tuberculosis cells increases the effectiveness of chemotherapy against a chronical infection in a murine model of tuberculosis.* Vaccine, 2005. **23**(11): p. 1393-1398.

122. Vilaplana, C., et al., *Double-blind, randomized, placebo-controlled Phase I Clinical Trial of the therapeutical antituberculous vaccine RUTI®.* Vaccine, 2010. **28**(4): p. 1106-1116.

123. Stanford, J., C. Stanford, and J. Grange, *Immunotherapy with Mycobacterium vaccae in the treatment of tuberculosis.* Front. Biosci., 2004. **9**: p. 1701-19.

124. van den Boogaard, J., et al., *New drugs against tuberculosis: problems, progress, and evaluation of agents in clinical development.* Antimicrob. Agents Chemother., 2009. **53**(3): p. 849-62.

125. Ndjeka, N., et al., *Treatment of drug-resistant tuberculosis with bedaquiline in a high HIV prevalence setting: an interim cohort analysis.* Int. J. Tuberc. Lung Dis., 2015. **19**(8): p. 979-85.

126. Guglielmetti, L., et al., *Compassionate use of bedaquiline for the treatment of multidrug-resistant and extensively drug-resistant tuberculosis: interim analysis of a French cohort.* Clin. Infect. Dis., 2015. **60**(2): p. 188-94.

127. Gupta, R., et al., *Delamanid and QT prolongation in the treatment of multidrug-resistant tuberculosis.* Int. J. Tuberc. Lung Dis., 2015. **19**(10): p. 1261-2.

128. Ryan, N.J. and J.H. Lo, *Delamanid: First Global Approval.* Drugs, 2014. **74**(9): p. 1041-1045.

129. Gler , M.T., et al., *Delamanid for Multidrug-Resistant Pulmonary Tuberculosis.* N. Engl. J. Med., 2012. **366**(23): p. 2151-2160.

130. United States Food and Drug Administration. 2012; Available from: https://www.accessdata.fda.gov/scripts/cder/daf/index.cfm?event=overview.process&applno=204384.

131. The European Commission. *Deltyba.* 2014; Available from: http://www.ema.europa.eu/ema/index.jsp?curl=pages/medicines/human/medicines/002552/human_med_001699.jsp&mid=WC0b01ac058001d124.

132. World Health Organization. *Mulitdrug-Resistant Tuberculosis (MDR-TB).* 2016; Available from: http://www.who.int/tb/challenges/mdr/mdr_tb_factsheet.pdf.

133. Crofton, J. and D. Mitchison, *Streptomycin resistance in pulmonary tuberculosis.* Br. Med. J., 1948. **2**(4588): p. 1009.

134. Jaramillo, E., *Guidelines for the programmatic management of drug-resistant tuberculosis*. 2008: World Health Organization.

135. Zhang, Y. and W. Yew, *Mechanisms of drug resistance in Mycobacterium tuberculosis [State of the art series. Drug-resistant tuberculosis. Edited by CY. Chiang. Number 1 in the series].* Int. J. Tuberc. Lung Dis., 2009. **13**(11): p. 1320-1330.

136. Tessema, B., et al., *Analysis of gene mutations associated with isoniazid, rifampicin and ethambutol resistance among Mycobacterium tuberculosisisolates from Ethiopia.* BMC Infect. Dis., 2012. **12**(1): p. 37.

137. Nebenzahl-Guimaraes, H., et al., *Systematic review of allelic exchange experiments aimed at identifying mutations that confer drug resistance in Mycobacterium tuberculosis.* J. Antimicrob. Chemother., 2014. **69**(2): p. 331-342.

138. Vareldzis, B.P., et al., *Drug-resistant tuberculosis: laboratory issues: World Health Organization recommendations.* Tuber and Lung Dis., 1994. **75**(1): p. 1-7.

139. Zhang, Y. and W.W. Yew, *Mechanisms of drug resistance in Mycobacterium tuberculosi.* Int. J. Tuberc. Lung Dis., 2009. **13**.

140. Zhao, M., et al., *Transmission of MDR and XDR tuberculosis in Shanghai, China.* PLoS One, 2009. **4**(2): p. e4370.

141. Escombe, A.R., et al., *Natural ventilation for the prevention of airborne contagion.* PLoS Med., 2007. **4**(2): p. e68.

142. Frieden, T.R., et al., *A multi-institutional outbreak of highly drug-resistant tuberculosis: epidemiology and clinical outcomes.* JAMA, 1996. **276**(15): p. 1229-1235.

143. Rather, I.A., et al., *Self-medication and antibiotic resistance: Crisis, current challenges, and prevention.* Saudi J. Biol. Sci., 2017. **24**(4): p. 808-812.

144. Kobaidze, K., A. Salakaia, and H.M. Blumberg, *Over the Counter Availability of Antituberculosis Drugs in Tbilisi, Georgia in the Setting of a High Prevalence of MDR-TB.* Interdiscip. Perspect. Infect. Dis., 2009. **2009**: p. 3.

145. Uplekar, M., et al., *Tuberculosis patients and practitioners in private clinics in India.* Int. J. Tuberc. Lung Dis., 1998. **2**(4): p. 324-329.

146. Cornwall, J., *Tuberculosis: a clinical problem of international importance.* The Lancet, 1997. **350**(9078): p. 660-661.

147. Castillo-Chavez, C. and Z. Feng, *To treat or not to treat: the case of tuberculosis.* J. Math. Biol., 1997. **35**(6): p. 629-656.

148. World Health Organisation. *Global strategy and targets for tuberculosis prevention, care and control after 2015a*. 2014; Available from: http://www.who.int/tb/strategy/End_TB_Strategy.pdf?ua=1.

149. O'Donnell, M.R., et al., *Re-inventing adherence: toward a patient-centered model of care for drug-resistant tuberculosis and HIV.* Int. J. Tuberc. Lung Dis., 2016. **20**(4): p. 430-434.

150. Fauci, A.S., *Multidrug-Resistant and Extensively Drug-Resistant Tuberculosis: The National Institute of Allergy and Infectious Diseases Research Agenda and Recommendations for Priority Research.* J. Infect. Dis., 2008. **197**(11): p. 1493-1498.

151. Forgarty International Center. *Fogarty funding spurs global health innovations*. 2013; Available from: https://www.fic.nih.gov/News/GlobalHealthMatters/november-december-2013/Pages/framework-innovations-projects.aspx.

152. Hendee, W.R., et al., *The National Institute of Biomedical Imaging and Bioengineering: history, status, and potential impact.* Radiology, 2002. **222**(1): p. 12-8.

153. *Plan to combat extensively drug-resistant tuberculosis: recommendations of the Federal Tuberculosis Task Force.* MMWR Recomm. Rep., 2009. **58**(Rr-3): p. 1-43.

154. World Health Organisation. *Surveillance of anti-tuberculosis drug resistance in the world: an updated analysis, 2007–2010.* 2012; Available from: http://www.who.int/bulletin/volumes/90/2/11-092585/en/.

155. Control, C.f.D. and Prevention, *Emergence of Mycobacterium tuberculosis with extensive resistance to second-line drugs--worldwide, 2000-2004.* MMWR. Morbidity and mortality weekly report, 2006. **55**(11): p. 301.

156. Gupta, R., et al., *Responding to market failures in tuberculosis control.* Science, 2001. **293**(5532): p. 1049-1051.

157. Volmink, J. and P. Garner, *Directly observed therapy for treating tuberculosis.* Cochrane Database Syst Rev, 2007. **4**.

158. Caminero, J.A., *Multidrug-resistant tuberculosis: epidemiology, risk factors and case finding [State of the art series. Drug-resistant tuberculosis. Edited by C-Y. Chiang. Number 4 in the series].* Int. J. Tuberc. Lung Dis., 2010. **14**(4): p. 382-390.

159. Aziz, M.A., et al., *Epidemiology of antituberculosis drug resistance (the Global Project on Anti-tuberculosis Drug Resistance Surveillance): an updated analysis.* Lancet, 2006. **368**(9553): p. 2142-54.

160. Lei, B., C.-J. Wei, and S.-C. Tu, *Action Mechanism of Antitubercular Isoniazid: Activation By Mycobacterium Tuberculosis KatG, Isolation, And Characterization Of Inha Inhibitor.* J. Biol. Chem., 2000. **275**(4): p. 2520-2526.

161. Wang, J.-Y., R.M. Burger, and K. Drlica, *Role of superoxide in catalase-peroxidase-mediated isoniazid action against mycobacteria.* Antimicrob. Agents Chemother., 1998. **42**(3): p. 709-711.

162. Shoeb, H.A., et al., *Peroxidase-mediated oxidation of isoniazid.* Antimicrob. Agents Chemother., 1985. **27**(3): p. 399-403.

163. Timmins, G.S., et al., *Nitric oxide generated from isoniazid activation by KatG: source of nitric oxide and activity against Mycobacterium tuberculosis.* Antimicrob. Agents Chemother., 2004. **48**(8): p. 3006-3009.

164. Johnsson, K., D.S. King, and P.G. Schultz, *Studies on the mechanism of action of isoniazid and ethionamide in the chemotherapy of tuberculosis.* J. Am. Chem. Soc., 1995. **117**(LIP-ARTICLE-1995-001): p. 5009-10.

165. Banerjee, A., et al., *inhA, a gene encoding a target for isoniazid and ethionamide in Mycobacterium tuberculosis.* Science, 1994. **263**(5144): p. 227-30.

166. Mdluli, K., et al., *Inhibition of a Mycobacterium tuberculosis β-Ketoacyl ACP Synthase by Isoniazid.* Science, 1998. **280**(5369): p. 1607-1610.

167. Marrakchi, H., G. Lanéelle, and A.k. Quémard, *InhA, a target of the antituberculous drug isoniazid, is involved in a mycobacterial fatty acid elongation system, FAS-II.* Microbiology, 2000. **146**(2): p. 289-296.

168. Winder, F. and P. Collins, *Inhibition by isoniazid of synthesis of mycolic acids in Mycobacterium tuberculosis.* Microbiology, 1970. **63**(1): p. 41-48.

169. Yuan, Y., et al., *Identification of a gene involved in the biosynthesis of cyclopropanated mycolic acids in Mycobacterium tuberculosis.* Proc. Natl. Acad. Sci. U. S. A., 1995. **92**(14): p. 6630-6634.

170. SAINT-JOANIS, B., et al., *Use of site-directed mutagenesis to probe the structure, function and isoniazid activation of the catalase/peroxidase, KatG, from Mycobacterium tuberculosis.* Biochem. J., 1999. **338**(3): p. 753-760.

171. Musser, J.M., *Antimicrobial agent resistance in mycobacteria: molecular genetic insights.* Clin. Microbiol. Rev., 1995. **8**(4): p. 496-514.

172. Heym, B., et al., *Implications of multidrug resistance for the future of short-course chemotherapy of tuberculosis: a molecular study.* Lancet, 1994. **344**(8918): p. 293-8.

173. Rouse, D.A., et al., *Characterization of the katG and inhA genes of isoniazid-resistant clinical isolates of Mycobacterium tuberculosis.* Antimicrob. Agents Chemother., 1995. **39**(11): p. 2472-2477.

174. Cockerill, I.I.I.F.R., et al., *Rapid Identification Of A Point Mutation Of The Mycobacterium tuberculosis Catalase-Peroxidase (katG) Gene Associated With Isoniazid Resistance.* J. Infect. Dis., 1995. **171**(1): p. 240-245.

175. DeVito, J.A. and S. Morris, *Exploring the Structure and Function of the Mycobacterial KatG Protein Using trans-Dominant Mutants.* Antimicrob. Agents Chemother., 2003. **47**(1): p. 188-195.

176. Rouse, D.A., et al., *Site - directed mutagenesis of the katG gene of Mycobacterium tuberculosis: effects on catalase –peroxidase activities and isoniazid resistance.* Mol. Microbiol., 1996. **22**(3): p. 583-592.

177. Zhang, Y., et al., *The catalase-peroxidase gene and isoniazid resistance of Mycobacterium tuberculosis.* Nature, 1992. **358**(6387): p. 591-3.

178. Timmins, G.S. and V. Deretic, *Mechanisms of action of isoniazid.* Mol. Microbiol., 2006. **62**(5): p. 1220-1227.

179. Sherman, D.R., et al., *Compensatory ahpC gene expression in isoniazid-resistant Mycobacterium tuberculosis.* Science, 1996. **272**(5268): p. 1641-3.

180. Hillas, P.J., et al., *The AhpC and AhpD antioxidant defense system of Mycobacterium tuberculosis.* J. Biol. Chem., 2000. **275**(25): p. 18801-9.

181. Hall, A., P.A. Karplus, and L.B. Poole, *Typical 2-Cys peroxiredoxins--structures, mechanisms and functions.* FEBS J., 2009. **276**(9): p. 2469-77.

182. Flohé, L. and J.R. Harris, *Peroxiredoxin Systems Structures and Functions.* 2007.

183. Perkins, A., et al., *Peroxiredoxins: guardians against oxidative stress and modulators of peroxide signaling.* Trends Biochem. Sci., 2015. **40**(8): p. 435-45.

184. Wood, Z.A., et al., *Structure, mechanism and regulation of peroxiredoxins.* Trends Biochem. Sci., 2003. **28**(1): p. 32-40.

185. Perkins, A., et al., *The sensitive balance between the fully folded and locally unfolded conformations of a model peroxiredoxin.* Biochemistry, 2013. **52**(48): p. 8708-21.

186. Wood, Z.A., et al., *Dimers to doughnuts: redox-sensitive oligomerization of 2-cysteine peroxiredoxins.* Biochemistry, 2002. **41**(17): p. 5493-504.

187. Nartey, W., et al., *NMR studies reveal a novel grab and release mechanism for efficient catalysis of the bacterial 2-Cys peroxiredoxin machinery.* FEBS J., 2015. **282**(23): p. 4620-4638.

188. Dip, P.V., et al., *Structure, mechanism and ensemble formation of the alkylhydroperoxide reductase subunits AhpC and AhpF from Escherichia coli.* Acta Crystallogr. D Biol. Crystallogr., 2014. **70**(Pt 11): p. 2848-62.

189. Chuang, M.H., et al., *The antioxidant protein alkylhydroperoxide reductase of Helicobacter pylori switches from a peroxide reductase to a molecular chaperone function.* Proc. Natl. Acad. Sci. U. S. A., 2006. **103**(8): p. 2552-7.

190. Moon, J.C., et al., *Oxidative stress-dependent structural and functional switching of a human 2-Cys peroxiredoxin isotype II that enhances HeLa cell resistance to H_2O_2-induced cell death.* J. Biol. Chem., 2005. **280**(31): p. 28775-84.

191. Jonsson, T.J., H.R. Ellis, and L.B. Poole, *Cysteine reactivity and thiol-disulfide interchange pathways in AhpF and AhpC of the bacterial alkyl hydroperoxide reductase system.* Biochemistry, 2007. **46**(19): p. 5709-21.

192. Lu, J. and A. Holmgren, *The thioredoxin antioxidant system.* Free Radic. Biol. Med., 2014. **66**: p. 75-87.

193. Guimaraes, B.G., et al., *Structure and mechanism of the alkyl hydroperoxidase AhpC, a key element of the Mycobacterium tuberculosis defense system against oxidative stress.* J. Biol. Chem., 2005. **280**(27): p. 25735-42.

194. Koshkin, A., et al., *The Mechanism of Mycobacterium tuberculosis Alkylhydroperoxidase AhpD as Defined by Mutagenesis, Crystallography, and Kinetics.* J. Biol. Chem., 2003. **278**(32): p. 29502-29508.

195. Wong, C.F., *Novel Insights into the N-terminus of Mycobacterium tuberculosis Alkylhydroperoxide Reductase subunit C.* 2016.

196. Wong, C.F., et al., *AhpC of the mycobacterial antioxidant defense system and its interaction with its reducing partner Thioredoxin-C.* Sci. Rep., 2017. **7**(1): p. 5159.

197. Zhang, Z., P.J. Hillas, and P.R. Ortiz de Montellano, *Reduction of peroxides and dinitrobenzenes by Mycobacterium tuberculosis thioredoxin and thioredoxin reductase.* Arch. Biochem. Biophys., 1999. **363**(1): p. 19-26.

198. Jaeger, T., et al., *Multiple thioredoxin-mediated routes to detoxify hydroperoxides in Mycobacterium tuberculosis.* Arch. Biochem. Biophys., 2004. **423**(1): p. 182-91.

199. Akif, M., et al., *Functional studies of multiple thioredoxins from Mycobacterium tuberculosis.* J. Bacteriol., 2008. **190**(21): p. 7087-95.

200. Cole, S.T., et al., *Deciphering the biology of Mycobacterium tuberculosis from the complete genome sequence.* Nature, 1998. **393**(6685): p. 537-44.

201. Lin, K., et al., *Mycobacterium tuberculosis Thioredoxin Reductase Is Essential for Thiol Redox Homeostasis but Plays a Minor Role in Antioxidant Defense.* PLoS Pathog., 2016. **12**(6): p. e1005675.

202. Grüber, G., et al., *Expression, purification, and characterization of subunit E, an essential subunit of the vacuolar ATPase.* Biochem. Biophys. Res. Commun., 2002. **298**(3): p. 383-91.

203. Waterhouse, A.M., et al., *Jalview Version 2—a multiple sequence alignment editor and analysis workbench.* Bioinformatics, 2009. **25**(9): p. 1189-1191.

204. *UniProt: the universal protein knowledgebase.* Nucleic Acids Res., 2017. **45**(D1): p. D158-D169.

205. Thompson, J.D., D.G. Higgins, and T.J. Gibson, *ClustalW: improving the sensitivity of progressive multiple sequence alignment through sequence weighting, position-specific gap penalties and weight matrix choice.* Nucleic Acids Res., 1994. **22**(22): p. 4673-80.

206. Higgins, D.G. and P.M. Sharp, *Clustal: a package for performing multiple sequence alignment on a microcomputer.* Gene, 1988. **73**(1): p. 237-44.

207. Seidman, C.E., et al., *Introduction of Plasmid DNA into Cells*, in *Curr. Protoc. Mol. Biol.* 2001, John Wiley & Sons, Inc.

208. Bornhorst, J.A. and J.J. Falke, *Purification of Proteins Using Polyhistidine Affinity Tags.* Methods Enzymol., 2000. **326**: p. 245-254.

209. Parsonage, D., et al., *Analysis of the link between enzymatic activity and oligomeric state in AhpC, a bacterial peroxiredoxin.* Biochemistry, 2005. **44**(31): p. 10583-92.

210. Peskin, A.V., et al., *Hyperoxidation of Peroxiredoxins 2 and 3: Rate constants for the reactions of the sulfenic acid of the peroxidatic cysteine.* J. Biol. Chem., 2013. **288**(20): p. 14170-14177.

211. Delaglio, F., et al., *NMRPipe: a multidimensional spectral processing system based on UNIX pipes.* J. Biomol. NMR, 1995. **6**(3): p. 277-93.

212. Goddard, T.D. and D.G. Kneller, *SPARKY.* May 30, 2008: University of California, San Francisco.

213. Olson, A.L., et al., *Solution structures of Mycobacterium tuberculosis thioredoxin C and models of intact thioredoxin system suggest new approaches to inhibitor and drug design.* Proteins, 2013. **81**(4): p. 675-89.

214. Schrodinger, LLC, *The PyMOL Molecular Graphics System, Version 1.8.* 2015.

215. Tang, G., et al., *EMAN2: an extensible image processing suite for electron microscopy.* J. Struct. Biol., 2007. **157**(1): p. 38-46.

216. Scheres, S.H., *RELION: implementation of a Bayesian approach to cryo-EM structure determination.* J. Struct. Biol., 2012. **180**(3): p. 519-30.

217. van Zundert, G.C., et al., *The HADDOCK2.2 Web Server: User-Friendly Integrative Modeling of Biomolecular Complexes.* J. Mol. Biol., 2016. **428**(4): p. 720-5.

218. Larkin, M.A., et al., *Clustal W and Clustal X version 2.0.* Bioinformatics, 2007. **23**(21): p. 2947-2948.

219. Papinutto, E., et al., *Crystal structure of alkyl hydroperoxide-reductase (AhpC) from Helicobacter pylori.* Biochim. Biophys. Acta, 2005. **1753**(2): p. 240-6.

220. Dip, P.V., et al., *Key roles of the Escherichia coli AhpC C-terminus in assembly and catalysis of alkylhydroperoxide reductase, an enzyme essential for the alleviation of oxidative stress.* Biochim. Biophys. Acta, 2014. **1837**(12): p. 1932-43.

221. Luft, J.R., J.R. Wolfley, and E.H. Snell, *What's in a drop? Correlating observations and outcomes to guide macromolecular crystallization experiments.* Cryst. Growth. Des., 2011. **11**(3): p. 651-663.

222. Sherman, D.R., et al., *AhpC, oxidative stress and drug resistance in Mycobacterium tuberculosis.* BioFactors, 1999. **10**(2-3): p. 211-7.

223. Hofmann, B., H.J. Hecht, and L. Flohe, *Peroxiredoxins.* Biol. Chem., 2002. **383**(3-4): p. 347-64.

224. Kamariah, N., et al., *Transition steps in peroxide reduction and a molecular switch for peroxide robustness of prokaryotic peroxiredoxins.* Sci. Rep., 2016. **6**: p. 37610.

225. Yang, K.S., et al., *Inactivation of human peroxiredoxin I during catalysis as the result of the oxidation of the catalytic site cysteine to cysteine-sulfinic acid.* J. Biol. Chem., 2002. **277**(41): p. 38029-36.

226. Dip, P.V., *Structural and functional insights into subunit a of Saccharomyces cerevisiae V-ATPase and the Escherichia coli Alkyl Hydroperoxide Reductase complex.* 2013.

227. Gao, G., J.G. Williams, and S.L. Campbell, *Protein-Protein Interaction Analysis by Nuclear Magnetic Resonance Spectroscopy*, in *Protein-Protein Interactions:*

Methods and Applications, H. Fu, Editor. 2004, Humana Press: Totowa, NJ. p. 79-91.

228. Rao, V.S., et al., *Protein-Protein Interaction Detection: Methods and Analysis.* Int. J. Proteomics, 2014. **2014**: p. 12.

Author's publication related to the projects

1. **Wong, C.F.**, et al., *AhpC of the mycobacterial antioxidant defense system and its interaction with its reducing partner Thioredoxin-C.* Scientific Reports, 2017. **7**(1): p. 5159.